COMPUTER MODELLING OF RESIDUAL STRESS & DISTORTION FOR ADDITIVELY MANUFACTURED METAL PARTS

A THESIS SUBMITTED TO
THE GRADUATE SCHOOL OF NATURAL AND APPLIED SCIENCES
OF
MIDDLE EAST TECHNICAL UNIVERSITY

BY

YUSUF ALPTUĞ POLAT

IN PARTIAL FULFILLMENT OF THE REQUIREMENTS
FOR
THE DEGREE OF MASTER OF SCIENCE
IN
METALLURGICAL AND MATERIALS ENGINEERING

NOVEMBER 2022

Approval of the thesis:

COMPUTER MODELLING OF RESIDUAL STRESS & DISTORTION FOR ADDITIVELY MANUFACTURED METAL PARTS

submitted by **YUSUF ALPTUĞ POLAT** in partial fulfillment of the requirements for the degree of **Master of Science in Metallurgical and Materials Engineering, Middle East Technical University** by,

Prof. Dr. Halil Kalıpçılar
Dean, Graduate School of **Natural and Applied Sciences**

Prof. Dr. Ali Kalkanlı
Head of the Department, **Met. and Mater. Eng., METU**

Assoc. Prof. Dr. Caner Şimşir
Supervisor, **Metallurgical and Materials Eng., METU**

Assist. Prof. Dr. Evren Yasa
Co-Supervisor, **Mech. Eng., Eskişehir Osmangazi Univ.**

Examining Committee Members:

Prof. Dr. Cemil Hakan Gür
Metallurgical and Materials Engineering, METU

Assoc. Prof. Dr. Caner Şimşir
Metallurgical and Materials Engineering, METU

Assist. Prof. Dr. Evren Yasa
Mech. Eng., Eskişehir Osmangazi University

Prof. Dr. Oğuzhan Yılmaz
Mechanical Engineering, Gazi University

Assist. Prof. Dr. Eda Aydoğan Güngör
Metallurgical and Materials Engineering, METU

Date: 28.11.2022

I hereby declare that all information in this document has been obtained and presented in accordance with academic rules and ethical conduct. I also declare that, as required by these rules and conduct, I have fully cited and referenced all material and results that are not original to this work.

Name, Last name : Yusuf Alptuğ Polat

Signature :

ABSTRACT

COMPUTER MODELLING OF RESIDUAL STRESS & DISTORTION FOR ADDITIVELY MANUFACTURED METAL PARTS

Polat, Yusuf Alptuğ
Master of Science, Metallurgical and Materials Engineering
Supervisor : Assoc. Prof. Dr. Caner Şimşir
Co-Supervisor: Assist. Prof. Dr. Evren Yasa

November 2022, 153 pages

Selective Laser Melting is a promising manufacturing technique which has been developed significantly in recent years. Additive nature of the process and selective fusion of metal powders enables manufacturing of complex geometries with minimum material wastege. However, residual stress formation during build stage of Selective Laser Melting process have negative effect on part mechanical properties and service life. Existence of residual stresses may lead to crack formation, part distortion and may reduce fatigue life eventually causing part failure. Although residual stress is released to some extent by post-process heat treatment, distortion occurs and allowable part tolerances may not be satisfied. For this reason, strong understanding of the mechanisms of residual stress and deformation is required in order to mitigate the detrimental effects of problems in question. Hovewer, the complex multiphysics characteristics of SLM process make it difficult to tailor the process parameters and overcome manufacturing issues; besides, long process time of the process and wastege of raw material make the experimental or trial-error solution approaches unfeasible. At this point numerical simulation techniques offer an applicable practice for the understanding, prediction and mitigation of residual stress and distoriton problem. In this study, modelling and simulation apporaches for residual stress and distortions for SLM process as well as subsequent heat treatment of 17-4 PH Stainless Steel are evaluated. Validation of simulation results are practiced with both CMM and contour residual stress measurement technique.

Keywords: Additive Manufacturing, Selective Laser Melting, Finite Element Method, Integrated Computational Materials Engineering, Modelling & Simulation, Residual Stress & Distortion

ÖZ

EKLEMELİ İMALAT İLE ÜRETİLMİŞ METAL PARÇALAR İÇİN BİLGİSAYAR DESTEKLİ KALINTI GERİLİM VE ÇARPILMA MODELLEMESİ

Polat, Yusuf Alptuğ
Yüksek Lisans, Metalurji ve Malzeme Mühendisliği
Tez Yöneticisi: Doç. Dr. Caner Şimşir
Ortak Tez Yöneticisi: Dr. Öğr. Üyesi Evren Yasa

Kasım 2022, 153 sayfa

Seçici Lazer Eritme, son yıllarda önemli ölçüde gelişme katetmiş umut vaadeden bir üretim tekniğidir. Prosesin eklemeli doğası ve metal tozlarının seçici olarak ergitilmesi, karmaşık geometrik yapıların minimum malzeme israfı ile üretilmesini sağlar. Ancak, Seçici Lazer Eritme işleminin yapım aşamasında oluşan artık gerilmelerin parça mekanik özellikleri ve çalışma ömrü üzerinde olumsuz etkileri vardır. Artık gerilimlerin varlığı, parça arızasına neden olabilecek çatlak oluşumuna, çarpılmalara neden olabilir ve yorulma dayancını düşürür. Artık gerilimler inşa sonrası ısıl işlemler ile belirli bir ölçüye kadar giderilse de çarpılmalar meydana gelebilir ve müsaade edilen parça toleransları karşılanmayabilir. Bu nedenle, söz konusu problemin zararlı etkilerini azaltmak için artık gerilme ve deformasyon mekanizmalarının güçlü bir şekilde anlaşılması gerekir. Ancak, SLM sürecinin karmaşık multifizik özellikleri, süreç parametrelerini uyarlamayı ve üretim sorunlarının üstesinden gelmeyi zorlaştırır; ayrıca uzun proses süresi ile beraber potansiyel hammadde israfı da deneysel veya deneme yanılma çözüm yaklaşımlarını olanaksız kılmaktadır. Bu noktada sayısal simülasyon teknikleri, artık gerilme ve çarpılma probleminin anlaşılması, tahmin edilmesi ve hafifletilmesi konusunda uygulanabilir bir çalışma yöntemi sunmaktadır. Bu tez çalışmasında 17-4 PH Paslanmaz Çeliğin SLM prosesi ve sonrasındaki ısıl işlemi için artık gerilme ve çarpılmalar için modelleme ve simülasyon yaklaşımları değerlendirilmektedir. Simülasyon sonuçlarının doğrulanması hem CMM hem de kontur artık gerilme ölçüm tekniği ile uygulanmaktadır.

Anahtar Kelimeler: Eklemeli İmalat, Seçici Lazer Ergitme, Sonlu Elemanlar Yöntemi, Bütünleşik Hesaplamalı Malzeme Mühendisliği, Modelleme & Simülasyon, Kalıntı Gerilim & Çarpılma

Every challenging work requires self-efforts as well as guidance of olders especially those who are very close to our soul.

I dedicate this humble effort to my beloved family:

Father, Mother & Sister

Whose affection, love, encouragement and supports make me able to get such success and honor.

ACKNOWLEDGMENTS

I would like to express my deepest gratitude to my supervisor Assoc.Prof. Dr. Caner Şimşir for his effort to transfer his wisdom with great patience and understanding.

I am also grateful to my assistant advisor, Assist. Prof. Dr. Evren Yasa, for her constructive criticism and sharing her valuable knowledge and experiences in an enlightening, guiding, and tolerant attitude.

I would like to thank to my supportive and collaborative colleagues Erkan Buğra Türeyen, Ece Kahraman, Oğuzcan Dedeci, Tansu Göynük, Can İhsan Tekinbaş, Okay Tutar, Gökhan Çelik, Mertcan Başkan and Orkun Umur Önem.

I also owe a great debt of gratitude to my experienced friend Aykut Demirkıran for his valuable supports and suggestions about measurement techniques.

I would also like to thank to my ICME research group, Gizem Özaltun and Utku Can Tuğutlu from METU Metallurgical and Materials Engineering, for their collaborative work and supports in softwares and challenging research processes.

I would also like to thank the technical staff of Atılım University Metal Forming Excellence Center for their supports in the tests.

I would like to thank my friends Ali Özalp, Andaç Özsoy, Berivan Tunca, Caner Yalçıner, Oğuzhan Bulut, Osman Dere, Yiğit Kemal Ökten, who have been always by my side, being supportive and encourageing.

Her beautiful eyes and warm smile make the difficulties more bearable. Başak Tanriverdi, I am so lucky to have you in my life.

Finally, my dear family for all their financial and moral support that they have never spared throughout my life; I express my deep gratitude to my mother, father and sister.

TABLE OF CONTENTS

ABSTRACT v

ÖZ vii

ACKNOWLEDGMENTS x

TABLE OF CONTENTS xi

LIST OF TABLES xiv

LIST OF FIGURES xv

LIST OF ABBREVIATIONS xxi

LIST OF SYMBOLS xxii

CHAPTERS

1 INTRODUCTION 1

2 LITERATURE REVIEW 5

2.1 Additive Manufacturing 5

2.1.1 An Introduction to Metal Additive Manufacturing 5

2.1.2 Major Types of Metal Additive Manufacturing 6

2.2 Challenges in Additive Manufacturing 9

2.3 17-4 PH Stainless Steel 10

2.3.1 Introduction to 17-4 PH Stainless Steel 10

2.3.2 17-4 PH SS in Metal Additive Manufacturing 12

2.4 Introduction to Residual Stresses 14

2.4.1 Classification of Residual Stress 14

2.4.2 Residual Stresses in Metal Additive Manufacturing 16
2.4.3 Factors Affecting Residual Stress 19
2.5 Experimental Approaches for Measurement of Residual Stress 26
2.5.1 Contour Method 27
2.6 Numerical Approaches for Predicting Residual Stress 30
2.6.1 Finite Element Method 30
2.6.2 Thermal Modelling Approach 31
2.6.3 Thermo-Mechanical Modelling Approach 33
2.6.4 Mechanical Modelling (Inherent Strain) Approach 34
2.6.5 Element Birth and Death 38
2.7 Calphad Approach 38
2.8 FEA Software Tools 39
2.9 Dilatometry Test 40
3 EXPERIMENTAL PROCEDURE 41
3.1 Starting Materials 41
3.1.1 Selective Laser Melting Equipment 44
3.2 Optimised SLM Process Parameters for 17-4 PH 44
3.3 Material Data 45
3.4 Mesoscale Model in Simufact Welding 48
3.5 Preliminary Settings and Calibration for Simufact Additive 50
3.5.1 Mechanical Calibration 50
3.5.2 Thermal Calibration 52
3.5.3 Thermomechanical Calibration 52
3.5.4 Simufact Additive 53

3.6 Dilatometric Study 57
3.7 Manufacturing for Validation of Distortion 57
3.8 Manufacturing for Validation of Residual Stress 60
3.9 Contour Residual Stress Measurement 63
3.9.1 Measurement of Surface Deformations with CMM 63
3.9.2 pyCM Software 64
4 RESULTS AND DISCUSSION 71
4.1 Validation of Simulation 71
4.2 Mesoscale Model 73
4.3 Mechanical Analysis vs Thermomechanical Analysis 91
4.4 Thermal Examination 92
4.5 Distortion 95
4.6 Residual Stress 95
4.6.1 Simulation and Contour Residual Stress Measurement Results 95
4.6.2 Comparison of Simulation Results with Contour Method 105
4.6.3 Evaluation of Crosses Regarding Contour Method 114
4.7 Critical Temperatures 119
5 CONCLUSION 123
REFERENCES 127

APPENDICES

A. DILATOMETRY 139
B. MATERIAL DATA 142
C. PHASE TRANSFORMATION STRAIN 153

LIST OF TABLES

TABLES

Table 1: 17-4 PH Stainless Steel Chemical Composition 11
Table 2: Heat Treatment Conditions for 17-4 PH Stainless Steel [24] 12
Table 3: Optimized Process Parameters for 17-4 PH Stainless Steel...................... 45
Table 4: Measured Z-max distortions after cutting of cantilever beams 51
Table 5: Calibrated Inherent Strain values 52
Table 6: Volumetric Expansion Factor (VEF) calibration results 53
Table 7: Critical Temperatures of Wrought & SLM'ed 17-4 PH Stainless Steel .. 120
Table 8: Hybrid Material Data 142
Table 9: Phase transformation strain values of SLM'ed 17-4 PH SS in X-Y-Z directions 153

LIST OF FIGURES

FIGURES

Figure 1: Classification of Additive Manufacturing Technology [9] 7

Figure 2: Schematic view of Selective Laser Melting [15] 9

Figure 3: (a) optical micrograph of conventionally processed 17-4 PH SS (b) EBSD image of conventionally processesed 17-4 PH SS (c) optical micrograph of SLM'ed as built 17-4 PH SS (d) EBSD image of SLM'ed as built 17-4 PH SS where grains oriantate along build direction [26] 13

Figure 4: Types of residual stresses [30] 15

Figure 5: Residual Stress formation in Additive Manufacturing a) During heating b) During cooling [30] 16

Figure 6: Negative effects of residual stress in metal AM a) reduced fatigue performance due to tensile residual stress b) deformation after cutting from baseplate c) residual stress causing distortion and resulting in recoater contact [30] 17

Figure 7: Failures due to residual stress a) delaminations b) seperation from supports c) cracks [33] [34] 18

Figure 8: Microcracks caused by residual stress formation during SLM processing [35], [36] 18

Figure 9: Process failure due to damaged recoater blade....................................... 19

Figure 10: Three bar analogy of residual stress formation 20

Figure 11: Axial stress evolution during cooling in welded steel undergoing phase transformations [40] 21

Figure 12: Mechanisms of Displasive and Reconstructive phase transformations. 22

Figure 13: Steel phases and regarding transformation types [41].......................... 22

Figure 14: Common residual stress measurement techniques 27

Figure 15: Schematic of EDM Cutting [56] 29

Figure 16: Schematic representation of inherent strain: a) standard state, b) stressed state, c) stress-free state [67].. 34

Figure 17: Inherent Strain Approach [68] 35
Figure 18: Element Activation Procedure[77] 38
Figure 19: Dilatation during phase transformation 40
Figure 20: Particle Size Distribution 42
Figure 21: SEM image of gas atomized 17-4 PH SS powder 42
Figure 22: EDS analysis of 17-4 PH SS powder 43
Figure 23: Mesoscale model in Simufact Welding 49
Figure 24: Simulation for inherent strain calibration 51
Figure 25: Mesh Convergence Analysis 54
Figure 26: Maximum Calculated Von Mises Stress vs Voxel Mesh Size 55
Figure 27: Solve Time for Simulation vs Voxel Mesh Size 55
Figure 28: Representation of Simufact Additive heat transfer calculations 56
Figure 29: Manufactured impellers for distortion measurement 58
Figure 30: CMM dimensional measurement of impellers 59
Figure 31: SLM'ed cross parts for the experimental validation of residual stress ... 60
Figure 32: Crosses Group 1 scan pattern 61
Figure 33: Crosses Group 2 scan pattern 62
Figure 34: Crosses after cut from baseplate 63
Figure 35: Measurement of Surface Deformations 64
Figure 36: Registration of Reference surface- Top view 65
Figure 37: Registration of Reference Surface- Side view (250x scale) 66
Figure 38: Preview of registered Reference and Floating surfaces 66
Figure 39: Averaging and gridding of Reference and Floating surfaces 67
Figure 40: Numerical Fitting of averaged surface 68
Figure 41: Extruding & meshing of the geometry and specification of numerically fitted surface deformations as well as boundary conditions to prevent rigid body motion and rotation 69
Figure 42: Optical microscopy of as built 17-4 PH SS in the build direction 71
Figure 43: EDS line analysis 72
Figure 44: EDS line analysis results 73

Figure 45: Mesoscale model thermal results 74
Figure 46: Melt pool in mesoscale model results 75
Figure 47: Mesoscale model melt pool depth 76
Figure 48: Mesoscale model thermal history of bottom node 77
Figure 49: Examination along X direction 78
Figure 50: Temperature profile along X direction 79
Figure 51: X Temperature gradient along X direction 79
Figure 52: Y Temperature gradient along X direction 80
Figure 53: Z Temperature gradient along X direction 80
Figure 54: Temperature gradient along X direction 81
Figure 55: X Normal Stress along X direction 81
Figure 56: Y Normal stress along X direction 82
Figure 57: Z Normal Stress along X direction 82
Figure 58: Equivalent Stress along X direction 83
Figure 59: Examination along Y direction 84
Figure 60: Temperature profile along Y direction 85
Figure 61: X Temperature gradient along Y direction 86
Figure 62: Y Temperature gradient along Y direction 86
Figure 63: Z Temperature gradient along Y direction 87
Figure 64: Temperature gradient along Y direction 88
Figure 65: X Normal Stress along Y direction 88
Figure 66: Y Normal Stress along Y direction 89
Figure 67: Z Normal Stress along Y direction 89
Figure 68: Equivalent Stress along Y direction 90
Figure 69: Comparison of analysis times of Mechanical and Thermomechanical analysis 91
Figure 70: Ratio of analysis times of Mechanical and Thermomechanical analysis 92
Figure 71: Temperature of top node of cube with edge length of 20 mm 93
Figure 72: Thermal history of selected node 94

Figure 73: Laser Scanned Surface Data 95
Figure 74: Contour Method: Distribution of σyy component of residual stress at the Y-cut surface of parallelly scanned Cross 1 96
Figure 75: Contour Method: Distribution of σxx component of residual stress at the X-cut surface of parallelly scanned Cross 2 97
Figure 76: Contour Method: Distribution of σzz component of residual stress at the Z-cut surface of parallelly scanned Cross 3 98
Figure 77: Contour Method: Distribution of σyy component of residual stress at the Y-cut surface of rotationally scanned Cross 4 99
Figure 78: Contour Method: Distribution of σxx component of residual stress at the X-cut surface of rotationally scanned Cross 5 100
Figure 79: Contour Method: Distribution of σyy component of residual stress at the Z-cut surface of rotationally scanned Cross 6 101
Figure 80: Thermomechanical Analysis: Distribution of σyy component of residual stress at the Y-cut surface of rotationally scanned Cross 4 102
Figure 81: Thermomechanical Analysis: Distribution of σxx component of residual stress at the X-cut surface of rotationally scanned Cross 5 102
Figure 82: Thermomechanical Analysis: Distribution of σzz component of residual stress at the Z-cut surface of rotationally scanned Cross 6 103
Figure 83: Mechanical Analysis: Distribution of σyy component of residual stress at the Y-cut surface of parallelly scanned Cross 4 103
Figure 84: Mechanical Analysis: Distribution of σxx component of residual stress at the X-cut surface of parallelly scanned Cross 5 104
Figure 85: Mechanical Analysis: Distribution of σxx component of residual stress at the X-cut surface of parallelly scanned Cross 6 104
Figure 86: Stress distribution on X-Cut of cross part along A-B line (Cross 5) ... 106
Figure 87: σxx on X-Cut surface of cross part along A-B line 107
Figure 88: Stress distribution on Y-Cut of cross part along C-D line 108
Figure 89: σyy on Y-Cut of cross part along C-D line (Cross 4) 109
Figure 90: Stress distribution on Z-Cut of Cross 6 along X-Direction (E-F line). 110

Figure 91: Z Normal Stress on Z-Cut of Cross 6 along X-Direction (E-F line) ... 111
Figure 92: Stress distribution on Z-Cut of Cross 6 along Y-Direction (G-H line) 112
Figure 93: Z Normal Stress on Z-Cut of Cross 6 along Y-Direction (G-H line) .. 113
Figure 94: Comparison of Contour results: a) Cross 3 (parallel scan) b) Cross 6 (rotational scan) ... 114
Figure 95: Residual Stress profile of Crosses 1 and 4 along their height ... 115
Figure 96: Residual Stress profile of Crosses 2 and 5 along their height ... 116
Figure 97: Residual Stress profile of Crosses 1 and 2 along their height ... 117
Figure 98: Residual Stress profile of Crosses 4 and 5 along their height ... 118
Figure 99: Dilatometry test result ... 119
Figure 100: Critical Temperatures (AC1-AC3) ... 121
Figure 101: Critical Temperatures (MS-MF) ... 121
Figure 102: Wrought 17-4 PH X-Cut ... 139
Figure 103: Wrought 17-4 PH Y-Cut ... 139
Figure 104: Wrought 17-4 PH Z-Cut ... 140
Figure 105: SLM'ed 17-4 PH X-Cut ... 140
Figure 106: SLM'ed 17-4 PH Y-Cut ... 141
Figure 107: SLM'ed 17-4 PH Z-Cut ... 141
Figure 108: Temperature dependent thermal conductivity data of 17-4 PH SS ... 146
Figure 109: Temperature dependent density data of 17-4 PH SS ... 146
Figure 110: Temperature dependent thermal expansion coefficient data of 17-4 PH SS ... 147
Figure 111: Temperature dependent specific heat capacity data of 17-4 PH SS .. 147
Figure 112: Temperature dependent Elastic Modulus data of 17-4 PH SS ... 148
Figure 113: Temperature dependent Poisson’s ratio data of 17-4 PH SSCreep Data ... 148
Figure 114: Stages of Creep ... 149
Figure 115: Creep data obtained from JmatPro at 2 different temperatures ... 150
Figure 116: Dilatometry curve between martensite start to martensite finish temperatures ... 151

Figure 117: Lever Rule between MS-MF 151
Figure 118: Fraction of martensite transformed between MS-MF........................152
Figure 119: Calculation of phase transformation strain 153

LIST OF ABBREVIATIONS

ABBREVIATIONS	
AM	Additive Manufacturing
CTE	Coefficient of Thermal Expansion
EDM	Electrical Discharge Machining
IS	Inherent Strain
SEM	Scanning Electron Microscopy
SLM	Selective Laser Melting
SHT	Solutionizing Heat Treatment
STL	Steolitography
TM	Thermomechanical
P	Laser Power
PH	Precipitation Hardening
XRD	X-Ray Diffraction

LIST OF SYMBOLS

SYMBOLS	
α	Coefficient of Thermal Expansion
σ	Stress
cp	Specific Heat Capacity
ε	Strain
k	Thermal Conductivity
ρ	Density
v	Poisson’s Ratio

CHAPTER 1

INTRODUCTION

Development of metal-based additive manufacturing began in the 1980s and made important progresses until today. State of the art technology offers advantages such as almost unlimited design freedom, rapid design verification, high adaptability, and minimization of waste materials. As metal AM has draw attention of various fields, especially biomedical and aviation, it could able to prove itself in these fields [1], [2]. Contrary to conventional machining processes which are based on material subtraction from bulk material, metal AM processes are basically repetitive fusion and addition of materials together. For this reason, AM enables manufacturing of complex geometries and controlled porous structures that are not possible with conventional methods. In addition to this, effect of geometric complexity on manufacturing costs are very limited unlike conventional methods [3].

In recent years, the metal-based additive manufacturing market has expanded greatly all over the world. By enabling parts to be produced directly from a CAD file, it is considered one of the key technologies on the path to digitization and industry 4.0, setting high expectations in the market. However, metal additive manufacturing market size is still a niche compared to other manufacturing technologies. Although the average growth rate of the additive manufacturing sector, which was 27.4% at the end of 2020 compared to previous years, slowed down due to the pandemic, the sector still expanded by 7.5% and reached 12.8 billion USD.

As a subbranch of metal AM, Selective laser melting (SLM) is a promising technique considering its advantages, however a few key issues limited its development. One of the main problem encountered during the manufacturing stage is residual stress formation. During SLM processing of metals, high thermal gradients and high cooling rates on the order of $10^3 - 10^8$ together with the complex heating-cooling cycles results in residual stress and deformation [4].

Residual stresses and distortions that are developed in the "part building" and partially relieved in subsequent "heat treatment" processes are important sub-processes of the Selective Laser Melting Process. As the understanding and design of these processes are critical in terms of part tolerancing and dimensional quality, these are also criticial for the mitigation of in service failures like fatigue or in process failures like cracking which decrease production efficiency[5].

Experimental effort on mitigation or determination of residual stress and distortion for SLM process inevitably lead to loss of time and money. At this point Integrated Computational Materials Engineering (ICME) outweighs the trial-error approach. As Gregory B. Olson mentioned in his studies ICME is a multidisciplinary approach that connects material models at multiple length scales to design products, related materials and material production methods. In phrase of ICME, the word "Integrated" has been emphasized in multiple relations, and the word "Engineering" has been emphasized to take care of industrial benefit. The focus in the approach is to analyze material models based on thermal, mechanical, electrical, magnetic etc. laws. Under material-process-property relations, ICME eases to solve engineering problems which requires deep knowledge in physics, materials engineering and mechanical engineering.

In this thesis study, modelling and simulation approaches for SLM processing of 17-4 PH SS regarding the current approaches such as thermal, mechanical and thermomechanical approaches will be evaluated by using the finite element basis as multi scale (mesoscale and macroscale) models. Required input material data is generated by using JMatPro software database. The complete study will be carried out in two branches as experimentally and numerically.

In experimental studies, the focus is on 2 subjects;

- Firstly material characterization techniques are carried out experimentally in order to measure critical components of 17-4 PH SS material data, such as coefficient of thermal expansion, MS-MF & AC1-AC3 temperatures and Koistinen-Marburger Parameter are determined for the use of input material data.
- Secondly, for the validation of simulation results, part build and heat treatments are carried out. Residual stress distributions are calculated indirectly by contour method and part deformations are measured by CMM.

For the numerical studies on the other hand, the focus is on 2 subjects;

- Firstly detailed thermal and thermomechanical simulations are run for SLM at mesoscale. Model dimensions are not greater than 1mm.
- Secondly, thermal, mechanical and thermomechanical approaches are evaluated at macro (part) scale for complete process chaing including "building" and "heat treatment" stages. Model dimensions vary between 20mm and 100mm. Phase transformations effect is taken into account which is important in the formation of residual stresses. The stress fields obtained by simulation from the part building stage will be used as the initial stress distribution data for the post-heat treatment simulation. Relaxation model that takes "creep" laws into account is used for heat treatment simulation.

Finally, for the validation section, simulation results and experimental measurement results for residual stress and distortions are compared and models are validated.

In summary, the residual stresses and undesirable shape and dimension changes (distortions) that occur in the material during manufacturing are the main problems affecting the product quality and manufacturability which result in serious time and money loss for metal additive manufacturing processes. The aim of this study is to create a deep knowledge and understanding of residual stress formation-relaxation mechanisms within the scope of complete process chain including part build and heat treatment steps of the SLM process and finally gaining prediction capability by developing various current models as a holistic.

CHAPTER 2

LITERATURE REVIEW

2.1 Additive Manufacturing

Additive manufacturing (AM), also known as 3-D printing, is a general term which is performed by addition of material. AM is defined by ASTM organisation as;

“A process of joining materials to make objects from 3D model data, usually layer upon layer, as opposed to subtractive manufacturing methodologies”

AM is first developed for the processing of polymeric materials by Charles Hull and the technique he invented is known as Steolitography (SLA) which led to development of the advanced AM technology [6]. As the technology has been matured over time, different sub-branches of AM technology have been emerged which enabled processing of different types of materials including metals, polymers, ceramics and composites. Today, AM parts successfully operate at several applications; from flying aircafts, rockets launching for space missions to human cranial implants.

2.1.1 An Introduction to Metal Additive Manufacturing

The development of the metal based additive manufacturing technology started at earlier 1980’s and today became a trending manufacturing technique due to advantages offered such as design flexibility, rapid prototyping, ease of production of complex parts, customer-specific production and waste minimization and due to these reasons having an important potential for the future of manufacturing technology. In the last years, development of metal additive manufacturing processes has gained acceleration thanks to its advantages like design flexibility, rapid prototyping and ease of producing complex parts [7].

2.1.2 Major Types of Metal Additive Manufacturing

In the most general sense, all sub-branches of AM processes are grounded on the same working principle; adding material. The differences between them are either the form of raw material, solidification mechanism or the way of supplying raw material. There are 7 different type of additive manufacturing processes defined by ASTM which is given below Figure 1 [8].

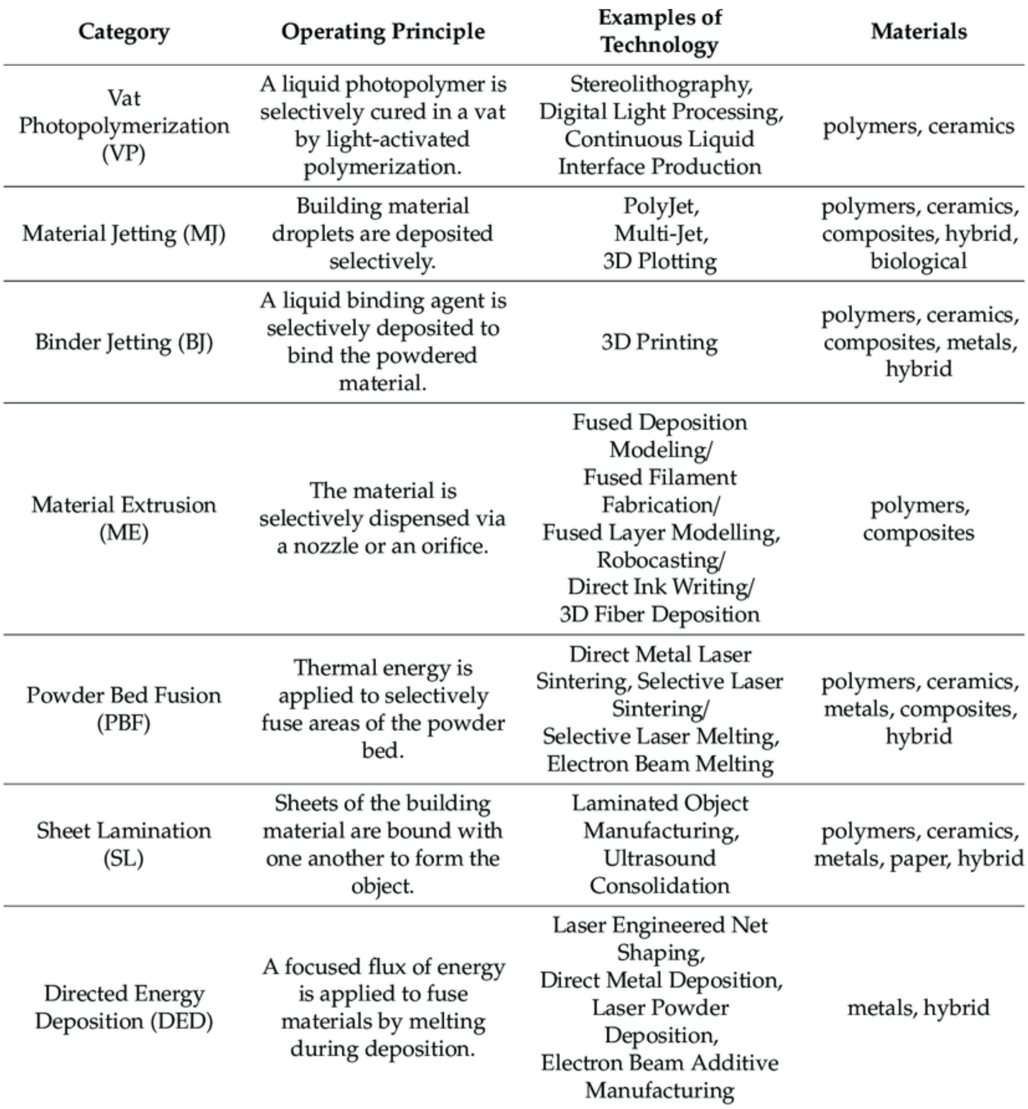

Category	Operating Principle	Examples of Technology	Materials
Vat Photopolymerization (VP)	A liquid photopolymer is selectively cured in a vat by light-activated polymerization.	Stereolithography, Digital Light Processing, Continuous Liquid Interface Production	polymers, ceramics
Material Jetting (MJ)	Building material droplets are deposited selectively.	PolyJet, Multi-Jet, 3D Plotting	polymers, ceramics, composites, hybrid, biological
Binder Jetting (BJ)	A liquid binding agent is selectively deposited to bind the powdered material.	3D Printing	polymers, ceramics, composites, metals, hybrid
Material Extrusion (ME)	The material is selectively dispensed via a nozzle or an orifice.	Fused Deposition Modeling/ Fused Filament Fabrication/ Fused Layer Modelling, Robocasting/ Direct Ink Writing/ 3D Fiber Deposition	polymers, composites
Powder Bed Fusion (PBF)	Thermal energy is applied to selectively fuse areas of the powder bed.	Direct Metal Laser Sintering, Selective Laser Sintering/ Selective Laser Melting, Electron Beam Melting	polymers, ceramics, metals, composites, hybrid
Sheet Lamination (SL)	Sheets of the building material are bound with one another to form the object.	Laminated Object Manufacturing, Ultrasound Consolidation	polymers, ceramics, metals, paper, hybrid
Directed Energy Deposition (DED)	A focused flux of energy is applied to fuse materials by melting during deposition.	Laser Engineered Net Shaping, Direct Metal Deposition, Laser Powder Deposition, Electron Beam Additive Manufacturing	metals, hybrid

Figure 1: Classification of Additive Manufacturing Technology [9]

2.1.2.1 Powder-Bed Fusion (PBF)

One common class among the metal based additive manufacturing techniques is Powder Bed Fusion processes. The process is carried out by spreading thin layer of closely packed metallic powder over a platform and then melting the selected area according to a CAD (Computer Aided Design) data. As top layer is printed by heat source, the platform is lowered and new layer of metal powder is spread with a recoater blade. The process repeats itself and desired geometry is manufactured in a layer-by-layer fashion until the product has completely formed. The entire building process is autometed [10].

The procedure of PBF is carried out by using either laser or electron beam as an energy source. Energy source selectively melts and fuses the metal powder bed together in an inert atmosphere or under vacuum. Selective Laser Melting (SLM) and Electron Beam Melting (EBM) are 2 processes which fall into this class. As their names signifiy, SLM uses laser and EBM uses electron beam as heat source [11].

PBF processes are widely used in different industries including aerospace, automotive or medicine due to their ability to manufacture nearly fully dense engineering metallic materials including Aluminum, Steel, Nickel-based superalloys or copper for structural and functional use [12].

2.1.2.1.1 Selective Laser Melting

SLM is a widely used PBF processes where high power-density laser beam is used as a heat source. By SLM process near net-shape, fully functional products can be manufactured. The building process is often carried out under protective atmosphere (either Nitrogen or Argon gas) in order to prevent oxidation [13]. The thickness of the powder varies between 20-50µm which affects the resolution, product tolerance and powder flowability and build rate [14].

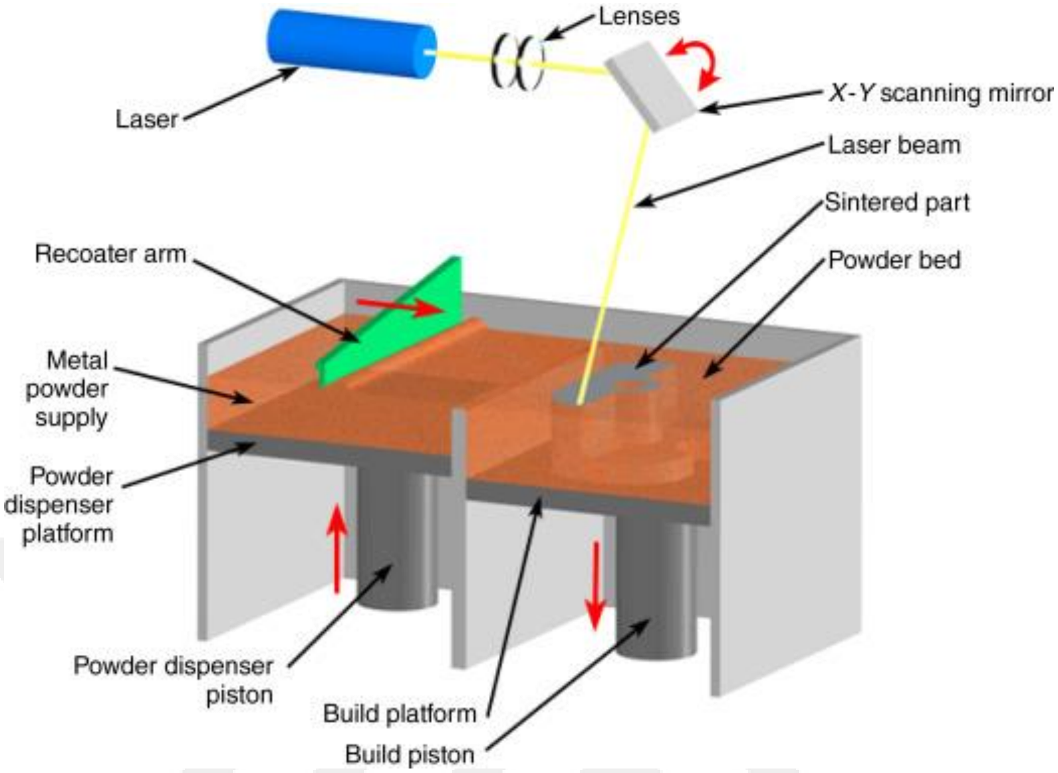

Figure 2: Schematic view of Selective Laser Melting [15]

Having finished the building process, the part is removed from the loose powders and then it is separated from the platform manually or by Electric Discharge Machining (EDM).

2.2 Challenges in Additive Manufacturing

Eventhough AM offers many advantages, it has still challanges which requires work to overcome. One challange is the slow production rate; depending on the part size, process takes days which eventually slowing down the transition to mass production and pushing up the cost of AM. Secondly, the spectrum of materials which can be additively manufactured is still limited comparing to conventional manufacturing which limits the application of AM thereby materials, process parameters or equipments still require development. Another concern is the part quality and repeatability of AM processes due to uncertainities in material performance which eventually may require different quality control or testing routes than conventional manufacturing. In literature, many studies reported quite different material properties[16] [5] [17]. Variety of standards are still being developed in order to assure proper quality control and set optimisation routes to overcome this issue [7]. Another issue is the high cooling rates of AM processes. Cooling rates of SLM on the order of 10^6 K/sec leads to formation of metastable phases and unique microstructures as well as residual stresses which is the main focus of this study which is going to be discussed in detail at next chapters.

2.3 17-4 PH Stainless Steel

2.3.1 Introduction to 17-4 PH Stainless Steel

17-4 PH Stainless Steel, named for its chemical content, contains approximately %17 chromium and %4 Nickel as main alloying elements. 17-4 PH Stainless Steel is a sub-class of precipitation hardened stainless steel, offering good balace between corrosion resistance and mechanical properties at high temperature. [18]. Compared to austenitic stainless steels, such as 304 and 316, precipitation hardened martensitic stainless steels have 3-4 times higher strength. When produced with conventional methods like welding, casting or forging, 17-4 PH stainless steel is fully martensitic. Due to its comperatively good strength and corrosion resistance, 17-4 PH stainless steel has broad applications areas in fields like aerospace, medical and food [19]. Standard composition of 17-4 PH SS is given below table;

Table 1: 17-4 PH Stainless Steel Chemical Composition

Composition	Wt %
Iron (Fe)	Balance
Carbon (C)	0.07 max
Chromium (Cr)	15.00-17.50
Nickel (Ni)	3.00-5.00
Copper	3.00-5.00
Silicon (Si)	1.00 max
Manganese (Mn)	1.00 max
Phosphorus (P)	0.04 max
Niobium + Tantalum (Nb+Ta)	0.15-0.45
Sulfur (S)	0.03 max

Copper and Niobium are the essential elements for the precipitation hardening and the hardening is dominated by Copper element in the martensitic phase after solutionizing and subsequent heat treatment for aging [20], [21]. Since different heat treatment procedures at different temperatures end up with different microstructures, wide range of mechanical properties can be achieved [22].

After solutionizing at 1038 °C and quenching, the aging heat treatment is carried out in the range of 480-620 °C [23]. 17-4 PH stainless steel can be heat treated into 8 different conditions as standard depending on the application or design requirement of the material which are given below;

Table 2: Heat Treatment Conditions for 17-4 PH Stainless Steel [24]

Condition	*Hardening Temperature* (°C)	*Hardening Time (hours)*	*Type of Cooling*
H 900	482	1	Air
H 925	496	4	Air
H 1025	552	4	Air
H 1075	579	4	Air
H 1100	593	4	Air
H 1150	621	4	Air
H 1150-D	621 - 621	4 - Followed by 4	Air
H 1150-M	760 - 621	2 - Followed by 4	Air

2.3.2 17-4 PH SS in Metal Additive Manufacturing

17-4 PH SS provides excellent weldability. The alloy is also applicable for metal AM which can be considered as countless of micro welding process. Contrary to the good mechanical properties offered by 17-4 PH SS, it has a low workability especially for the production of complex shapes because of high hardness induced by precipitation hardening mechanism. At this point metal additive manufacturing becomes promising for the production of 17-4 PH stainless steel into the complex shapes in high geometrical accuracy by reducing or completely eliminating the machining operations [25]

Microstructure of additively manufactured 17-4 PH stainless steel differ by microstructure and phases from conventionally manufactured counterparts. For 17-4 PH parts manufactured by conventional processes such as casting, forging etc. phase transformation sequence follows δ-ferrite > γ-austenite > martensite transformations. On the contrary, metal additive manufacturing processes results in very high cooling rates on the order of $10^5 - 10^6$ K/sec which cancels out the equilibrium phase diagram therefore non-equilibrium phases are present for additively manufactured 17-4 PH SS [26]. Moreover, grains of additively manufactured 17-4 PH stainless steel have texture and epitaxial growth orientate along the build direction unlike conventionally processed alloy as shown in below Figure 3;

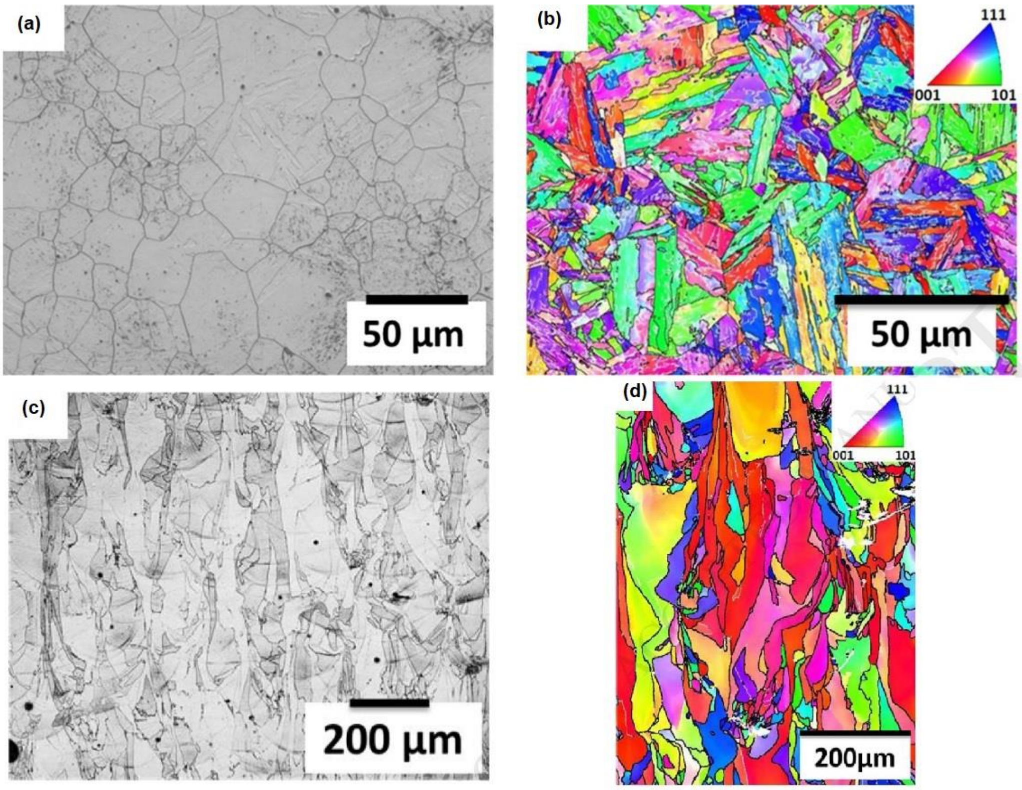

Figure 3: (a) optical micrograph of conventionally processed 17-4 PH SS (b) EBSD image of conventionally processesed 17-4 PH SS (c) optical micrograph of SLM'ed as built 17-4 PH SS (d) EBSD image of SLM'ed as built 17-4 PH SS where grains oriantate along build direction [26]

Studies show that depending on the Cr/Ni equivalent, microstructure of the SLM'ed 17-4 PH can be either fully martensitic or ferritic. It was also shown that martensitic phase is more prone to transform into reverted austenite during the precipitation heat treatment. Eventhough conventionally processed 17-4 PH SS has a martensitic microstructure, conflicting studies have been reported about the microstructure of additively manufactured 17-4 PH SS. The resulting microstructure mainly depends on the protective atmosphere being used during build and Cr_{eq}/Ni_{eq} ratio of initial powder. In their study, Rafi et al reported fully martensitic with a small amount of retained austenite microstructure which is processed under argon atmosphere. On the other hand, when the process is under nitrogen atmosphere, martensite and austenite phases are nearly in half shares [27]. In their 2 different study, Alnajjar et al. stated that the microstructure of SLM'ed 17-4 PH is fully delta ferritic. This is because of the very high cooling rates, on the order of 10^6 K/sec, prevents delta ferrite to transform into austenite and therefore first solidified delta ferrite is retained at room temperature. Since 17-4 PH SS has a very low carbon content, crystal structure of martensite is BCT and thus martensite-ferrite identification cannot be made from XRD. In order to identify the present phase, EBSD analysis was done and parent austenite phase is not found so it can be deduced that the present phase is delta ferrite [26], [28].

2.4 Introduction to Residual Stresses

Residual stresses are defined as the stresses which preseent in a material at equilibrium even there is no net external force applied on that material Origin of the residual stresses in metallic materials may be resulted from nearly all stages of manufacturing such as casting, welding, additive manufacturing, heat treating or machining [29].

2.4.1 Classification of Residual Stress

Residual stresses are classified as TypeI, TypeII and TypeIII residual stresses according to the length scale where they exist.

TypeI residual stresses exist at macroscopic scale and may cause long range distortions.

TypeII residual stresses also called as intergranular stresses which exist on grain scale and considered as microlevel residual stress. These stresses are caused by the local microstructural differences like coherency/incoherency of precipitates or differences in slip behavior of grains.

TypeIII residual stresses exist at atomic scale and caused by the existence of substitutional atoms or vacancies.

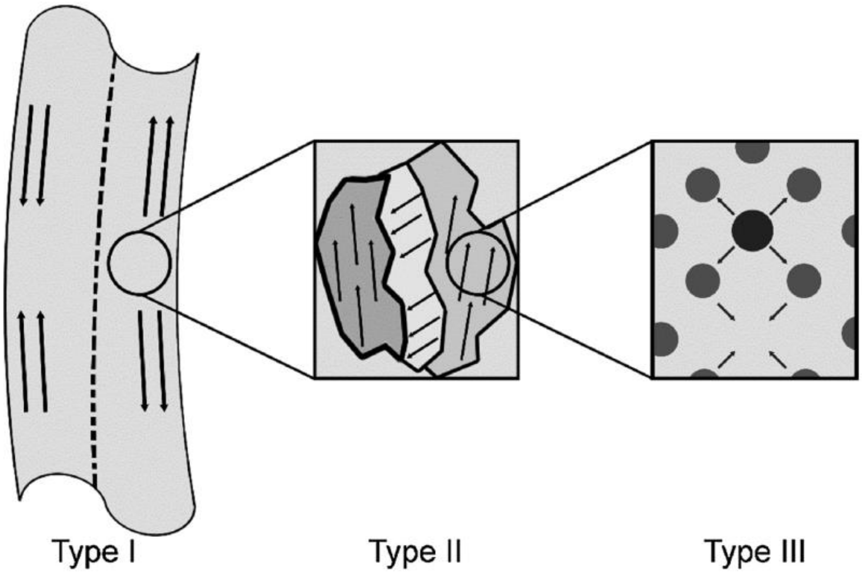

Figure 4: Types of residual stresses [30]

TypeI residual stress, which directly effect the mechanical properties of material, is effective over part scale large distances and dominant among the TypeII and TypeIII residual stresses since these are caused by short scale atomic mismatch or dislocations. On the other hand, considering the resolution of available test methods, measurement of TypeII and TypeIII .are not applicable since high level of resolution is required. Due to these reasons, reported studies in literature mainly focus on the evaluation of TypeI residual stress [29]–[31].

2.4.2 Residual Stresses in Metal Additive Manufacturing

During the additive manufacturing of metals, high thermal gradients and high cooling rates on the order of $10^3 - 10^8$ K/s occur due to the localized heat input. Considering subsequent layer deposition in SLM, when the upper portion of the layer melts, the layer below liquid line also is heated up and expands. This expansion is restricted by underlying cooler material and causes residual compressive stress in upper part and tensile stress in the lower part. On the other hand, when the heat source moves away, the upper layer cools down and shrinks at faster rates than the bottom layer therefore leads to tensile residual stresses in the upper part and compressive stresses in the bottom part. An illustration is given in below Figure 5;

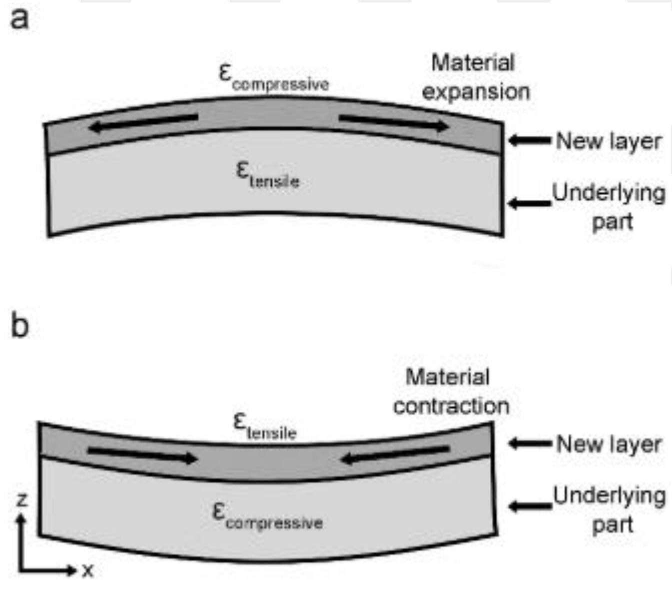

Figure 5: Residual Stress formation in Additive Manufacturing a) During heating b) During cooling [30]

If the amount of these restrictions are high enough, stresses can reach the yield strength of the material and lead to plastic deformation. It is important to notice that material deformation is easier at elevated temperatures due to the decrease in yield strength. The rapid heating-cooling cycles caused by high heat energy input during

SLM process cause uneven expansion-contraction on the material due to thermal expansion and phase transformations, resulting in residual stresses [32].

In SLM processes, the residual stress that occurs in the material due to high heat input and high cooling rates during the manufacturing stages and the resulting shape and size changes (distortions) are the main problems affecting product quality and manufacturability. Attemps of increasing product quality by trial/error approach result in serious loss of time and money. Apart from limiting the manufacturability (crack formation, warping, recoater contact, etc.) and dimensional accuracy, the residual stresses adversely affect the mechanical properties of the product, especially the fatigue performance.

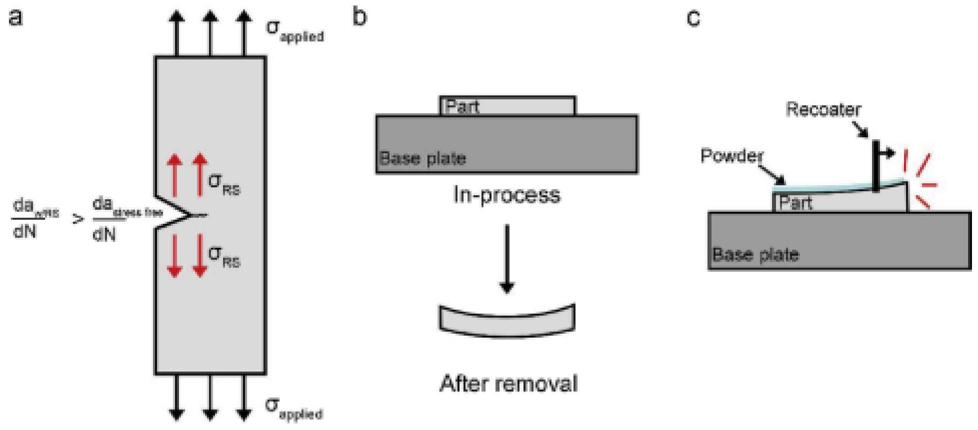

Figure 6: Negative effects of residual stress in metal AM a) reduced fatigue performance due to tensile residual stress b) deformation after cutting from baseplate c) residual stress causing distortion and resulting in recoater contact [30]

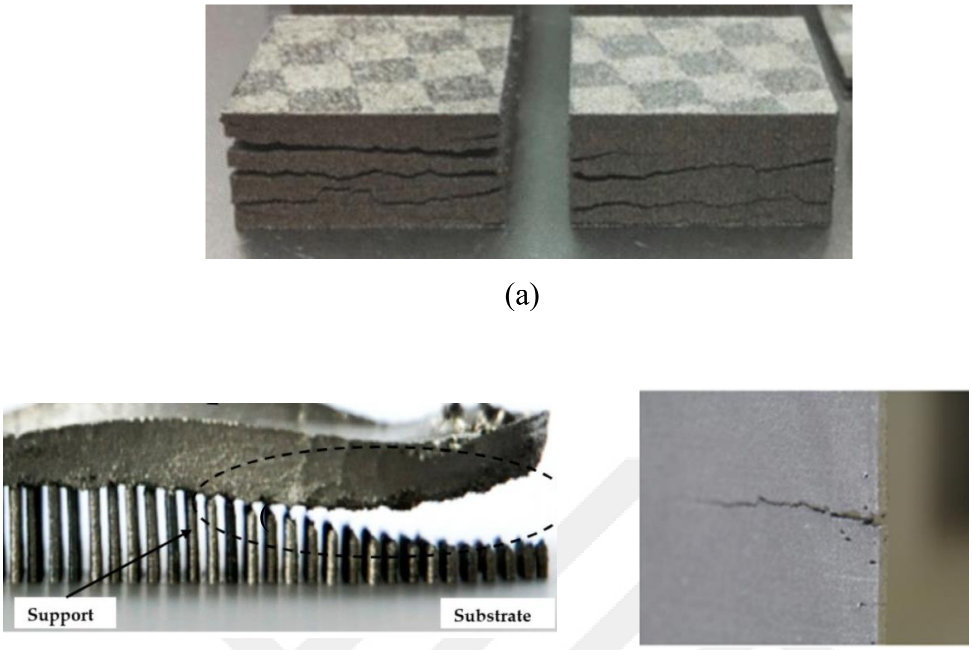

(a)

b) (c)

Figure 7: Failures due to residual stress a) delaminations b) seperation from supports c) cracks [33] [34]

The images of micro-cracks caused by residual stress in the part are shown in below figure;

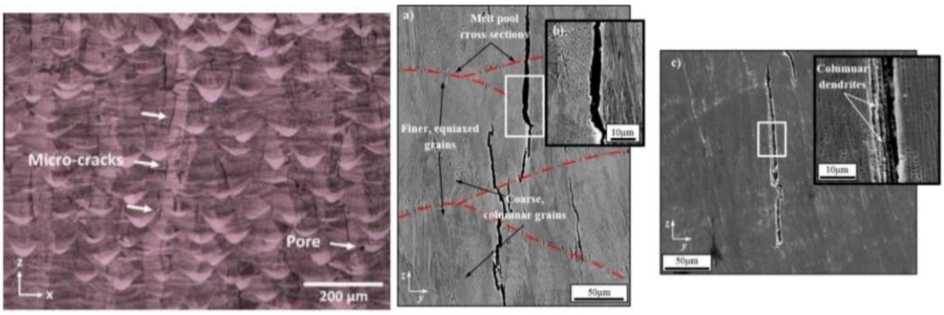

Figure 8: Microcracks caused by residual stress formation during SLM processing [35], [36]

If distortion and/or cracks do not occur in the parts produced by metal AM, the residual stresses can be relieved by applying heat treatment to some extent. However, if a high amount of residual stress has developed in the part during production, distortions and/or cracks occur in the final part with the relaxation of the residual stresses during heat treatment, even if the part does not warp after manufacturing.

The distortions that occur in the part cause the geometric tolerance of the product not to be achieved, additional straightening processes and a decrease in product quality. In addition, as seen in below figure, if these distortions in the material occur during build stage, the part and the recoater blade collide, causing the blade to be damaged and even build may stop.

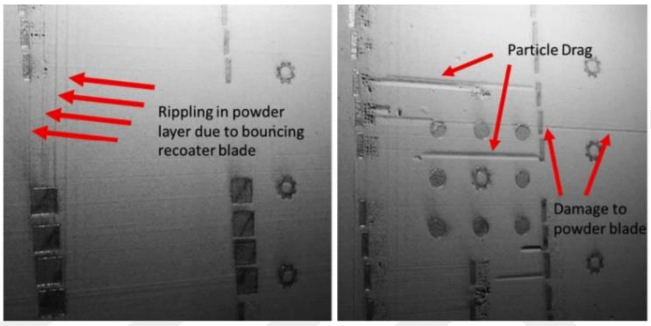

Figure 9: Process failure due to damaged recoater blade.

Additionally, expensive metal powder combined with the long process time leads to serious financial losses in case of failure. As a result, residual stresses and distortion are major problems for both product quality and production efficiency, and these problems need to be predicted and precautions should be taken.

2.4.3 Factors Affecting Residual Stress

2.4.3.1 Thermal Gradient

For the illustration of welding residual stress formation, a common example is the three bar analogy. Initially at equal length and temperature connected at the ends end they are at zero stress. When the middle bar is heated without connection, there is no residual stress after reaching equilibrium temperature; however, when the middle bar is connected to others, residual stress remains in components having reached the room temperature (middle bar in compression, side bars in tension) [37]

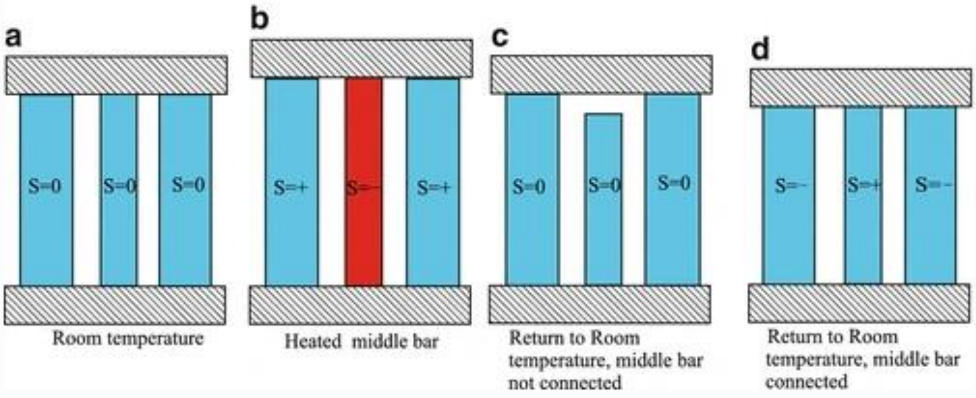

Figure 10: Three bar analogy of residual stress formation

2.4.3.2 Phase Transformation

In the case of phase transformation of steels, it is proven that the solid state phase transformation has significant effect on residual stress and distortion of welded components due to the transformation strains [39]. In their work, Stone et al. have proven that in welding process, phase transformation strains may completely neutralize the strains due to thermal contraction near the melt pool.

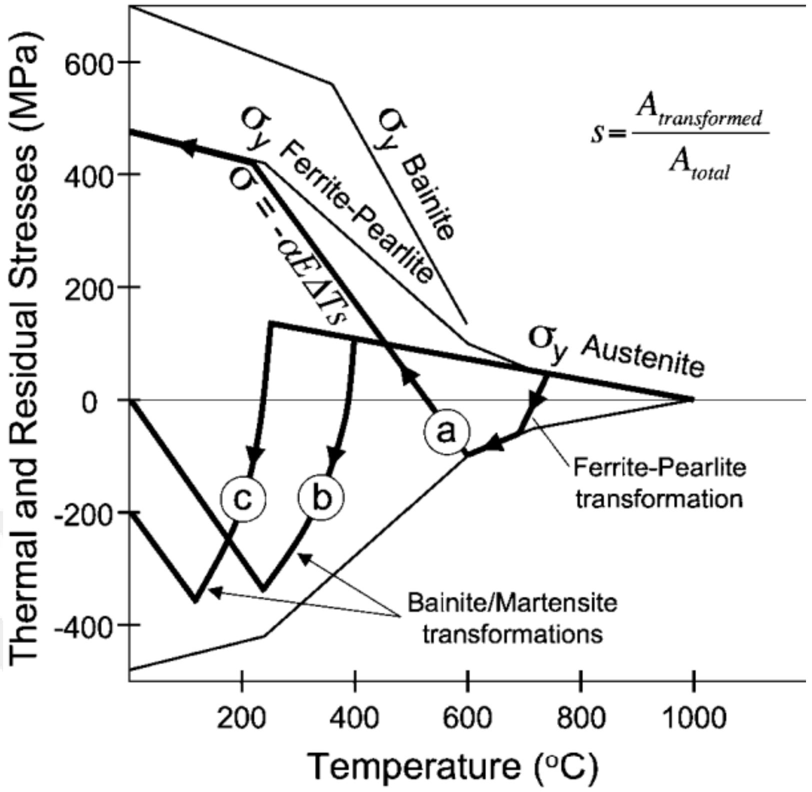

Figure 11: Axial stress evolution during cooling in welded steel undergoing phase transformations [40]

Steels have variety of micrustructures and phases because atoms that make up the steel have plenty of ways to accomplish the same allotropic transformation. Transformation can occur by either reconstructive or displasive (shear). In reconstructive transformation, constituting atoms break bonds and rearranged in a different structure and diffusion of atoms is the main mechanism. On the contrary, displasive transformation takes place by homogenous deformation of the parent crystal structure into a new crystal structure and the transformation is diffusionless (time independent) [41].

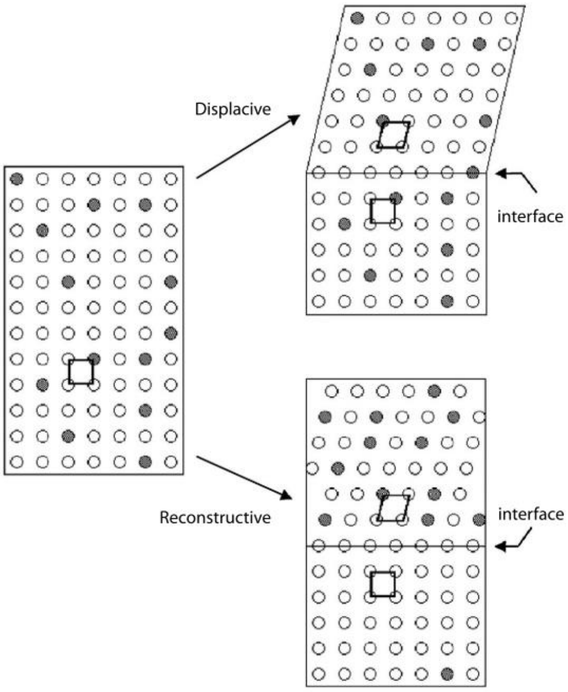

Figure 12: Mechanisms of Displasive and Reconstructive phase transformations

Steel phases and regarding transformation type from austenite is given below.

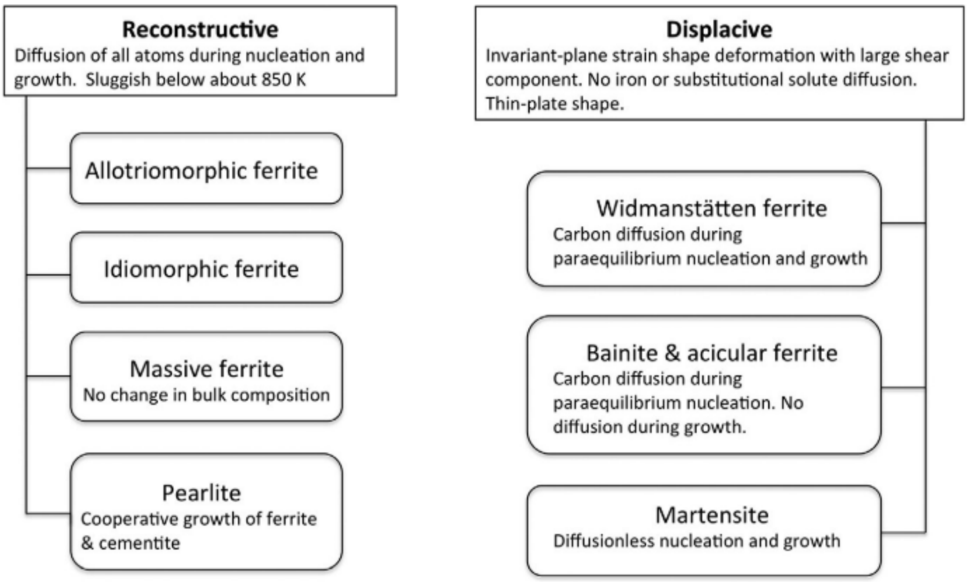

Figure 13: Steel phases and regarding transformation types [41]

Note that the austenite to martensite transformation is an athermal transformation, the fraction of phase transformed depends on the amount of undercooling below the martensite start temperature. Time independent nature of austenite to martensite transformation is explained by Koistinen and Marburger [42];

$$Xm = Xa0\ (1 - e^{-k(MS-T)}$$

Where;

Xa0 is Austenite fraction at the beginning of transformation,

XM is fraction of Martensite at any temperature,

k is Koistinen-Marburger parameter

T is Temperature,

Ms is Martensite start temperature

Due to the similarities of welding and metal additive manufacturing, phase transformation strains are needed to be taken into account for additive manufacturing build stage and the following heat treatment process if the material undergoes phase transformation.

Understanding the phase transformation mechanism in steel is crucial for the study of thermal/thermomechanical treatments as well as computer modelling of residual stress formation in steel. In dilatometry test, continuous heating and cooling cycle is applied on a material and resulting dimensional change is recorded with varying temperature. In the linear regions of the dilatometry curve, there is no transformation and linear thermal expansion coefficient can be calculated. If there is a volume change during phase transformation, dilatometry curve deviates from linearity and therefore test can capture transformation temperature and strain. By extrapolation of linear regions locating at phase transformation boundaries, fractions of the transforming phases at specific temperature can be calculated by lever rule [43].

2.4.3.3 Process Parameters

Scan Strategy: Long scanning vectors causes in accumulation of residual stress. Moreover greatest stress component is developed parallel to the scan vectors, resulting in anisotropic residual stress distribution.

In practice, residual stress distribution is dependent on scanning strategy which affects the thermal history of built part. In literature studies reported that the highest stress tensor component is developed parallel to the scan direction, i.e at specific moment, if the laser is moving through the X direction, σx is developed as highest component due to higher thermal gradient along X direction. Moreover, with increasing scan vector length, developed stresses also increase [34] [44] [45] [46] [47] [48].

2.4.3.4 Material Properties

In their study, Zhu et al. stated that effect of thermal expansion coefficient has a moderate effect on the simulation of residual stress and distortion, however yield stress is a key property for achieving correct results. While other parameters, such as thermal conductivity, Young’s Modulus, have small effects, specific heat and density have negligible effects on results [49]. Similarly, in another study, Vracken et al. studied the effect of material properties. In addition to the thermal expansion coefficient, they draw attention to the importance of the melting temperature, since the shrinkage occurs in the higher temperature range as the melting temperature increases for alloys such as Ti6Al4V. They observed no distinguishable trends for the effect of thermal diffusivity. Their conclusion is also that yield stress values at high temperatures are important for the correct results. However no distinguishable correlation is observed for the effect of thermal diffusivity even solidification theory indicates that materials with lower thermal diffusivity results in higher residual stress as the accumulated heat cannot be dissipated and large thermal gradients and residual stresses develop for materials with lower thermal diffusivity [50]. In another study, Yakout et al. studied the influence of thermal properties on residual stress for SLM'ed aerospace alloys. The studied alloys were Invar 36, 316L and Ti6Al4V. They reported that while Invar 36 has the lowest residual stress levels due to its low thermal expansion coefficient, Ti6Al4V has the highest levels due to its low thermal diffusivity. However, effect of yield stress is not considered [51]. Considering above studies, it is obvious that CTE is an important parameter which directly affects the residual stress levels of a material. The thermal stress in a material having a thermal gradient is given by;

$$\sigma = \alpha \, E(T - Tref)$$

Where σ is the thermal stress,

α is the thermal expansion coefficient,

E is the young's modulus,

T is temperature and

Tref is the reference temperature.

Note that CTE directly influences the thermal stress in a material. On the other hand, thermal diffusivity is the ability of a material to how fast it can dissipate heat which is given by;

$$D = \frac{k}{\boldsymbol{\rho \, Cp}}$$

Where D is the thermal diffusivity,

k is the thermal conductivity,

ρ is the density and

Cp is the heat capacity.

Note that thermal diffusivity indirectly effects thermal stress by effecting thermal gradient in a material.

2.5 Experimental Approaches for Measurement of Residual Stress

Experimental approaches for residual stress measurements are indirect way of measuring stresses; instead stresses are calculated over measured strain. Techniques for measurement of residual stresses can be classified as destructive and non-destructive. Destructive techniques involve cutting away some part of a bulk material containing stress then deformation response is measured and stresses are calculated from deformation. Some of the frequently used destructive techniques are contour method, crack compliance and hole drilling. Each technique have its own specific calculation procedure but the main principle is the same. [52]. On the other hand, non-destructive techniques requires sensitive calibration.

For the accurate selection of the residual stress measurement techniques, one shall consider accuracy of the measurement, resolution and steate of the material to be measured like stress magnitude and gradient. Common residual stress measurement techniques and their specifications are given below figure; [53]

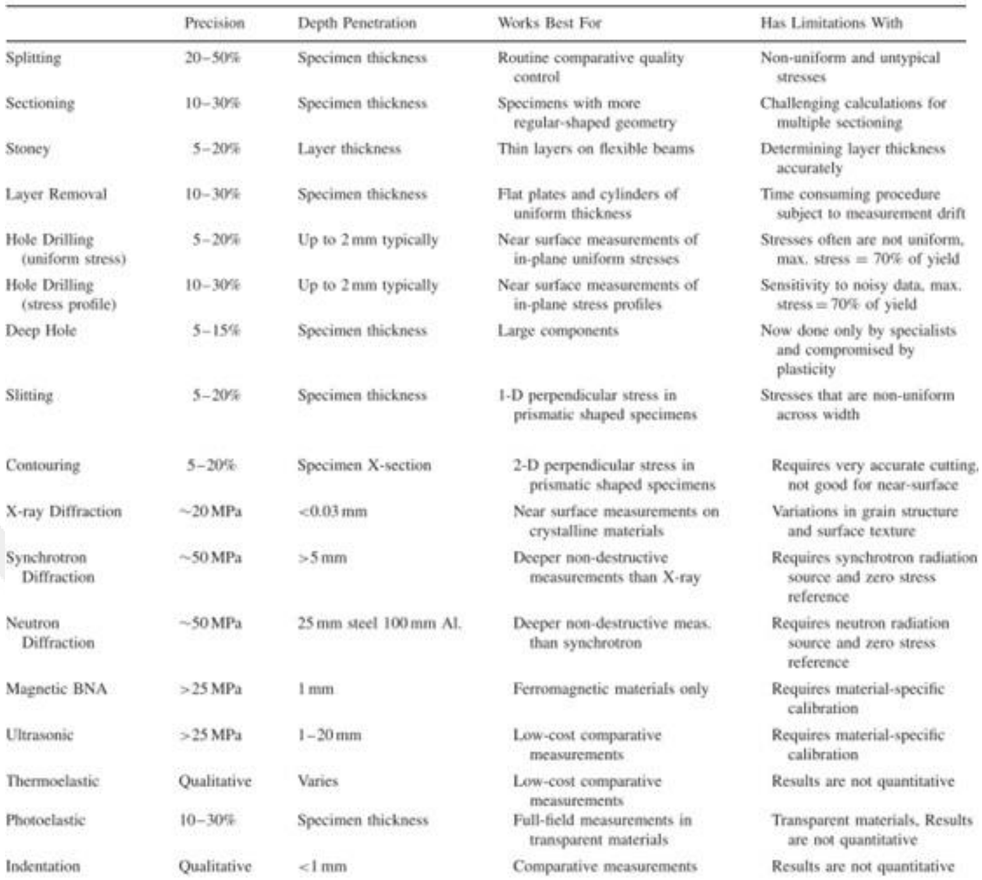

	Precision	Depth Penetration	Works Best For	Has Limitations With
Splitting	20–50%	Specimen thickness	Routine comparative quality control	Non-uniform and untypical stresses
Sectioning	10–30%	Specimen thickness	Specimens with more regular-shaped geometry	Challenging calculations for multiple sectioning
Stoney	5–20%	Layer thickness	Thin layers on flexible beams	Determining layer thickness accurately
Layer Removal	10–30%	Specimen thickness	Flat plates and cylinders of uniform thickness	Time consuming procedure subject to measurement drift
Hole Drilling (uniform stress)	5–20%	Up to 2 mm typically	Near surface measurements of in-plane uniform stresses	Stresses often are not uniform, max. stress = 70% of yield
Hole Drilling (stress profile)	10–30%	Up to 2 mm typically	Near surface measurements of in-plane stress profiles	Sensitivity to noisy data, max. stress = 70% of yield
Deep Hole	5–15%	Specimen thickness	Large components	Now done only by specialists and compromised by plasticity
Slitting	5–20%	Specimen thickness	1-D perpendicular stress in prismatic shaped specimens	Stresses that are non-uniform across width
Contouring	5–20%	Specimen X-section	2-D perpendicular stress in prismatic shaped specimens	Requires very accurate cutting, not good for near-surface
X-ray Diffraction	~20 MPa	<0.03 mm	Near surface measurements on crystalline materials	Variations in grain structure and surface texture
Synchrotron Diffraction	~50 MPa	>5 mm	Deeper non-destructive measurements than X-ray	Requires synchrotron radiation source and zero stress reference
Neutron Diffraction	~50 MPa	25 mm steel 100 mm Al.	Deeper non-destructive meas. than synchrotron	Requires neutron radiation source and zero stress reference
Magnetic BNA	>25 MPa	1 mm	Ferromagnetic materials only	Requires material-specific calibration
Ultrasonic	>25 MPa	1–20 mm	Low-cost comparative measurements	Requires material-specific calibration
Thermoelastic	Qualitative	Varies	Low-cost comparative measurements	Results are not quantitative
Photoelastic	10–30%	Specimen thickness	Full-field measurements in transparent materials	Transparent materials, Results are not quantitative
Indentation	Qualitative	<1 mm	Comparative measurements	Results are not quantitative

Figure 14: Common residual stress measurement techniques

2.5.1 Contour Method

The primary advantage of contour method is 2D map of residual stress measurement. Other measurement techniques like X-Ray Diffraction, Neutron Diffraction and hole drilling yields single residual stress profile lines. The method is based on the fact that the stress component perpendicular to the cut plane is relaxed because, the perpendicular stress component is zero by definition on a new free surface. As a consequence of stress relaxation, elastic deformations on the cut surface occurs. By inverse analysis and Bueckner’s superposition principle, returning back the cut surface to its prior position, stress field just before the cutting step can be calculated. Following assumptions are done for the application of contour method [54];

1. Resulting deformations after cutting is caused by pure elastic relaxation of stress
2. The cutting plane is symmetric, flat and has an infinitesimal thickness.
3. Cutting stage does not introduce stresses which affect measured displacements

Only deformation component which is normal to the cut direction is taken into account. Applying the other components also gives the same results due to the Poisson contraction. On the other hand, it is impossible to identify shear stresses therefore only normal stresses can be identified. However in real case there exist shear stresses and in plane displacements. To overcome this error, both side of the contour surfaces should be measured and averaged. By doing so, error caused by in plane displacements and shear stresses are cancelled and so resulting displacements are only because of the release of residual stress component normal to the cut plane. It is sensible that modelling the cut plane of the part as flat and applying the measured cut surface with opposite sign to the flat cut plane results in same stress field with the applying the measured deformation by keeping the sign constant and forcing the surface back to the original flat plane since the deformation of the cut surface is very small comparing to the part [55].

In order not to affect the stress distribution, the cutting is done with EDM (Electric Discharge Machining). The assumptions of the contour method are made based on the thickness of the cut plane is infinitesimally small, flat and the cutting procedure introduces no plastic deformation. Therefore EDM is the proper cutting technique for contour method. Below the schematic of the EDM cutting process is given;

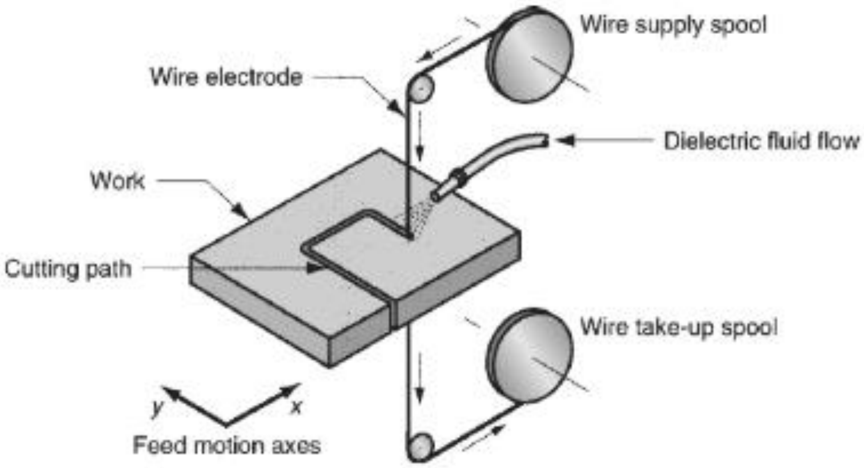

Figure 15: Schematic of EDM Cutting [56]

For the EDM cutting process, the direction of cutting is an also important parameter since it effects the way of stress relief. If the stress distribution on the part can be forecasted, cutting perpendicular to the dominant stress component resulting in balanced stress relief. It should be noted that for SLM'ed components, stresses along the build direction (Z-normal stress) is more dominant compared to in plane stresses [57]. Therefore to cut properly, cutting should be carried out perpendicular to the build direction.

As cutting proceeds, stress is relieved and part may move so in order to prevent this error clamping before cutting is necessary for proper cutting. The use of clamps prevents deviaton of the cut surface from planarity and therefore minimizes the errors of cutting. For fine cutting, EDM wire with a diameter of 100µm is reported to be the optimum thickness for the cutting procedure. Procedure for the contour residual stress measurement method is given below;

1. Part is cut through by EDM. A flat cut is required.
2. Both cut surfaces of pieces are measured by CMM.
3. Both surface contours are averaged.
4. Averaged surface data is fitted to be able to evaluate the surface coordinates at arbitrary points.

5. A finite element model is constructed representing the cut part.
6. Negative of the fitted cut surface contour is defined as displacement boundary condition on the part cut surface in FE model.
7. After simulation run is completed, resulting stresses are prior stress distribution before cutting.

For the measeurements of the cut surface, CMM measurement is the optimum solution due to its availability, speed, high accuracy and resolution at the scale of the problem. Other than CMM, laser measurements are also possible however the accuracy is low compared to CMM.

There are 2 reasons of the need for data fitting. Firstly, CMM measurements includes noises or measurements error and fitting eliminates these noises. Secondly, the measured surface data points are discrete and these points don't exactly belong to the nodes of the further finite element model. Fitting enables to exactly assign the measured displacements as displacement boundary condition to the nodes of the model. In general, spline fitting is applied for the fitting of the measured surface contour.

2.6 Numerical Approaches for Predicting Residual Stress

Considering the scale of the problem, macro-level residual stresses are the dominant stresses and macro scale finite element modelling approaches would be appropriate for the solution of the problem [58].

2.6.1 Finite Element Method

2.6.1.1 Modelling Scales

In order to effectively solve the problem, necessary modelling scale should be determined. In literature, there are three different modelling scales for the modelling of residual stress and deformation; these are micro scale, meso scale and macro scale modelling. For a microscale model, melt pool characteristics such as convection, surface tension and other particle behaviour are examined. For the mesoscale modelling, without considering the individual particle behaviour or melt pool dynamics, distinct laser patterns and phase transformations, resulting thermal cycles and mechanical responses are examined. However, even for a model with a $36mm^2$ scan area, a detailed analysis takes 92 hours to solve [59]. On the other hand, macroscale approach involves full scale part modelling of AM components. For the selective laser melting of a part with 100 mm length, depending on the powder layer thickness, nearly 3000 times of powder layer recoating is necessary to complete the build. Therefore it is computationally very demanding to simulate a part scale model considering all the physics including scan strategy, powder-laser interaction or melt pool dynamics together with the non-linear material properties etc and actual constructuion of part with too much layerrs. In order to overcome such computational load, some assumptions or simplifications are required. Macroscale modelling approach therefore do not exactly reflect the actual thermal cycles exactly. It is still required to develop more accurate and efficient macroscale modelling. [60]

2.6.2 Thermal Modelling Approach

Governing heat transfer equation is given as;

$$\rho C_p \frac{dT}{dt} = -\nabla \cdot \boldsymbol{q}(\boldsymbol{r}, t) + Q(\boldsymbol{r}, t)$$

Where;

ρ is is the density of the material,

Cp is specific heat capacity,

T is temperature,

t is time,

Q is rate of heat generation.

Fourier heat flux constitutive relation is given by;

$$\boldsymbol{q} = -k\nabla T$$

Where k is the thermal conductivity.

∇T is thermal gradient

Heat transfer due to convection is given by;

$$q_{conv} = h(T_s - T_\infty)$$

Where h is the convective heat transfer coefficient,

Ts is surface temperature of object and

T∞ is the ambient temperature.

Stefan-Boltzmann law:

$$q_{rad} = \varepsilon\sigma({T_s}^4 - {T_\infty}^4)$$

Where ε is the emissivity,

σ is Stefan-Boltzmann constant,

Ts is surface temperature of object and

T∞ is the ambient temperature.

2.6.3 Thermo-Mechanical Modelling Approach

In the thermo-mechanical modeling approach, the thermal and mechanical solutions of the process are combined in a single simulation. The temperature changes and the residual stresses and distortions caused by each time step in the simulation are analyzed. An important advantage of this approach is that it can realistically simulate the "scan pattern" and "moving heat source", which are important variables that greatly affect the residaul stress field developed during metal AM processes. However, this approach requires high computational power and the computations become more and more complex as the number of layers increases, executing a realistic simulation can take days, weeks or even months, except for small blocks consisting of several layers. As the time proceeds, number of layers increases and it is getting more difficult to handle the materials non-linearity and hence calculations become more complex. Also accurate prediction of residual stresses require accurate measurement of temperature dependent material properties. For this reason, it is practically difficult to simulate a part scale geometry [61].

Shen et al. developed 2 layered (4x2mm) model for EBM for thermo-mechanical analysis. The temperature dependent material properties are defined and the powder/solid phase-change is implemented together with an unspecified model that takes into account the viscous dissipation. However, the mechanical behaviour of the powder is not clearly outlined and the results are only validated with literature data. Nonetheless, results are consistent [62]

Labudovic et al. developed a small single-scan detailed DED model and thermo-mechanical analysis is ran. Continuous material addition is modeled but powder behaviour is not. The output results are compared with the XRD measurements and it is concluded that the results are consistent with XRD measurements. All studies presented considers realistic heat source and layer addition. However the scale is small; a few layer addition is modeled due to the computational demand of thermo-mechanical modeling approach [63]

2.6.4 Mechanical Modelling (Inherent Strain) Approach

For inherent strain modelling approach the size of the aforementioned problem for thermo-mechanical simulation is significantly reduced. In inherent strain modelling approach, no thermal analysis is performed therefore reducing the solution time considerably, making the modelling approach practically applicable to the real product. This approach assumes that each laser seam has same temperature history and offers complete mechanical solution. Predetermined inherent strain tensors are assigned in the linear elastic finite element formulations. The main logic of this approach is that the elastic stresses will relax when the parts cool down to room temperature due to the fact that the welded parts are not fixed, so that the previously calculated plastic strains can be applied directly as an initial tension in the new simulation [64] [65] [66].

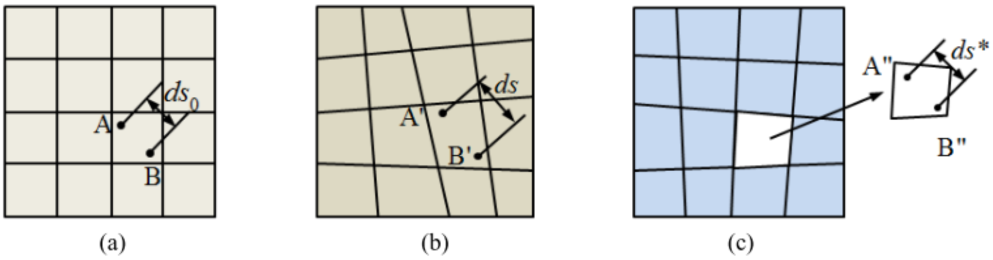

Figure 16: Schematic representation of inherent strain: a) standard state, b) stressed state, c) stress-free state [67]

Due to the physical similarity of welding process and additive manufacturing process, the inherent strain method has been successfully adapted to additive manufacturing. This adaptation to additive manufacturing is based on applying the pre-calculated residual plastic strain tensors by the addition of each layer [64]. A schematic representation of Inherent Strain approach is given below figure;

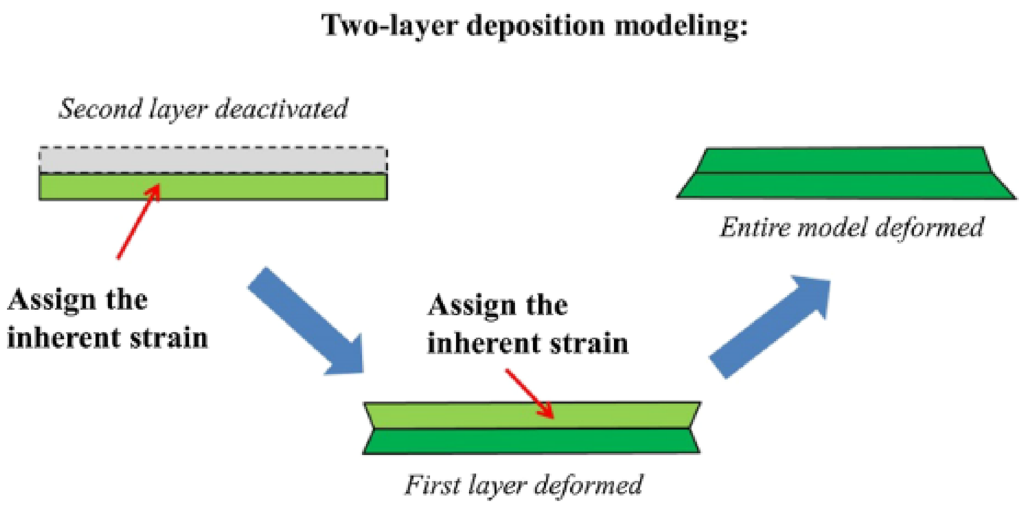

Figure 17: Inherent Strain Approach [68]

The inherent strains are dependent on the material properties and the process parameters and can be defined in the following way;

The total strain is defined as the summation of elastic strain, plastic strain, thermal strain and phase transformation strain;

$$\varepsilon\text{total} = \varepsilon\text{e} + \varepsilon\text{p} + \varepsilon\text{thermal} + \varepsilon\text{phase}$$

The inherent strain, ε^*, is defined as the difference between the total residual strain and the elastic strain;

$$\varepsilon^* = \varepsilon\text{total} - \varepsilon\text{e}$$

The inherent strains are therefore the summation of unrecoverable strains; including the plastic, thermal and phase transformation strains. Using elastic FEM, residual stresses can be calculated from inherent strains according to following equations;

$$[K][u] = [f^*]$$

$$f^* = \int [B][D][\varepsilon *] dV$$

Where [K] is the elastic stiffness matrix, [u] is the nodal displacement vector, f* is the nodal force vector induced by the inherent strains. When the displacement vector [u] has been solved, the total strain, ε and consequently the residual stress, σ, can be calculated.

$$\varepsilon = [B][u]$$

$$\sigma = [De] ([\varepsilon tot] - [\varepsilon *])$$

Where [B] is the nodal deformation matrix and [De] denotes the material elastic matrix.

The inherent strain method was originally introduced in 1975 as a practical and quick solution for welding residual stress problems. The main logic of this approach is that the elastic stresses will relax when the parts cool down to room temperature due to the fact that the welded parts are not fixed, so that the previously calculated plastic strains can be applied directly as an initial tension in the new simulation [69] [70]. Due to the physical similarity of welding process and additive manufacturing process, the inherent strain method has been successfully adapted to additive manufacturing [71]. This adaptation to additive manufacturing is based on applying the pre-calculated residual plastic strain tensors by the addition of each layer. Inherent strains can be obtained by 2 ways; either carrying out micro-scale thermomechanical simulation or building cantilever beams and measuring the distortion [65] [72] [73].

An important advantage of the inherent strain modelling approach is the size of the aforementioned problem for thermo-mechanical simulation is significantly reduced. In inherent strain modelling approach, no thermal solution is produced thus solution time is considerably reduced, making the modelling approach practically applicable to the real product. This approach assumes that each laser seam has same temperature history and therefore results in complete mechanical solution. Predetermined inherent strain tensors are assigned in the linear elastic finite element formulations [74] [75].

Siewart et al. additively produced small test samples by LBM and residual stresses have been measured by XRD. Inherent strain values are extracted from distortion simulation of cross-cantilever beam. Results have been compared with the inherent strain model results. Before XRD measurements, etching is applied to the surface of the part. It is concluded that despite the simplification of the modelling approach, simulation results show good consistency with the XRD measurements. However, the part geometry is simple prismatic and dimensional difference from the calibrated part is small which increases the accuracy of results [76].

Chen at al. extracted inherent strain values from a detailed small-scale thermo-mechanical simulation and 2 different part scale mechanical models (big and small geometries) are simulated with the assignment of extracted inherent strains. The simulation results are compared with experiment results and concluded that deviation from experimental results increases as the geometrical difference between sample part and the calibration part [65].

2.6.5 Element Birth and Death

Imitation of SLM process in simulation softwares requires a procedure so called element activation. To do that, elements are kept quiet; material properties are not assigned to elements until making contact with the laser heat source [77].

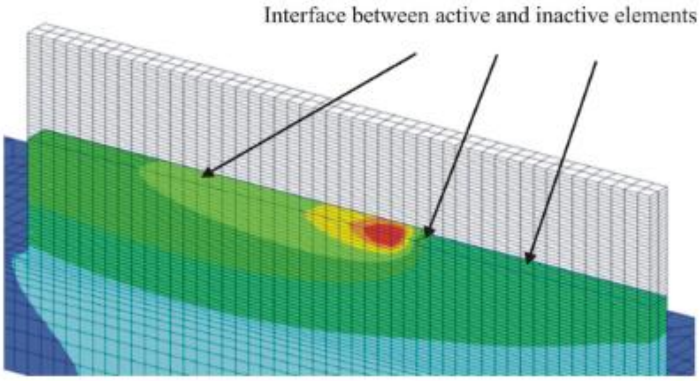

Figure 18: Element Activation Procedure[77]

2.7 Calphad Approach

For the modelling of phase equilibria of multi-component systems, CALPHAD methodology based thermodynamic modelling is a widely accepted technique. Equilibrium solidification can also be extended to non-equilibrium solidification by the Scheil-Gulliver model [78].

Variety of thermophysical properties needed can be accurately calculated as a function of time, temperature or cooling rate with JMatPro software and the calculated data can be used as input for the Finite Element simulations. For the simulation of residual stresses and distortions for additive manufacturing and post-heat treatment, the following material data are needed:

- Temperature dependent material properties (thermal conductivity, density, thermal expansion coefficient, Young’s Modulus)
- Enthalpy change during phase transformations

- Data related to the phase transformation (TTT-CCT, MS, MF, Koistinen Marburger parameters),
- Temperature dependent flow curves [79]

To calculate each property, fractions of all constituent phases present are calculated for each temperature

Calculated above parameters can either be as for each constituent phase seperately (Multi-Phase Material) or can be averaged into a single data set (Single Phase Material).

2.8 FEA Software Tools

MSC Software has varying tools for many processes such as welding, joining

and additive manufacturing. A large variety of treatments can be simulated to yield sufficient components. Simufact Additive deals with the additive manufacturing processes, more specifically Selective Laser Melting. MSC Simufact creates simulation possibilities such as:

- Determination of the final shape by predicting distortions and residual stresses.
- Detection of possible part and process failures.
- Verifying the process parameters before starting the real build.

ABAQUS on the other hand, is a general purpose finite element software. In this study, both Simufact Additive and ABAQUS softwares are made use of.

2.9 Dilatometry Test

One of the assumptions of the phase transformation model constructed from the dilatometry curve is the phase transformation strain is isotropic since the dilatometry test record only the linear change with respect to temperature. However, phase transformation volume change occurs anisotropically as shown in below figure; [43] [80].

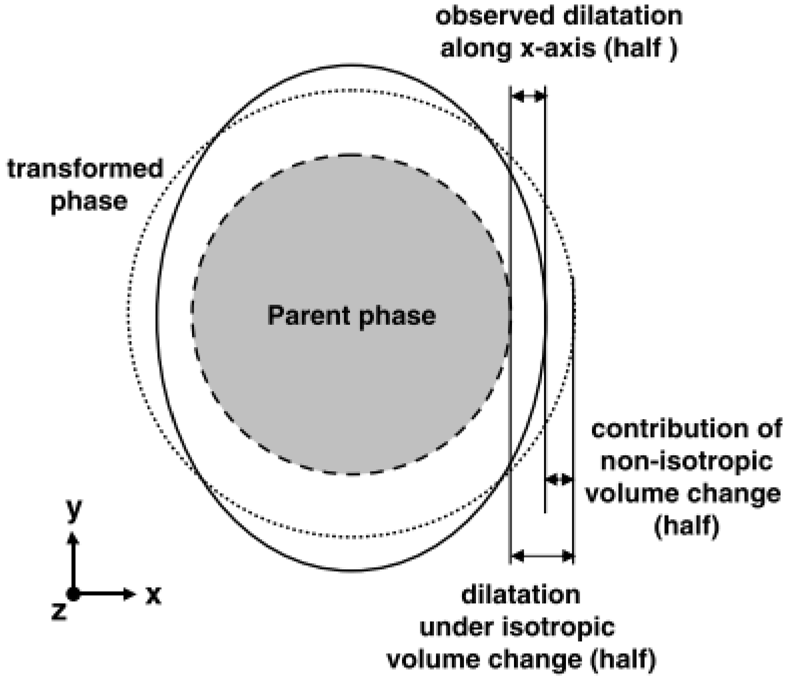

Figure 19: Dilatation during phase transformation

CHAPTER 3

EXPERIMENTAL PROCEDURE

Study methodology is divided into 2 main phases. First phase is the experimental studies. Experimental characterisation of 17-4 PH SS together with part scale measurement of distortions and residual stresses are carried out.

The second phase involves numerical analysis for the calculation of residual stress and distortions. In this phase, both thermo-mechanical and mechanical modelling approaches of Finite Element Method are going to be used. Aforementioned advantages of both modelling approaches are discussed.

3.1 Starting Materials

As a starting material, commercial 17-4 PH Stainless Steel Powder (LPW Technology, Carpenter Additive) are used. Particle size distribution is measured by Camsizer X2 particle analyzer. Measurement result is given below where D10=21 µm, D50=30 µm and D90=41 µm.

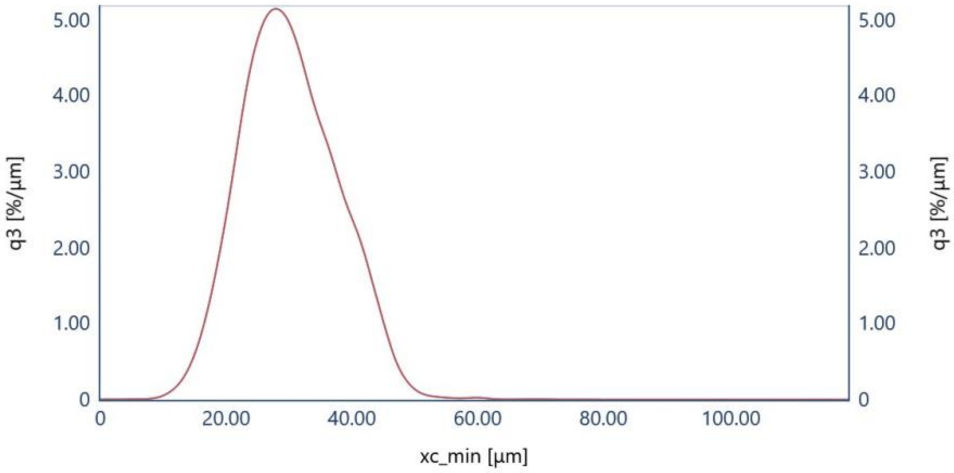

Figure 20: Particle Size Distribution

SEM analysis of gas atomized 17-4 PH SS powder is given below where the great majority of powder are spherical and some satellite powder can be seen.

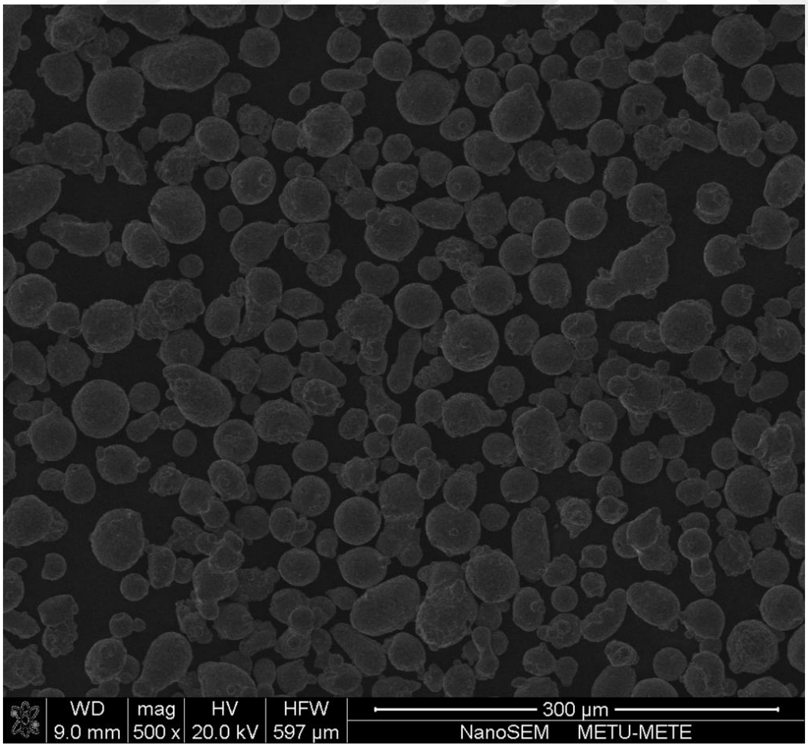

Figure 21: SEM image of gas atomized 17-4 PH SS powder

EDS analysis of starting powder is given below where the chemical composition of constituent elements fall into standart range.

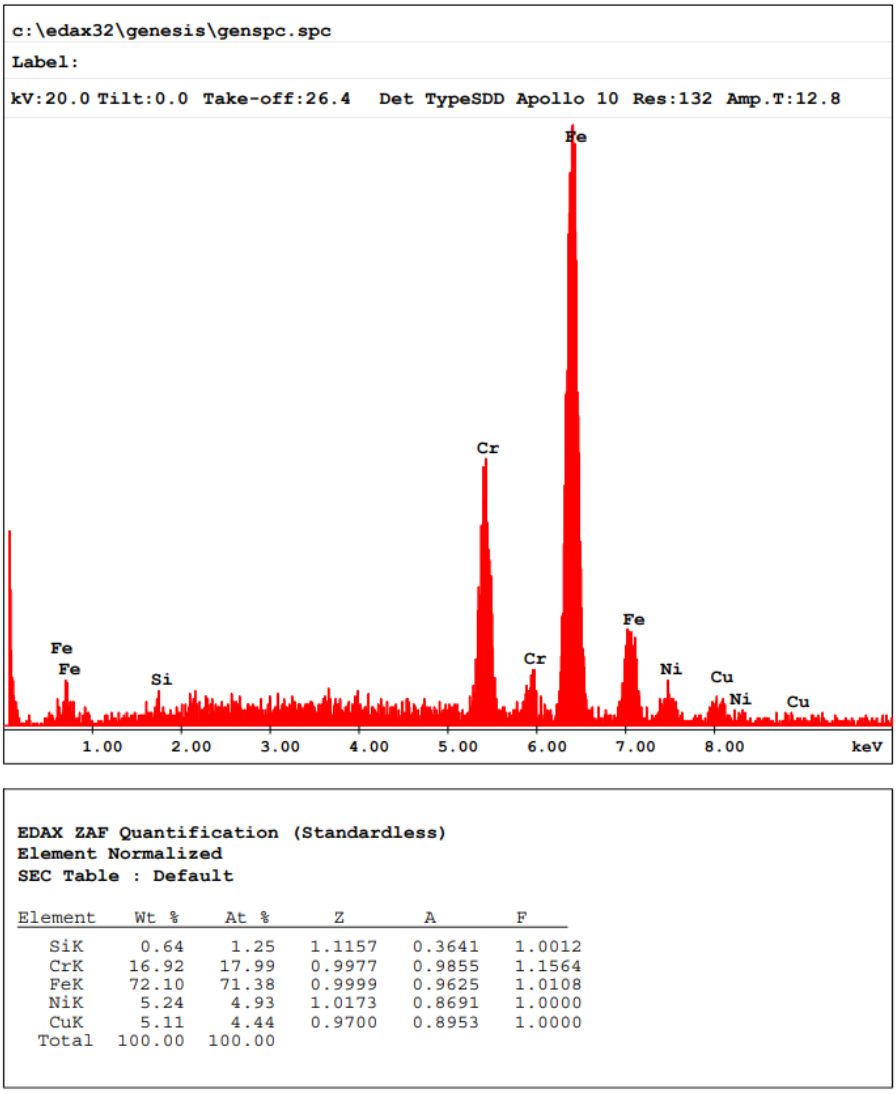

```
c:\edax32\genesis\genspc.spc
Label:
kV:20.0 Tilt:0.0  Take-off:26.4   Det TypeSDD Apollo 10  Res:132  Amp.T:12.8
```

```
EDAX ZAF Quantification (Standardless)
Element Normalized
SEC Table : Default

Element    Wt %     At %       Z         A         F
   SiK     0.64     1.25    1.1157    0.3641    1.0012
   CrK    16.92    17.99    0.9977    0.9855    1.1564
   FeK    72.10    71.38    0.9999    0.9625    1.0108
   NiK     5.24     4.93    1.0173    0.8691    1.0000
   CuK     5.11     4.44    0.9700    0.8953    1.0000
  Total  100.00   100.00
```

Figure 22: EDS analysis of 17-4 PH SS powder

3.1.1 Selective Laser Melting Equipment

Renishaw AM400 consist of pulsed-mode single Yb-fiber maximum laser power of 400 W with a wavelength of 1064 nm is used to build desired parts. Laser spot diameter is 70 µm. Argon or Nitrogen is used as gas atmosphere, where the oxygen levels don’t exceed 100 ppm during process. Baseplate material is AISI 1117 Carbon Steel and the dimensions of baseplate is 250x250x30mm.

3.2 Optimised SLM Process Parameters for 17-4 PH

During the development stage of process parameters for a material, main focus is to maximize material density with minimum defects such as cracks, voids, porosities or lack of fusion zones in order to obtain good mechanical properties. %99 material density is the canonical lower limit for a successful process [81]–[83].

In their study, Özsoy et al studied the various combination of process parameters for the resulting part density of SLM’ed 17-4 PH for pulsed-mode laser system. Their study shows that following set of parameters resulted with the highest density which is %99.69 [84];

Table 3: Optimized Process Parameters for 17-4 PH Stainless Steel

Parameter	Value
P (Watt)	200
Exposure Time (µs)	142
Point Distance (µm)	110
Hatch Distance (µm)	110
Layer Thickness (µm)	30
Rotation Between Layers (°)	67
Laser Spot Diameter (micrometer)	70
Recoating Time (seconds)	7
Scan Pattern	Meander
Protective Environment	Argon
Oxygen Content (ppm)	< 0.05

Resulting optimised process parameters above are accepted as basis for the use of input data for simulations. By doing so, porosities and misleading evaluation of residual stresses are minimised.

3.3 Material Data

There are 5 options for selecting the input material data (Appendix A);

1. Experimental testing for each material property: Generating too many temperature dependent material parameters is expensive and time consuming as well as test infrastructure may not be available. Therefore experimental testing is applied for only critical material parameters which has a high impact on simulation results for the sake of simplification and being cost-effective.

- Coefficient Of Thermal Expansion (CTE): Dilatometry tests with sub-zero quenching were carried out for the determination of CTE. For both SLM'ed and Wrought 17-4 PH SS rods, CTE's are determined along X, Y, Z directions.
- Phase Transformation Strain: Needed for the simulation of heat treatment and calculated from dilatometry results.

2. Computationally generated material data (JMatPro): There are 2 options for CALPHAD based generation of material data by JMatPro software; Single Phase Material (SPM) and Multi Phase Material (MPM). By default, for both SPM and MPM, JMatPro calculates room temperature phase for 17-4 PH SS as martensite. However, present phase is delta ferrite for SLM'ed as built 17-4 PH. Therefore tailoring of computation results are required. While SPM is used for simulation of the build stage of SLM process, MPM is used for the post heat treatment stage due to reasons explained below;
    - JMatPro Single Phase Material: Based on Scheil-Gulliver solidification, constituent phases are calculated as delta ferrite>austenite>martensite and temperature dependent thermophysical properties are averaged into a single phase based on rule of mixture of constituent phases at every specific temperature. Utilization of material data as a single phase also enables to tailor the thermophysical properties for SLM process since SLM'ed 17-4 PH consists of single phase as delta ferrite. Thus, it is reasonable to generate JMatPro single phase material and tailor it according to the SLM'ed 17-4 PH SS. For the sake of correct reflection of process history, delta ferrite material properties are extrapolated from solidification start temperature (1450 C) down to room temperature (25 C).
    - JMatPro Multi Phase Material: Accurate prediction of residual stress and distortion induced by heat treatment process requires accurate

information of properties of constituent phases which are a function of elemental composition. For the calculation of distortion;

  - Thermophysical & Physical Data of each phase (thermal conductivity, heat capacity, thermal expansion coefficient, density) and
  - TTT/CCT diagrams are required.

3. Software databases (Simufact Material): Default 17-4 PH material offered in Simufact Material is inadequate due to
   - Constant (temperature independent) material properties
   - Insufficient flow curve. Existing for only room temperature.
   - Absence of creep data which is required for the simulation of heat treatment

Above mentioned inadequancies reasult in in calibration error as well as inaccurate results.

4. Literature data: Material properties reported in literature for 17-4 PH SS are mostly for the wrought & standard heat treated conditions. Detailed characterisation for the additively manufactured 17-4 PH SS are not reported which differs from its conventional counterparts due to high cooling rates and anisotropy. Using cast or wrought 17-4 PH material data for the simulation of additive manufacturing processes results in inaccurate results.
5. Hybrid Approach: Another option is combining above methods such as experimental determination of most sensitive parameters and calculation of less sensitive parameters depending on sensitivity analysis results. In this study, hybrid approach is selected for the generation of material data. While CTE and phase transformation strain is determined experimentally; density, heat capacity, thermal conductivity, poisson's ratio and Elastic Modulus is computed by JMatPro. Detailed information about material data is given in Appendix A

3.4 Mesoscale Model in Simufact Welding

In Simufact Additive, it is not possible to model the process parameters such as laser scanning strategy and to investigate their effects in detail due to macro scale simplifications in the software. This is acceptable since detailed part scale modelling results in serious increase in computational demand. Nonetheless Simufact Welding enables detailed modelling of welding processes where the electron beam or laser is used as a heat source. Herein due to the similarities of welding processes and metal AM processes, SLM process can also be modeled in detail for mesoscale in Simufact Welding software.

Together with Simufact Welding, MSC Apex, being a CAE specific direct modelling and meshing software, is used for model creation, meshing, dividing the model into layers and creation of laser trajectories in order to accomplish mesoscale modelling of SLM process.

For build part, a 0.5mm x 0.5 mm x 0.150 mm geometry is created and for baseplate, 0.9mm x 0.9 mm x 0.15 in MSC Apex. Then build part is meshed with hexahedral mesh of 0.01 mm and baseplate is meshed with 0.03 mm hexahedral mesh with MSC Apex Mesher. By using Slicer module in tool palette, geometry is sliced into 5 layers with layer height of 0.030 mm which is actual optimized SLM layer thickness. Then, by using Hatching module laser vectors of SLM process are created. Trajectory spacing and point spacing is selected as 0.110 mm which is hatch spacing and point distance. Angular cut selected as incremental and angle is selected as 67° for laser vector rotation in each layer. Then trajectories which represent the laser vector coordinates are created in a bounding box of 0.5mm x 0.5 mm x 0.150 mm as .csv file format.

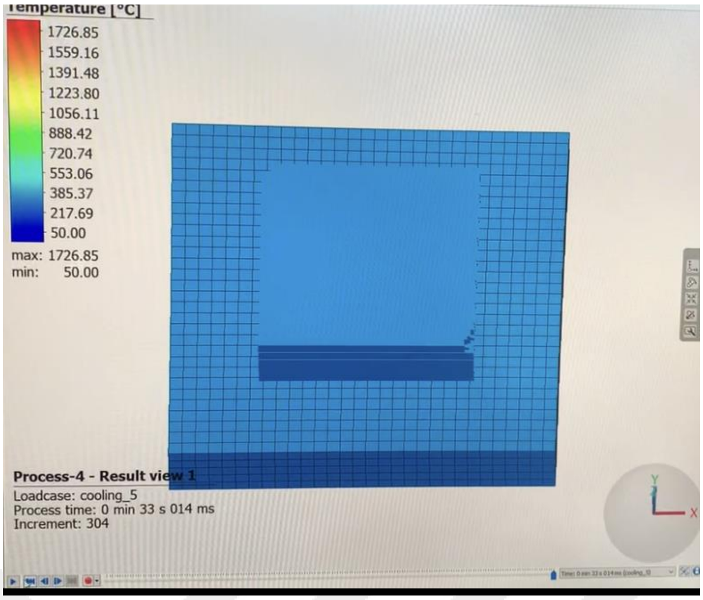

Process-4 - Result view 1
Loadcase: cooling_5
Process time: 0 min 33 s 014 ms
Increment: 304

Figure 23: Mesoscale model in Simufact Welding

Directed Energy Deposition (DED) module in Simufact Welding is used for simulations. DED module allows assignment of elements where the heat source passes. This technique is called Element Birth. Considering this technique, SLM process can also be modelled as DED process since these 2 processes are similar in principle.

Velocity is selected as 0.775 m/s, power is 200 W and efficiency is 0.4 and Gaussian parameter is 1.

Baseplate material selected as C45 material and process material is 17-4 PH SS.

Thermomechanical analysis run in presicion mode. Parallelization is activated and number of domains are selected as 2 and number of cores are 4.

3.5 Preliminary Settings and Calibration for Simufact Additive

Considering SLM'ed part and resulting residual stress field and distortions, the thermal response of the part drives the mechanical responses therefore accurate modelling of mechanical model requires accurate transient thermal model.

For the calibration procedure, one should consider the following aspects; material properties, laser properties, boundary conditions and geometry [85].

Optimized process parameters for Selective Laser Melting of 17-4 PH Stainless Steel is selected for Modelling & Simulation studies and experiental studies since optimized process parameters results in stable melting-solidification and denser products with minimum defects. Optimised process parameters used in this study is given in Section 3.2.

Simufact Additive has 3 calibration steps which requires printing of a real part in order to capture the calibration parameters for a specific material and a process parameter. These calibration parameters are given below;

1. Exposure Energy Fraction (EEF): Determined in Thermal Calibration
2. Volumetric Expansion Factor (VEF): Determined in Thermomechanical Calibration
3. Inherent Strain (IS): Determined in Mechanical Calibration

3.5.1 Mechanical Calibration

For the mechanical calibration of Simufact Addtive, 2 12x9x70 centilever beams with 0° and 90° with respect to baseplate are produced via SLM and no heat treatment was applied to the parts. Then the teeth of as-built cantilever beams were cut through their centerlines by EDM. Z-displacements on top of the beams along their longitudinal directions were recorded seperately. 4 points were measured for each cantilever beam. Values are given below;

Table 4: Measured Z-max distortions after cutting of cantilever beams

	0° Cantilever		*90° Cantilever*	
Points	*Z-Length*	*ΔL*	*Z-Length*	*ΔL.*
1 (Reference Point)	8.6560	0.00	8.6098	0.00
2	9.3768	0.7208	9.3285	0.7187
3	9.8176	1.1616	9.7353	1.1255
4	10.3896	1.7336	10.2510	1.6412

Calibration simulation is run with given measured Z-max distortions as given below;

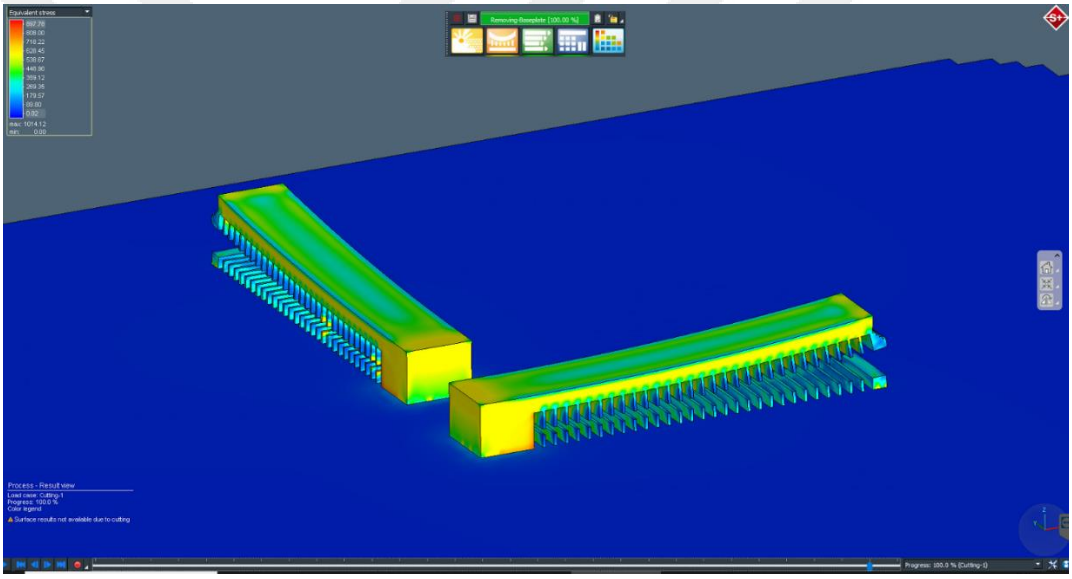

Process - Result view
Load case: Cutting-1
Progress: 100.0 %
Color legend
⚠ Surface results not available due to cutting

Figure 24: Simulation for inherent strain calibration

Once the calibration setup is arranged, software estimates the inherent strain values by solving the following optimization problem by least square method;

$$S = min \sum_{i=1}^{n} r_i^2$$

Where

r_i is the difference of maximum deflection between experimentally measured deflection and simulated deflection result where i is the number of iteration step.

According to the parameters given in tablexx and having completed the calibration procedure, the inherent strains are converged to a uniform x, y and z value which are given below,

Table 5: Calibrated Inherent Strain values

Strain Component	**Calibrated Value**
εxx	-0.00260779
εyy	-0.00246138
εzz	-0.029

3.5.2 Thermal Calibration

Exposure Energy Fraction (EEF) is required for Thermal Analysis. This approach splits the total energy input into 2 and EEF corresponds to percentage of the total energy input which actually melts the top layer of the printed part. Other portion of the energy input dissipates through the bottom of the part. For thermal calibration, peak temperature is the target value. Peak temperature and efficiency are defined as 2150 °C and 0.25 before starting the thermal calibration [86]. After calibration has finished, EEF is calculated as 23.8538.

3.5.3 Thermomechanical Calibration

Besides Exposure Energy Fraction (EEF-determined in thermal calibration), Thermomechanical Analysis also requires input data called Volumetric Expansion

Factor (VEF). Thermal strains are scaled by VEF due to the fact that single voxel mesh layer include many real powder layer. Calibration procedure of VEF is similar to the calibration of IS where the target value is the Z-Max Displacement of cantilever beam. During calibration, VEF is calculated iteratively until Z-Max Displacement is reached. Before calibrating VEF, EEF is needed to be calibrated first. Anisotropic VEF calibration results are given below table;

Table 6: Volumetric Expansion Factor (VEF) calibration results

VEF Component	**Calibrated Value**
X	0.311907
Y	0.294251
Z	0.418286

3.5.4 Simufact Additive

3.5.4.1 Mesh Size Convergence Analysis

Since the metal additive manufacturing processes don’t show excessive plastic deformation, remeshing is not critical for simulation of such kind of applications. Thermomechanical simulations run for cubes with edge length of 20 mm by varying mesh sizes. Maximum developed von mises stress at part-baseplate interface are recorded.

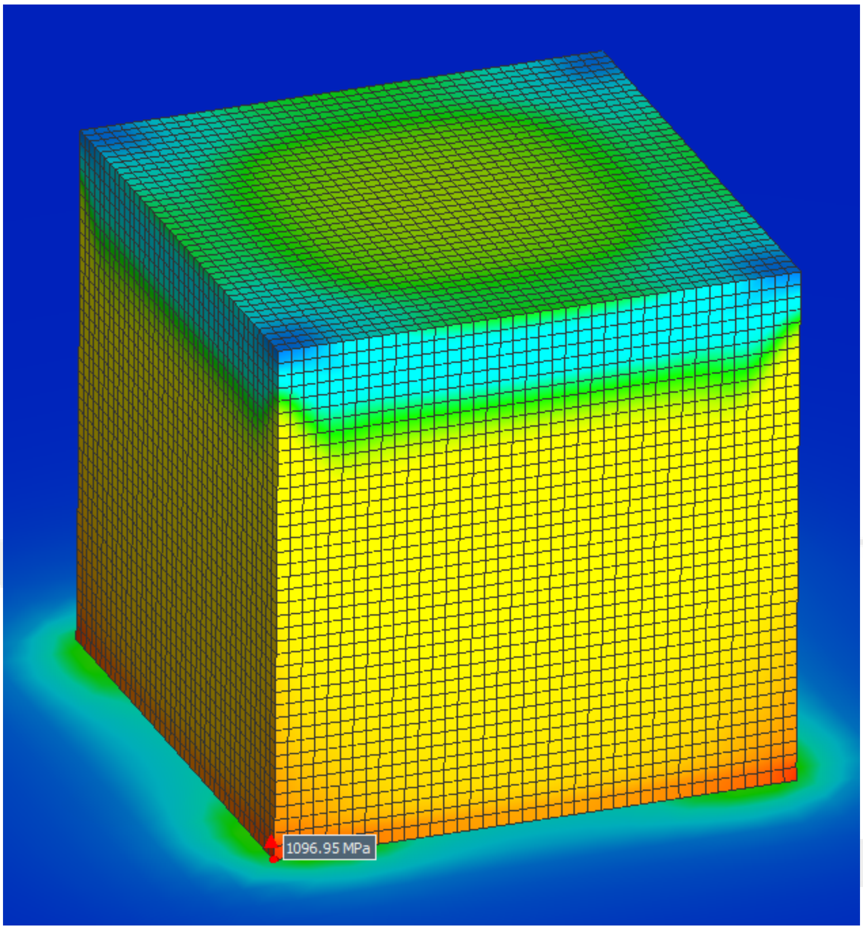

Figure 25: Mesh Convergence Analysis

Results are given below;

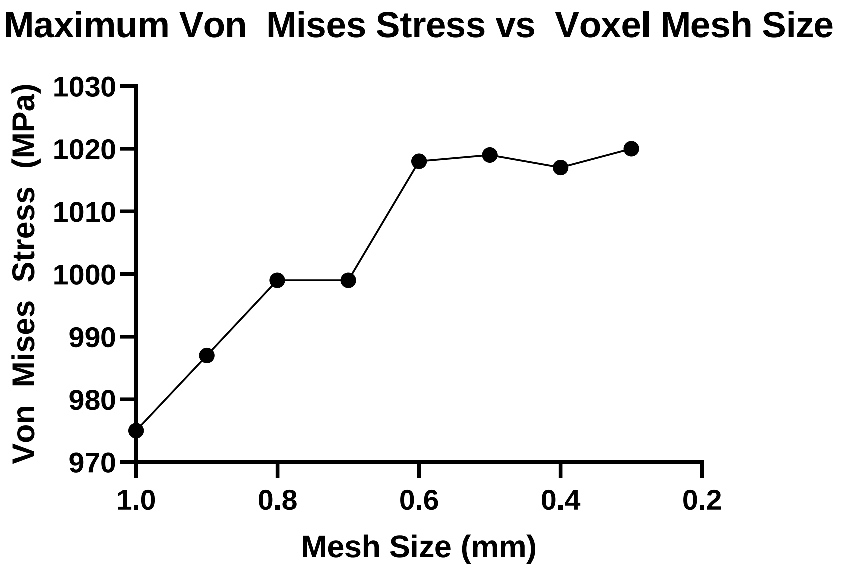

Figure 26: Maximum Calculated Von Mises Stress vs Voxel Mesh Size

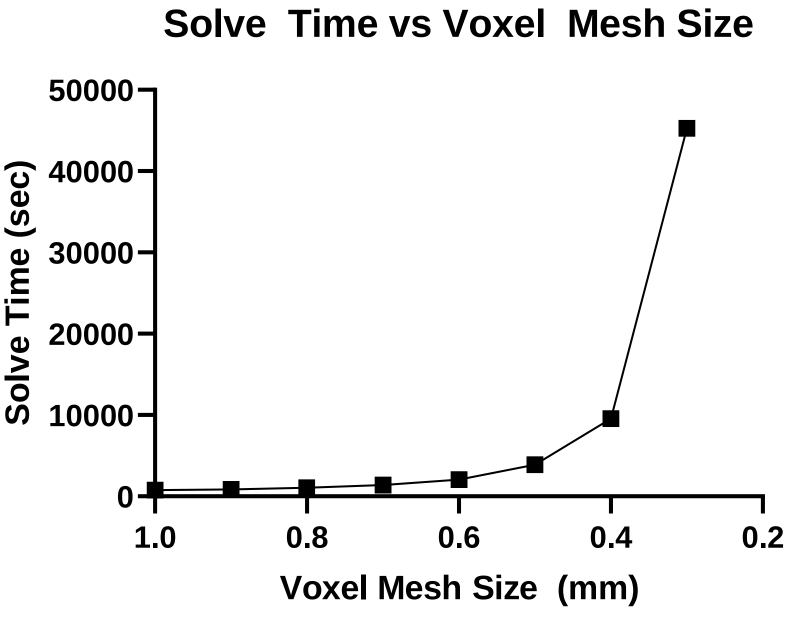

Figure 27: Solve Time for Simulation vs Voxel Mesh Size

Considering the simulation results, decreasing the voxel mesh size below 0.5 mm does not significantly effect the Von Mises Stress values, however solve time increses dramatically. Therefore 0.5 mm is selected as optimum mesh size for the following analysis

3.5.4.2 Assumptions and Simplifications

For Simufact Additive software, there are some simplifications for calculations;

- Liquid convection is not considered
- In order to simplify the calculations, Simufact Additive software neglects the thermal conductions between the part to be printed and the powder and also the powder and baseplate due to the low conductivity of powder. During printing, the heat transfer is only calculated for the very top layer. In the case of deformable base plate selection, predefined heat transfer coefficient and emissivity values of baseplate are made use of during calculations. Representation of heat transfer calculation is given below figure;

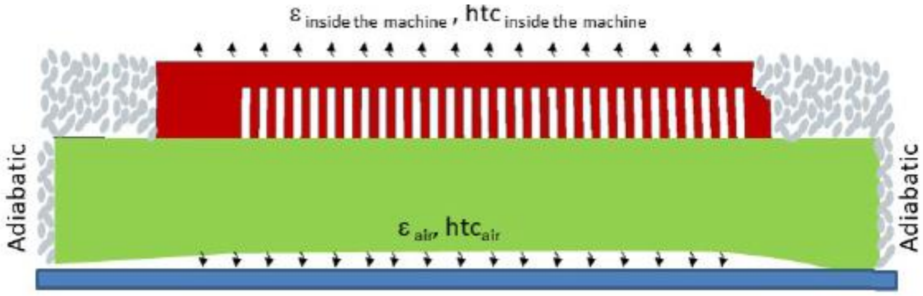

Figure 28: Representation of Simufact Additive heat transfer calculations

For the post-building or heat treatment stage, the predefined heat transfer coefficients are applied to all open surfaces since the powder is removed at these stages. Here, different emissivities and heat transfer coefficients of the baseplate and the part are used.

3.6 Dilatometric Study

In order to obtain thermal expansion behaviour as material input, dilatometric tests was carried out between 1038 °C and -140 °C. First 3 different dilatometry specimens cut from as built SLM'ed and wrought 17-4 PH rods at X-Y-Z directions. First each specimen heated from room temperature to austenitisation temparature at a rate of 1 °C /sec. Specimens were hold for 30 minutes at austenitisation temperature which is 1038 °C. Than cooled at a rate of 7 °C /sec until subzero temperature which is -140 °C to make sure that no retained austenite remains. Thermal dilatation data is recorded over the temperatuıre range. Tests were carried out under %99.9 purified argon atmosphere. Heating and cooling cycles were controlled by induction coil as well as thermocouples. Subzero quenching is also controlled by liquid nitrogen.

Tests were carried out in BAEHR Deformation Dilatometer setup in Atılım University Metal Forming Center of Excellence.

Detailed information about dilatometry test is given in Appendix A

3.7 Manufacturing for Validation of Distortion

In order to evaluate distotion of SLM'ed and SLM'ed & heat treated parts, a proper specimen geometry and a manufacturing setup is needed. To be more realistic, impeller geometry is chosen since impeller requires high geometrical accuracy depending on the application. Therefore 6 identical impellers are manufactured with same optimised process parameters (Section 3.2) on the same baseplate as shown in below figure.

Figure 29: Manufactured impellers for distortion measurement

In order to examine the as built and heat treated part distortions, experimental setup is as follows;

- Impeller 1,2,3 and 4 is cut from baseplate with EDM. Any post-heat treatment is applied without baseplate.
    - Impeller 1: Remains as-built. No post heat treatment
    - Impeller 2: Stress relief heat treatment
    - Impeller 3: Solutionizing & ageing
    - Impeller 4: Stress relief heat treatment, solutionizing & ageing
- Impeller 5 and 6 is stress relieved on baseplate.
    - Impeller 5: Stress relief heat treatment & EDM cut from baseplate

- Impeller 6: Stress relief heat treatment, EDM cut from baseplate followed by solutionizing and ageing heat treatment

At first step, surface profile of the impellers are recorded with CMM device without cutting from baseplate as shown below figure.

Figure 30: CMM dimensional measurement of impellers

3.8 Manufacturing for Validation of Residual Stress

In order to validate simulation results for residual stress, 6 different crosses are built as shown below figure;

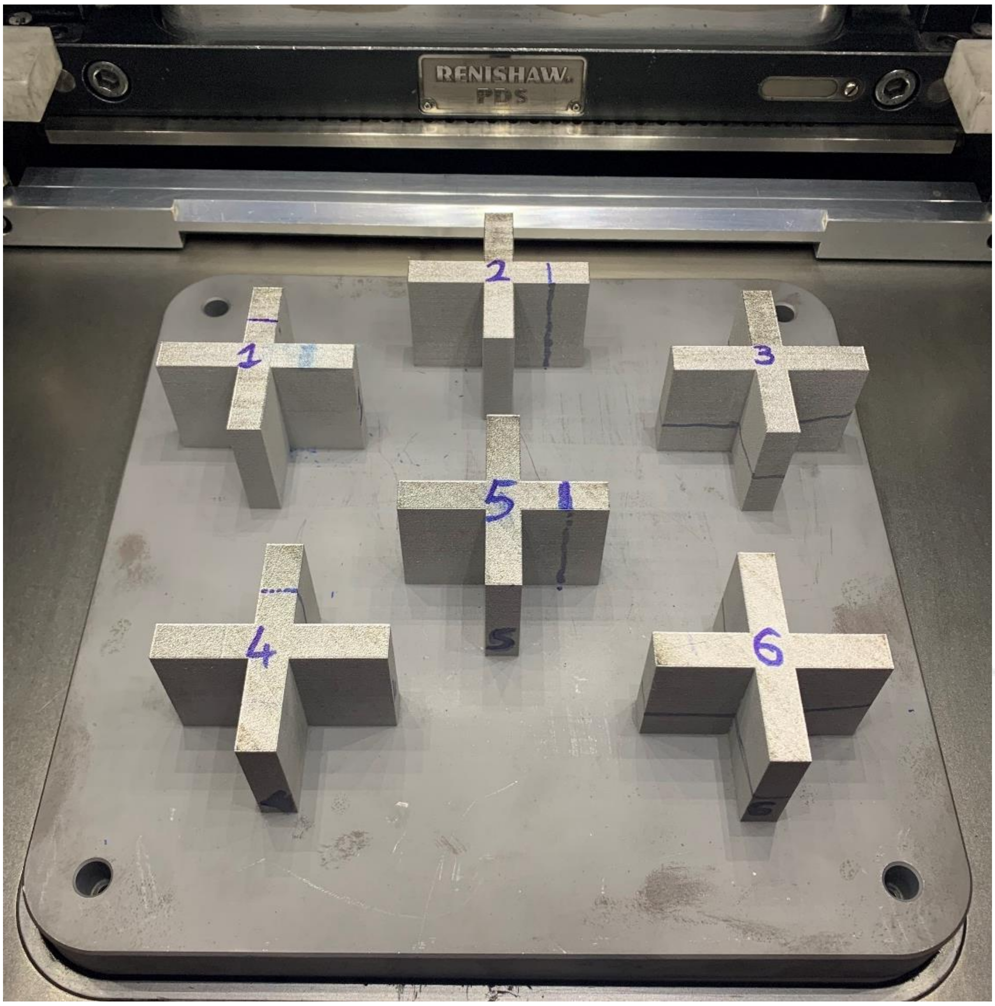

Figure 31: SLM'ed cross parts for the experimental validation of residual stress

All crosses are manufactured with same optimised 17-4 PH process parameters with meander scan pattern (Section 3.2). Only difference is rotation between layers. There are 2 groups of crosses;

- Group 1 consisting of Crosses 1,2,3 are manufactured with optimised 17-4 PH parameters except for 0 degree rotation between layers. Scan vectors lie along X axis for whole build. An illustration of scan pattern for Group 1 is as follows;

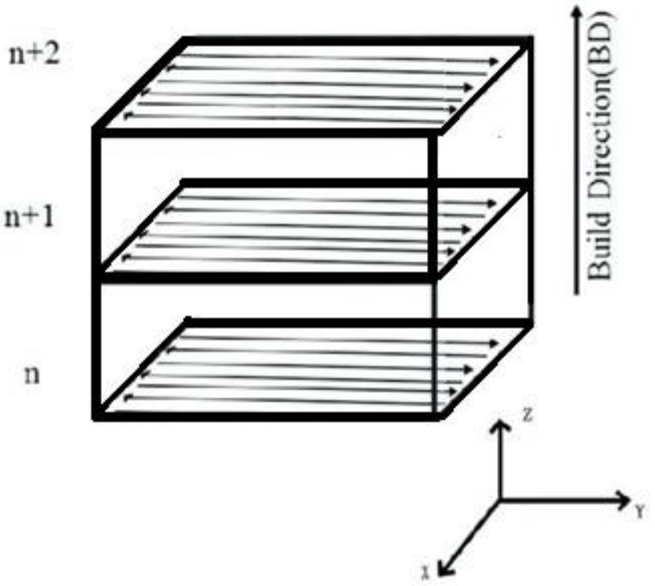

Figure 32: Crosses Group 1 scan pattern

- Group 2 consisting of Crosses 4,5,6 are manufactured with optimised 17-4 PH parameters. An illustration of scan pattern for Group 2 is as follows;

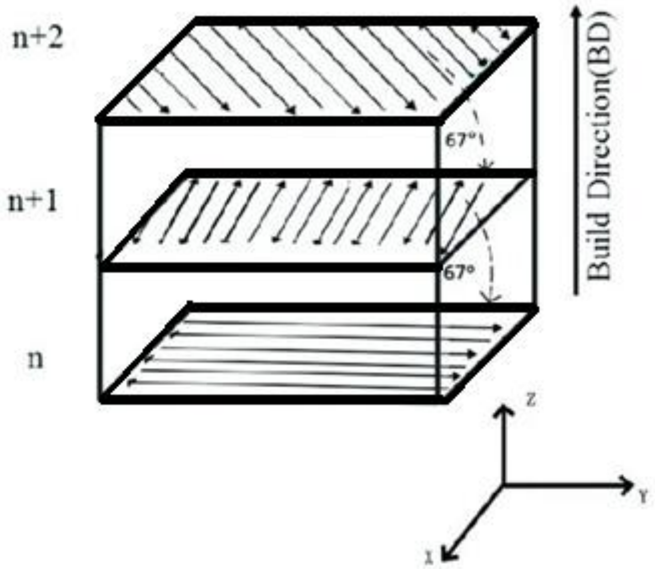

Figure 33: Crosses Group 2 scan pattern

All crosses are cut from baseplate by EDM and further EDM cutting is carried out at the mid section of dashed lines as X-Y-Z cut.

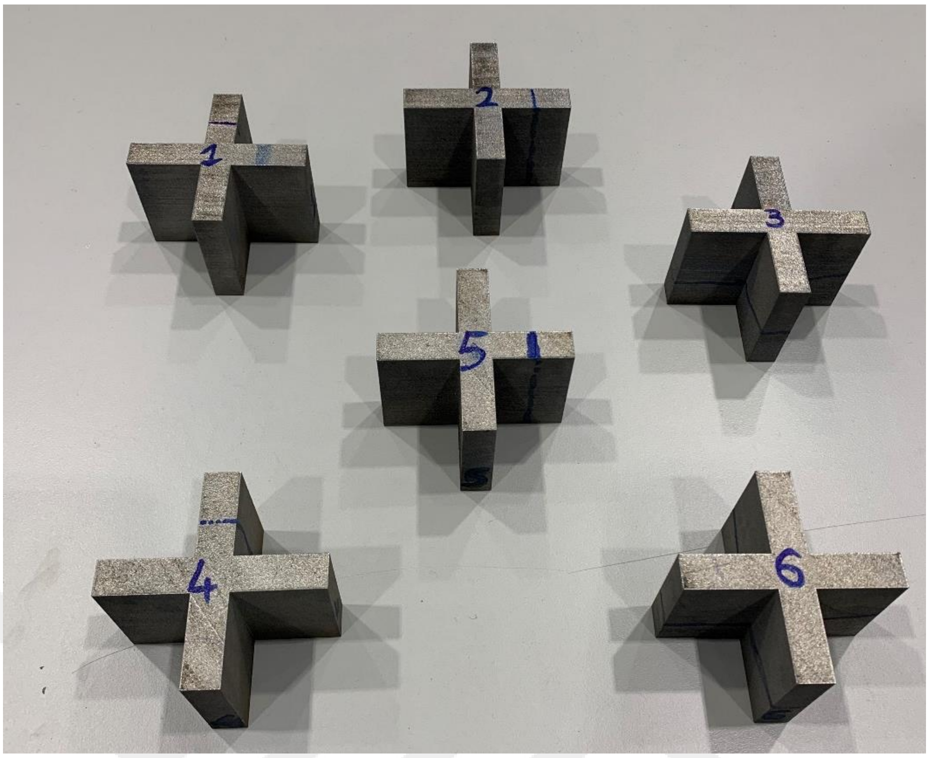

Figure 34: Crosses after cut from baseplate

3.9 Contour Residual Stress Measurement

3.9.1 Measurement of Surface Deformations with CMM

Measurements of surface deviations are carried out with Hexagon Tigo SF CMM device with a working capacity of 500 x 580 x 500 mm (X/Y/Z). Renishaw star probe is used for the measurements.

Figure 35: Measurement of Surface Deformations

3.9.2 pyCM Software

Python Contour Method (pyCM) is a Python based open source software developed by M.J. Roy at University of Manchester in order to ease and standardise the experimental contour residual stress measurement technique. pyCM consists of a GUI framework for the purpose of processing and making the experimentally measured raw data ready for the further FE analysis. The workflow of pyCM consists of following steps:

1. Registration of both sides of CMM measured raw cut surface data:

One of the measured surface profile is registered as reference while the opposite surface as floating. Measured surface profiles are registered in 2 step; outline data and surface data. File is imported as .txt. Outlier data for both reference and floating surfaces are eliminated at the registration step. Outline and surface data are both moved to mean Z therefore difference between mean z values are eliminated. Origin coming from CMM data is changed into geometric centroid by moving to the centroid. By applying Single Value Decomposition, skewed normal of the point surface is aligned along Z axis.

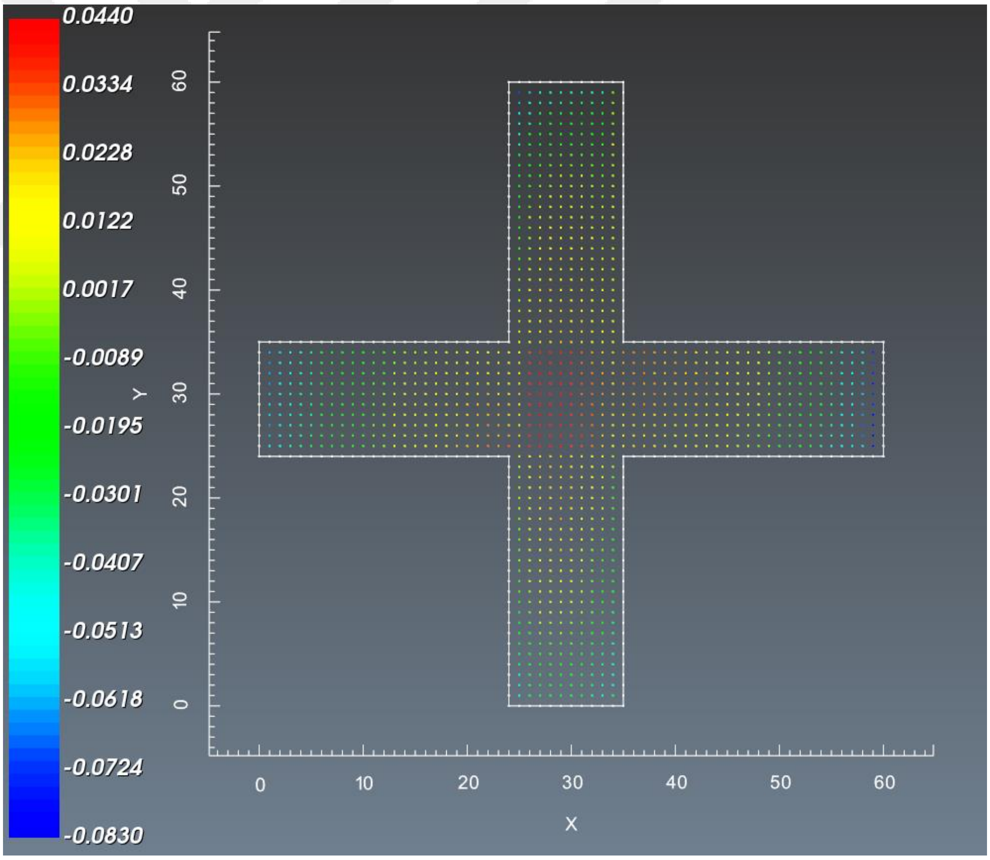

Figure 36: Registration of Reference surface- Top view

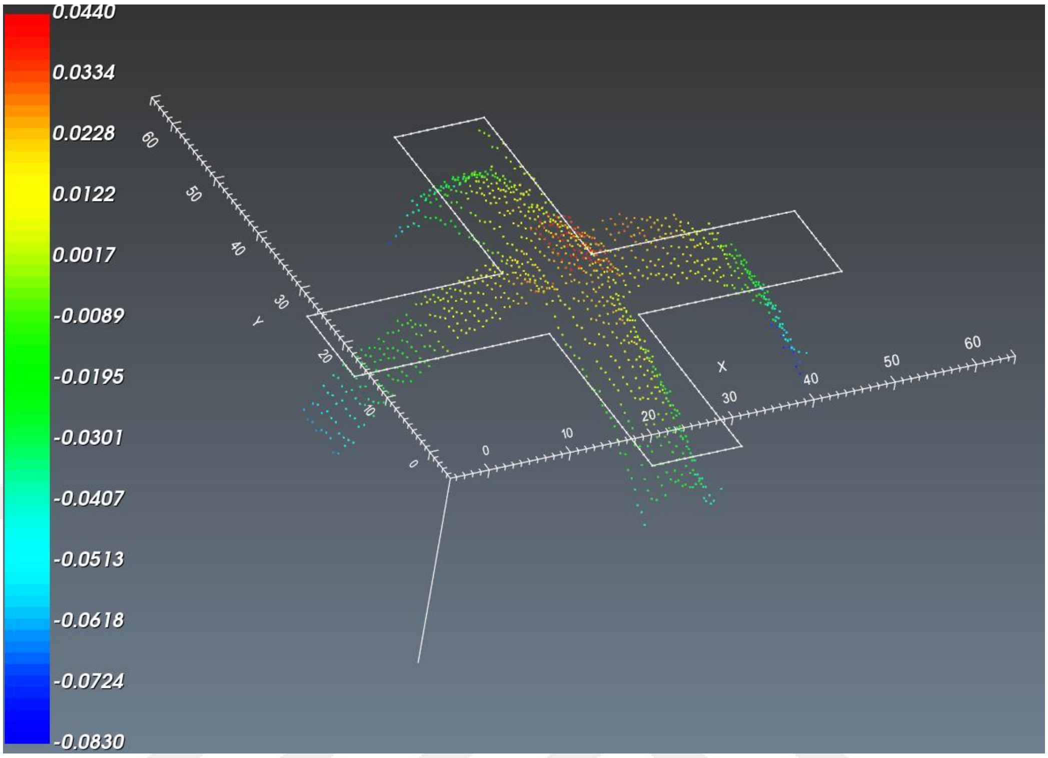

Figure 37: Registration of Reference Surface- Side view (250x scale)

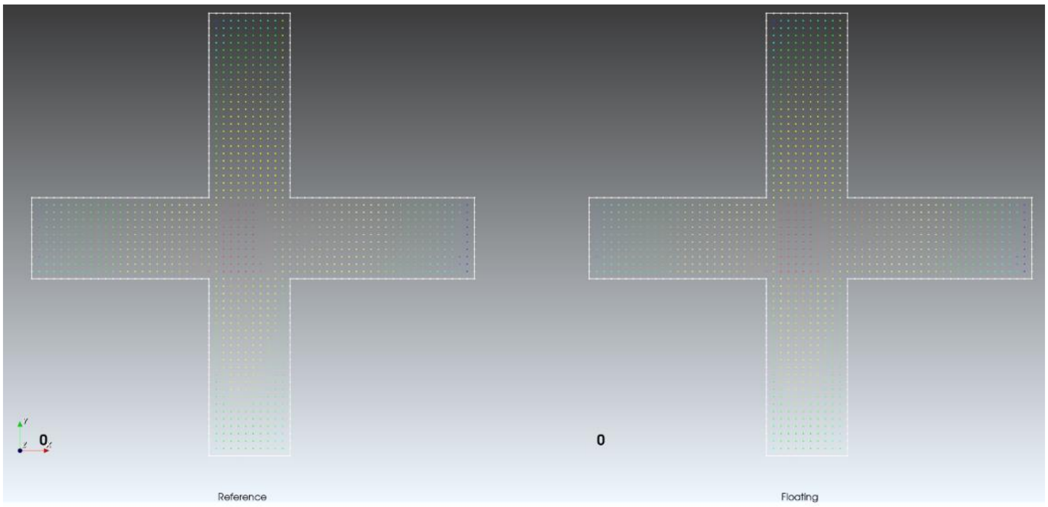

Figure 38: Preview of registered Reference and Floating surfaces

2. Alignment and averaging of both surface profiles:

   In order to eliminate cutting error, both reference and floating data defined in previous step are averaged into a common grid. By using Automated Iterative Closest Point algorithm, differences in outlines are prevented. Both reference and floating surfaces moved to their centroids automatically. Alignment of surface and outline data are done with K-neighbour Iterative Closest Point (ICP) algorithm which minimizes the error between surface and outline data. On a common x,y grid of both reference and floating surfaces, linear interpolation is applied for z values. Grid spacing value is set automatically which is calculated according to the density of data. After alignment is completed, both reference and floating surfaces are averaged into one surface.

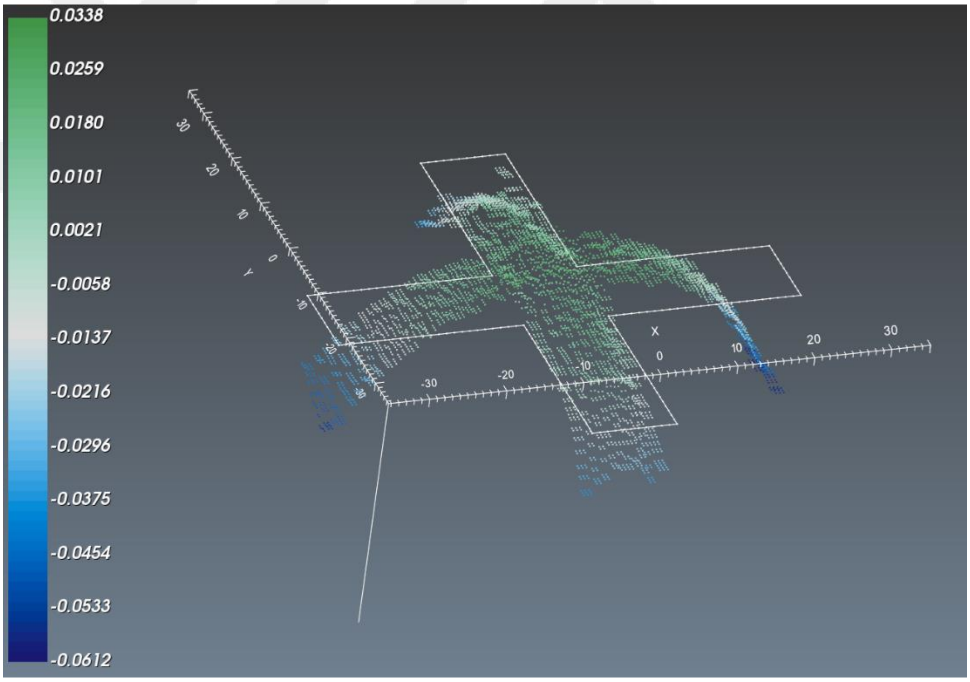

Figure 39: Averaging and gridding of Reference and Floating surfaces

3. Numerical fitting of averaged surface profile

   Averaged data is numerically fit in order to smooth and further use as displacement boundary condition for FE analysis. A bivariate fit as discrete polynomial functions at the order of 3 is applied where the spline spacing is calculated automatically.

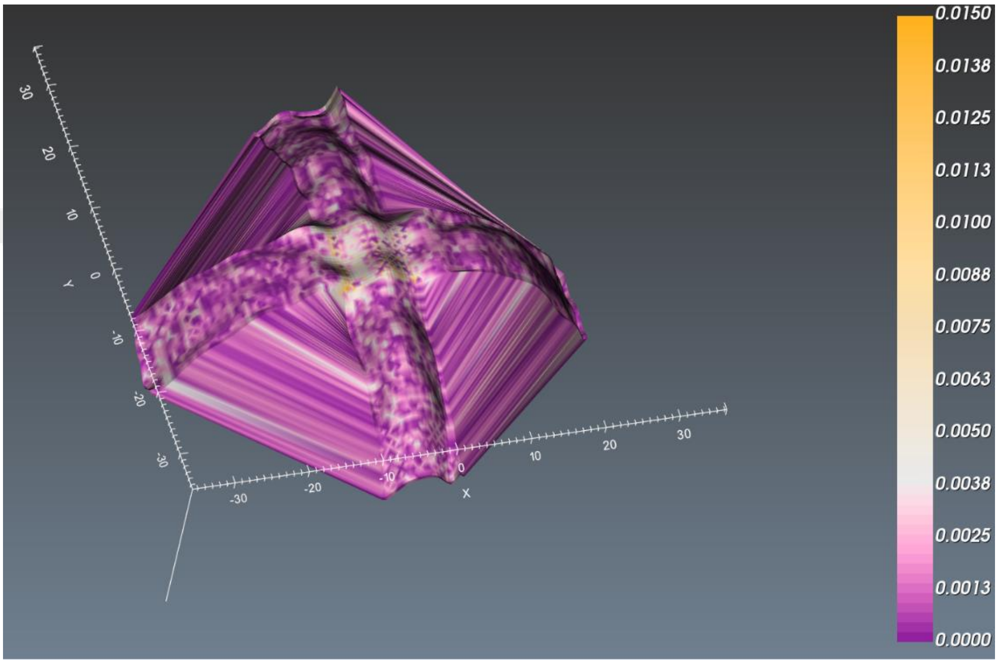

Figure 40: Numerical Fitting of averaged surface

4. FEA preprocessing

   In order to run linear elastic FE analysis, numerically fitted surface profile needed to be meshed, Elastic Modulus and Poisson’s ratio should be defined together with the displacement boundary conditions which is dictated by numerically fitted data. In this study, mesh generation is done by however it can also be done by GMSH v4.1.1.0. In this step, extrude function enables points locating at outline and serving as mesh seeds to be extruded along Z direction. Node count, Extrusion Length and Minimum element length are defined as respectively. Mesh structure is consists of 8 noded linear quadrilateral elements, or 10 noded second order tetrahedra. Boundary conditions are defined on 2 neighbour corners. The node on the left corner is fixed along X-Y direction while the node on the right corner is fixed along only Y direction. Elastic modulus and Poisson's Ratio are defined as E=200 GPa and V=0.3. Then Project is saved as .inp format which can be opened by ABAQUS or other solvers. Calculix v3.5 software is used for solving the generated .inp file.

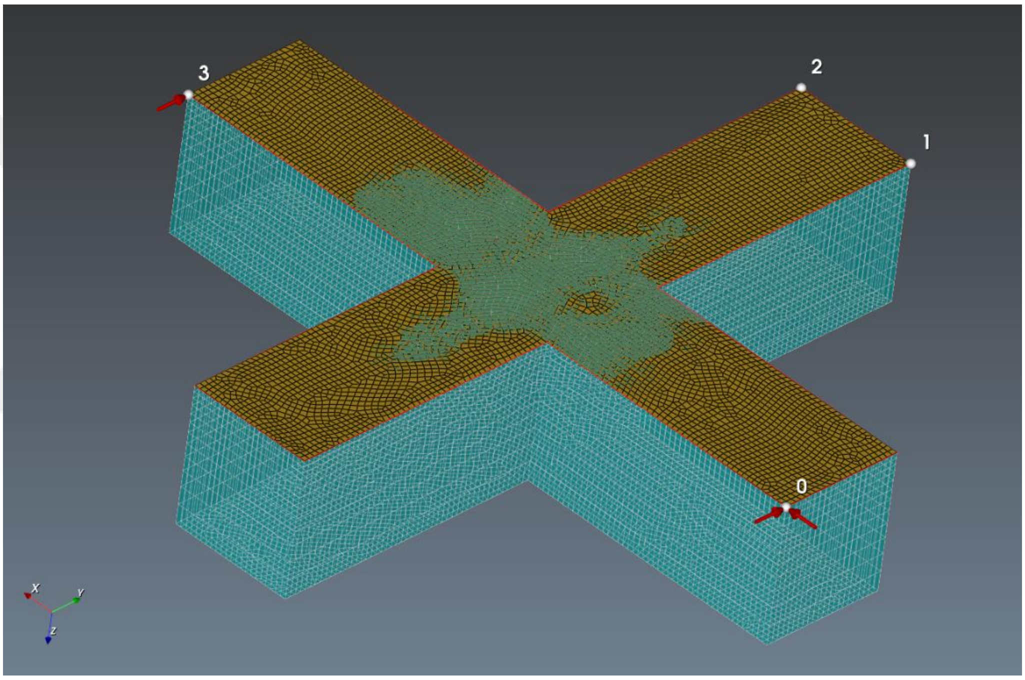

Figure 41: Extruding & meshing of the geometry and specification of numerically fitted surface deformations as well as boundary conditions to prevent rigid body motion and rotation

5. Post processing and interpretation

Obtained results are discussed in Results&Discussion section.

CHAPTER 4

RESULTS AND DISCUSSION

4.1 Validation of Simulation

From the optical microscopy image the melt pool width is validated with the simulation. The observed melt pool has 90 micrometer width and point distance is close to 110 micrometer [34]. Optical microscopy image is given below;

Figure 42: Optical microscopy of as built 17-4 PH SS in the build direction

Validation of simulation results is done by comparing the optical microscope image of solidified melt pool size. The specimen to be observed is SLM'ed with same parameters in with model input values.

Image of EDS line analysis and results are given below figure. No significant segregation is observed across point distance which is 110 µm.

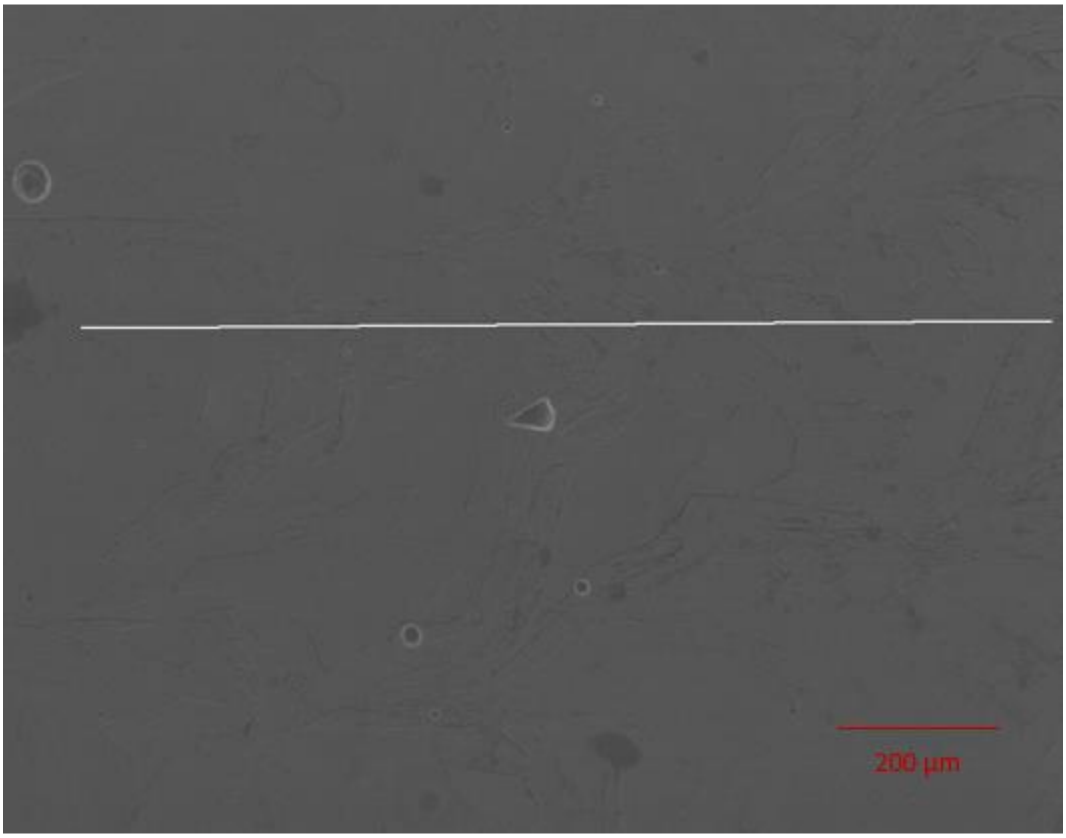

Figure 43: EDS line analysis

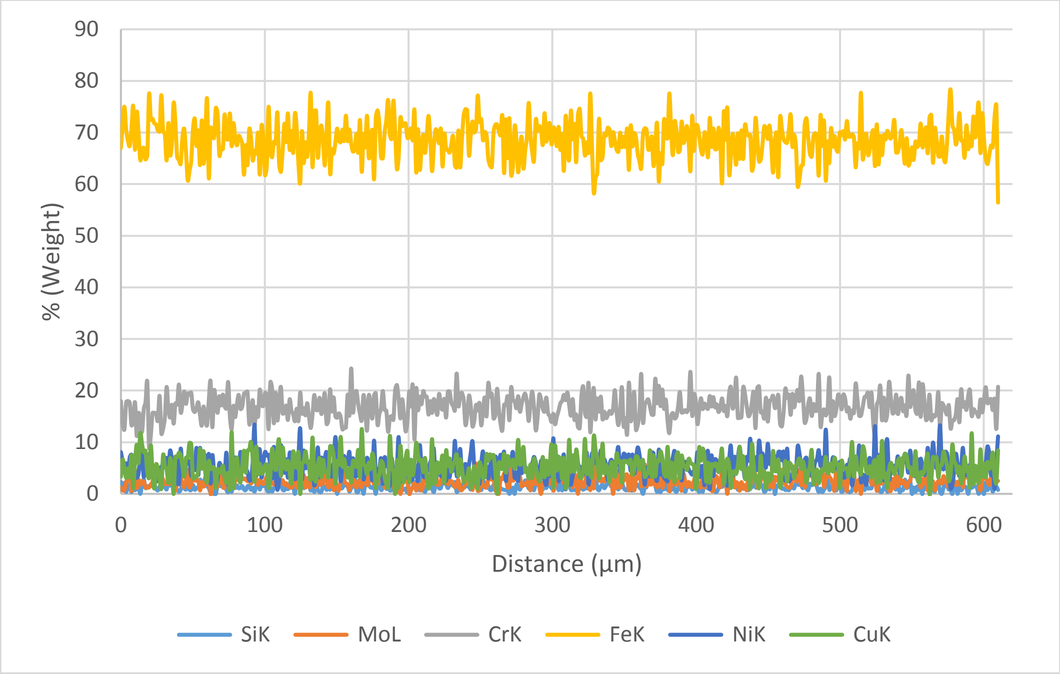

Figure 44: EDS line analysis results

4.2 Mesoscale Model

In mesoscale model which consists of total 5 layers, observed peak tempearature of the melt pool is 2140 °C, as being consistent with literature.

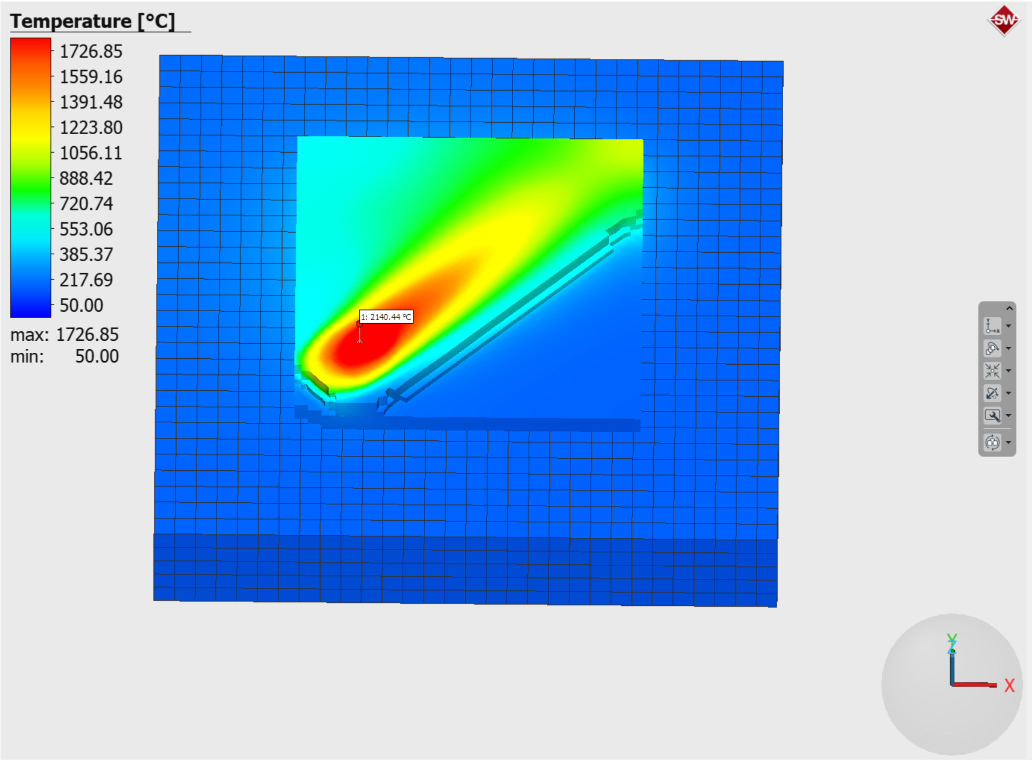

Figure 45: Mesoscale model thermal results

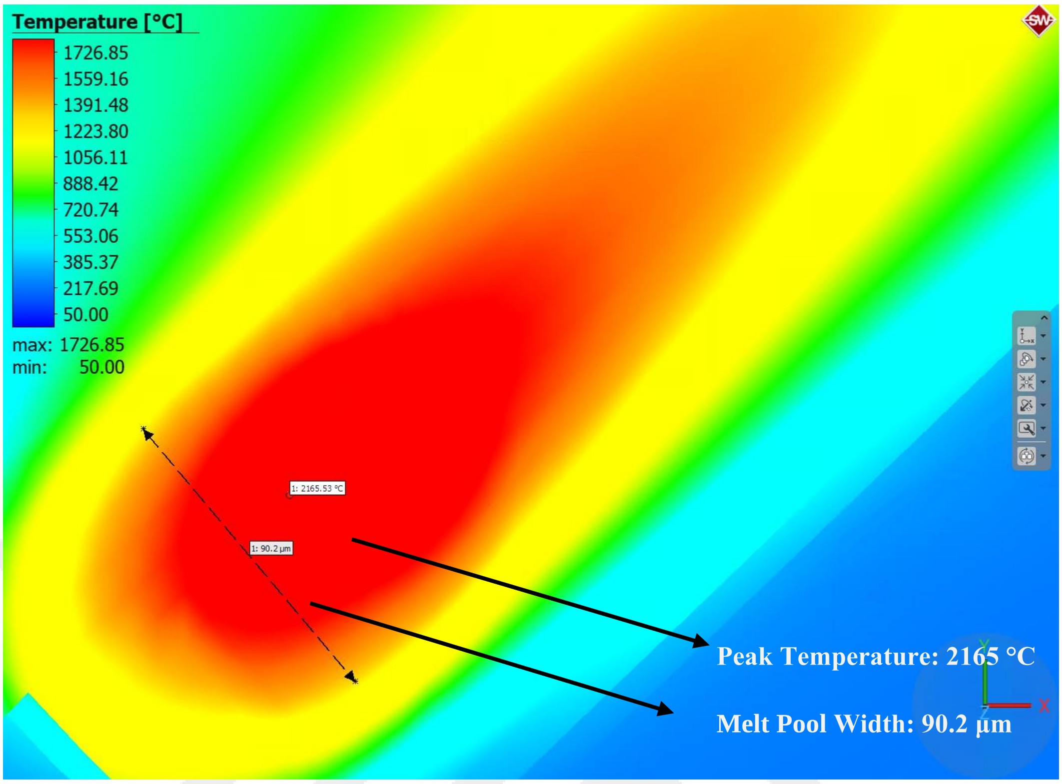

Figure 46: Melt pool in mesoscale model results

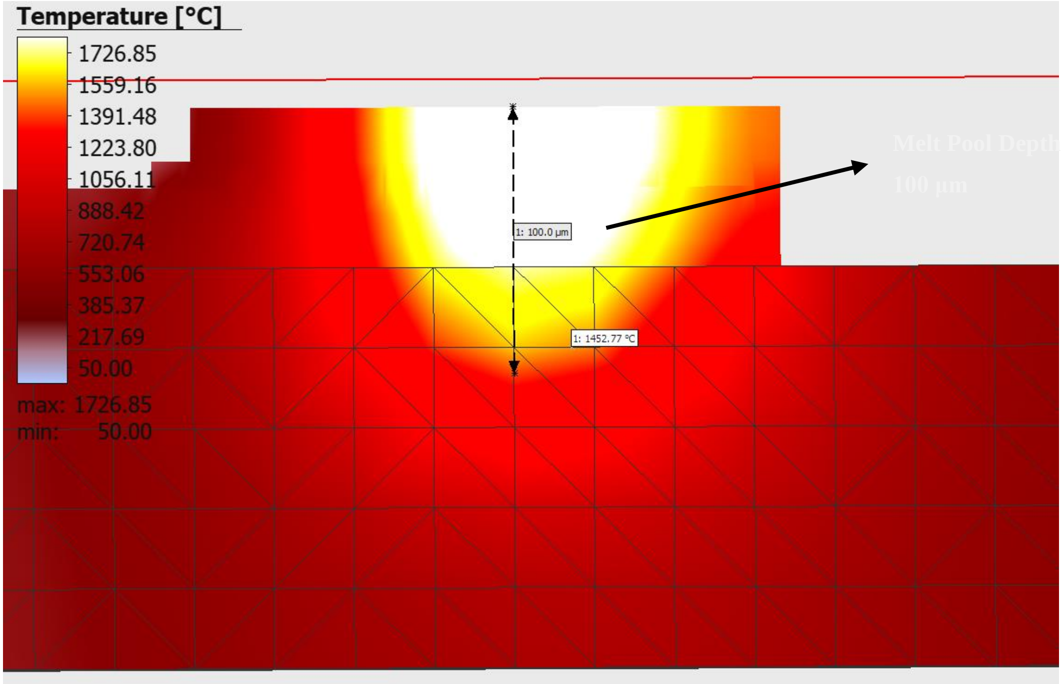

Figure 47: Mesoscale model melt pool depth

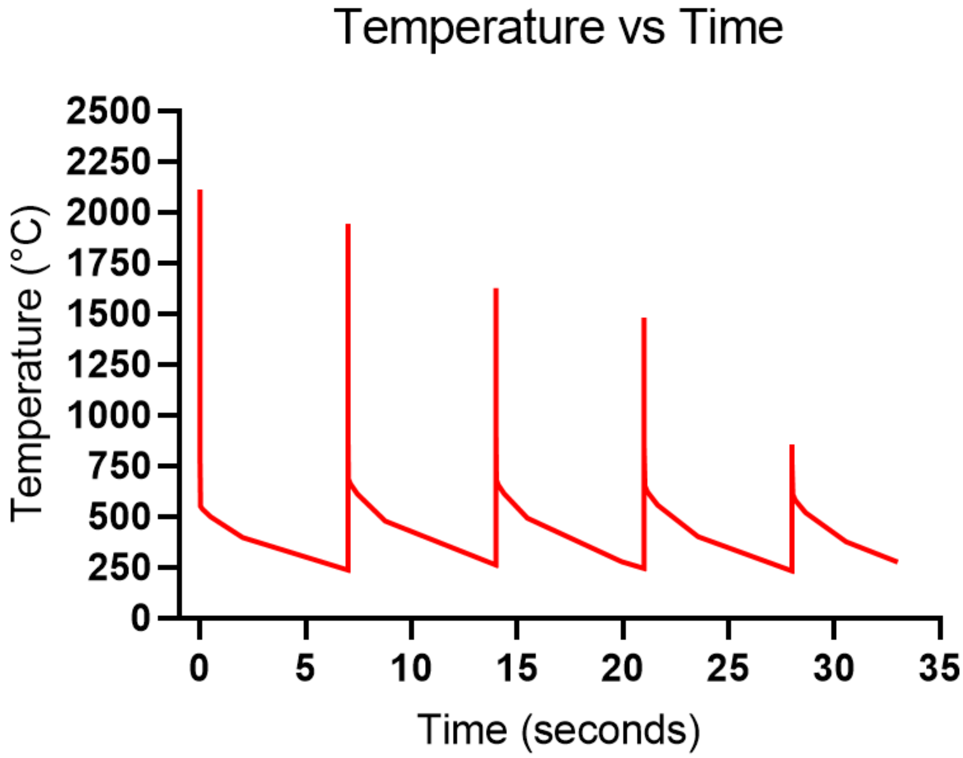

Figure 48: Mesoscale model thermal history of bottom node

Cooling rate from 2100 °C peak temperature is calculated as 211292.6 K/sec which is consistent with the observed SLM cooling rates reported in the literature. For each consecutive recoated layers, peak temperature of selected node decreases 2111 °C, 1941 °C, 1625 °C, 1479 °C and 862 °C which means that together with the very top layer, remelting and solidification occurs for 3 layer beneath it.

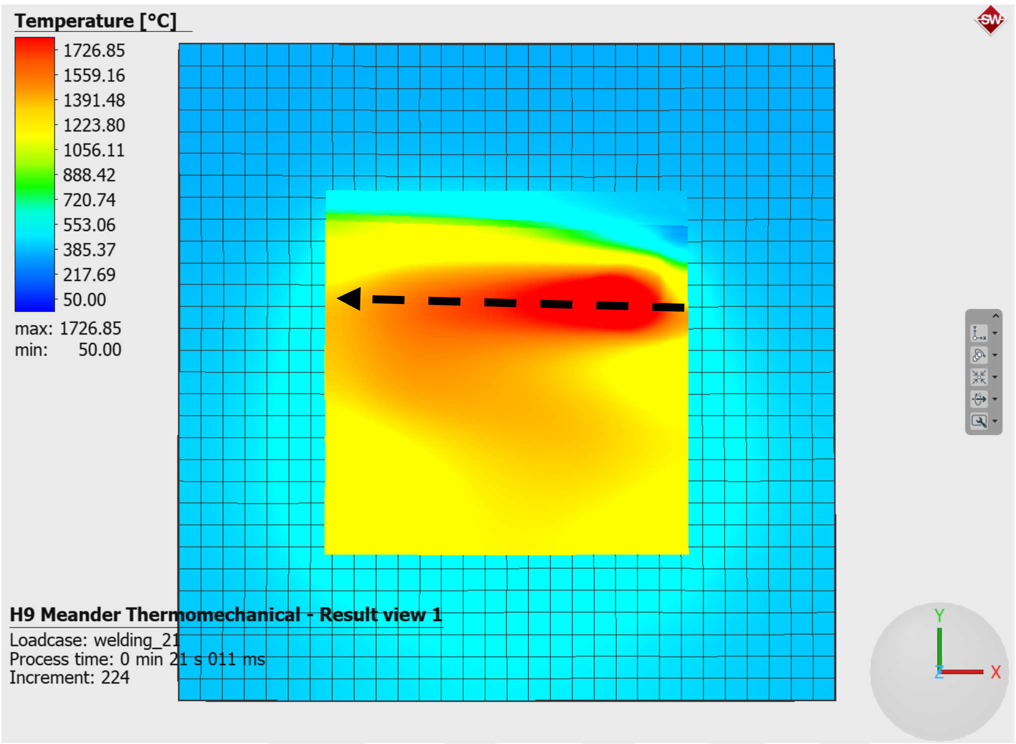

H9 Meander Thermomechanical - Result view 1

Loadcase: welding_21
Process time: 0 min 21 s 011 ms
Increment: 224

Figure 49: Examination along X direction

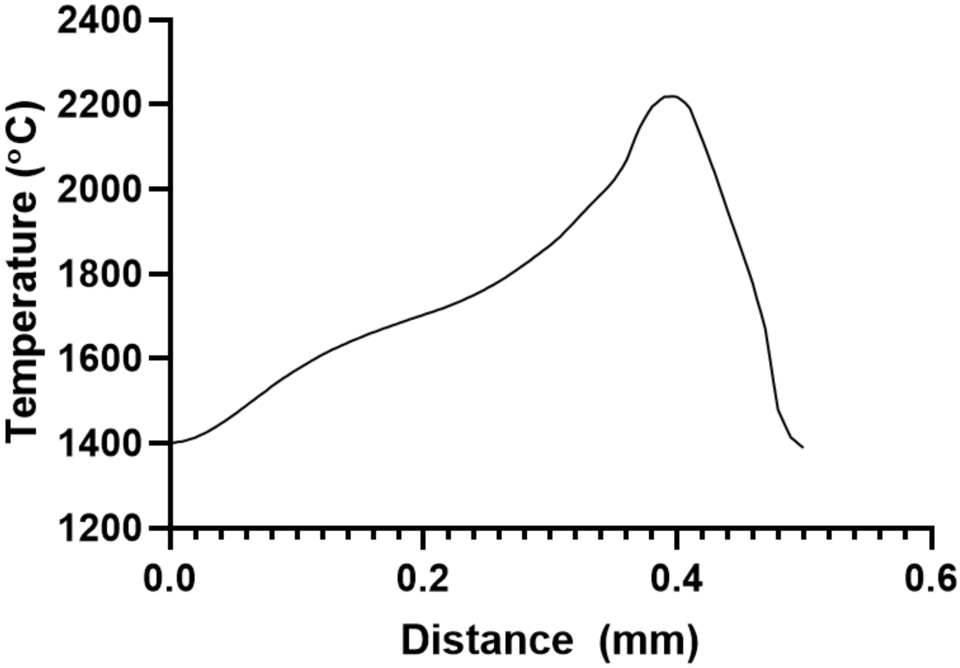

Figure 50: Temperature profile along X direction

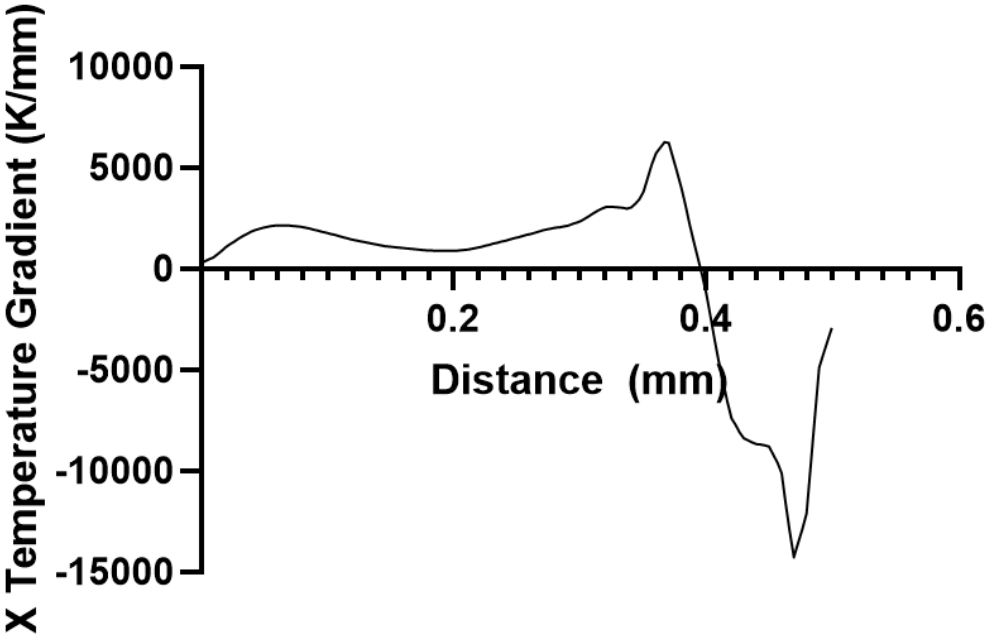

Figure 51: X Temperature gradient along X direction

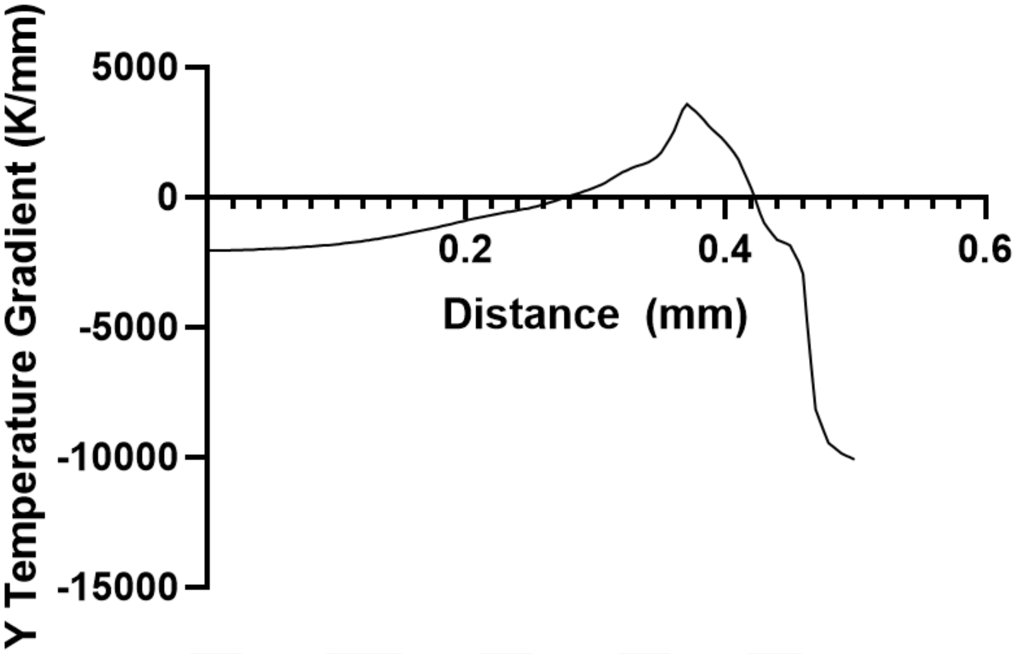

Figure 52: Y Temperature gradient along X direction

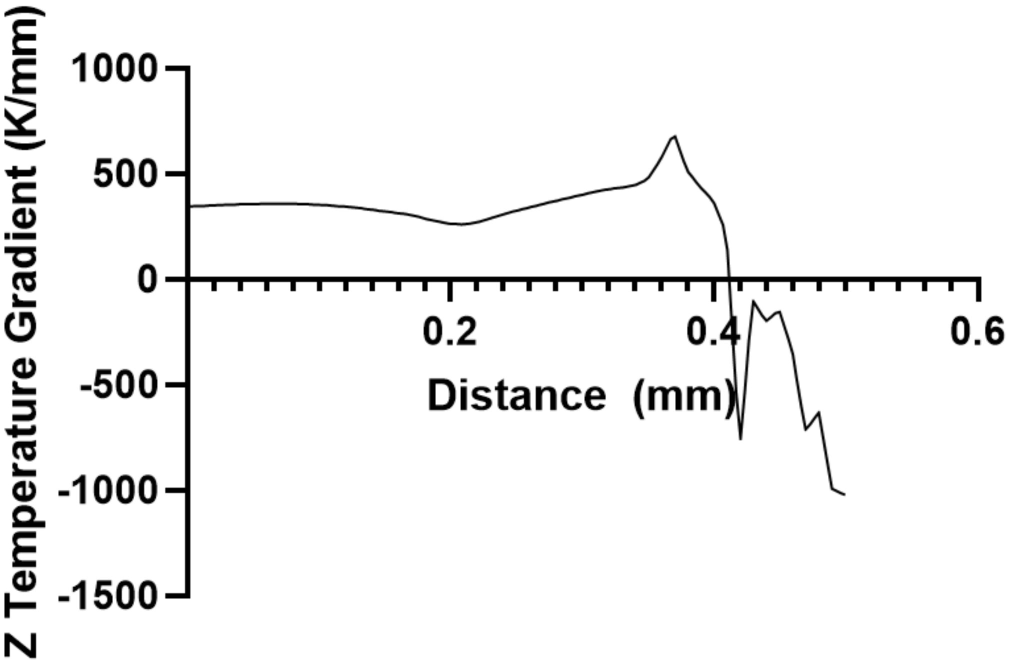

Figure 53: Z Temperature gradient along X direction

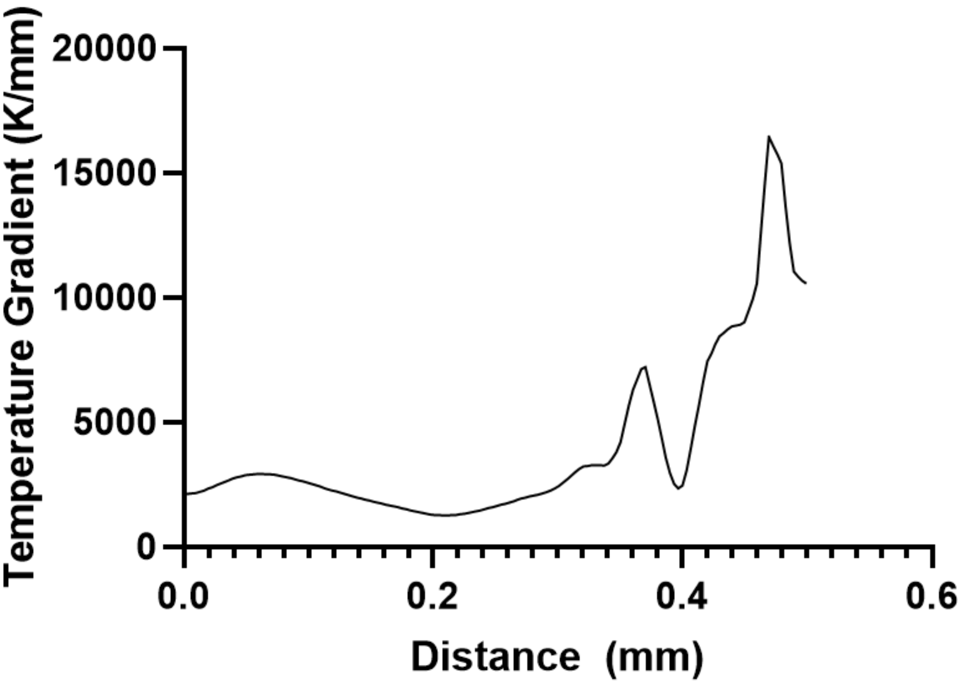

Figure 54: Temperature gradient along X direction

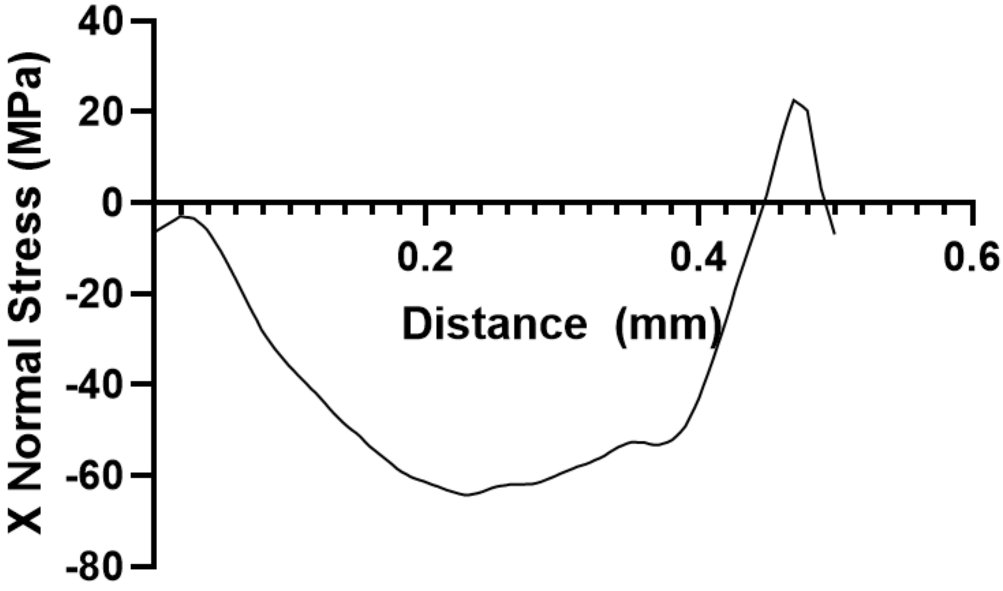

Figure 55: X Normal Stress along X direction

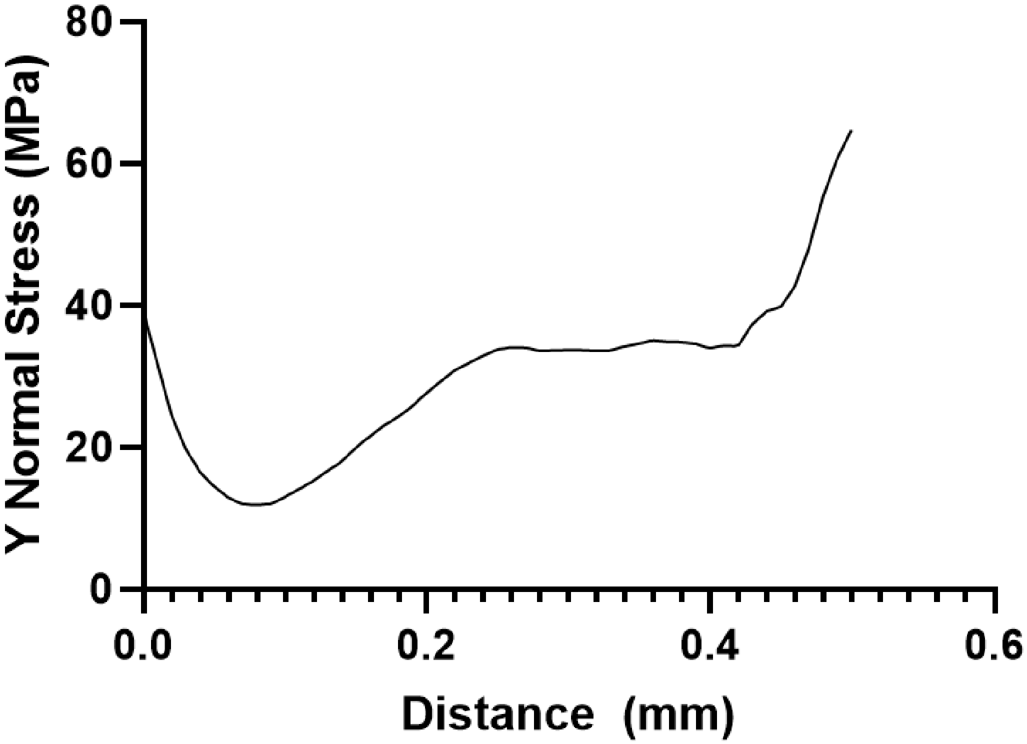

Figure 56: Y Normal stress along X direction

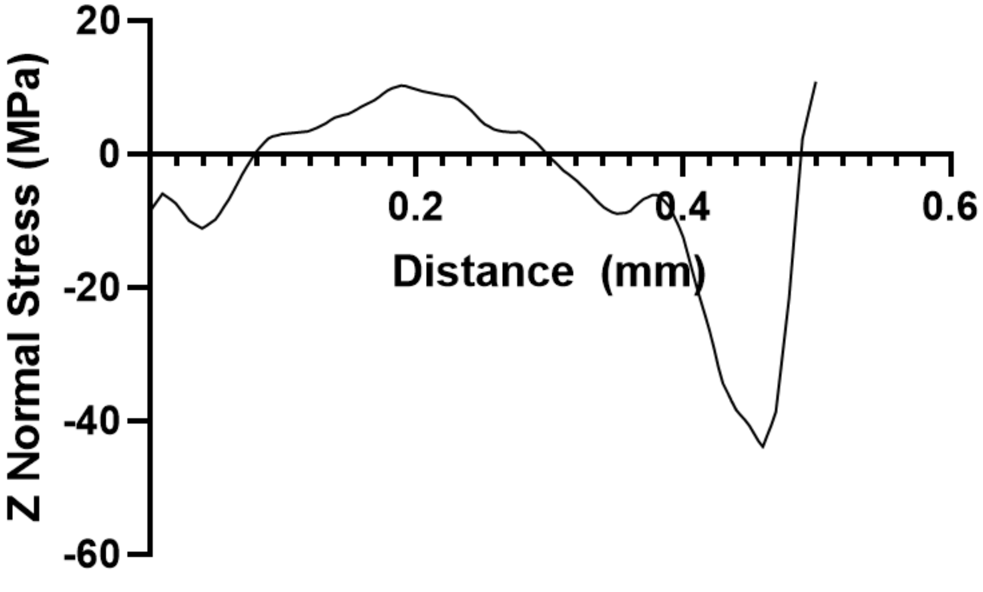

Figure 57: Z Normal Stress along X direction

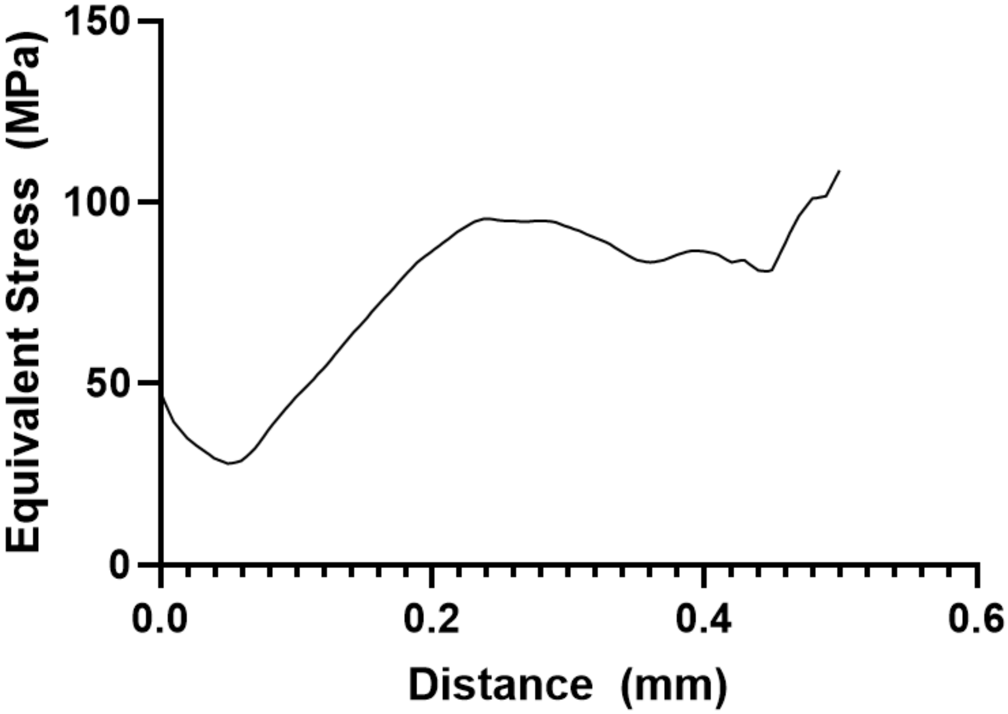

Figure 58: Equivalent Stress along X direction

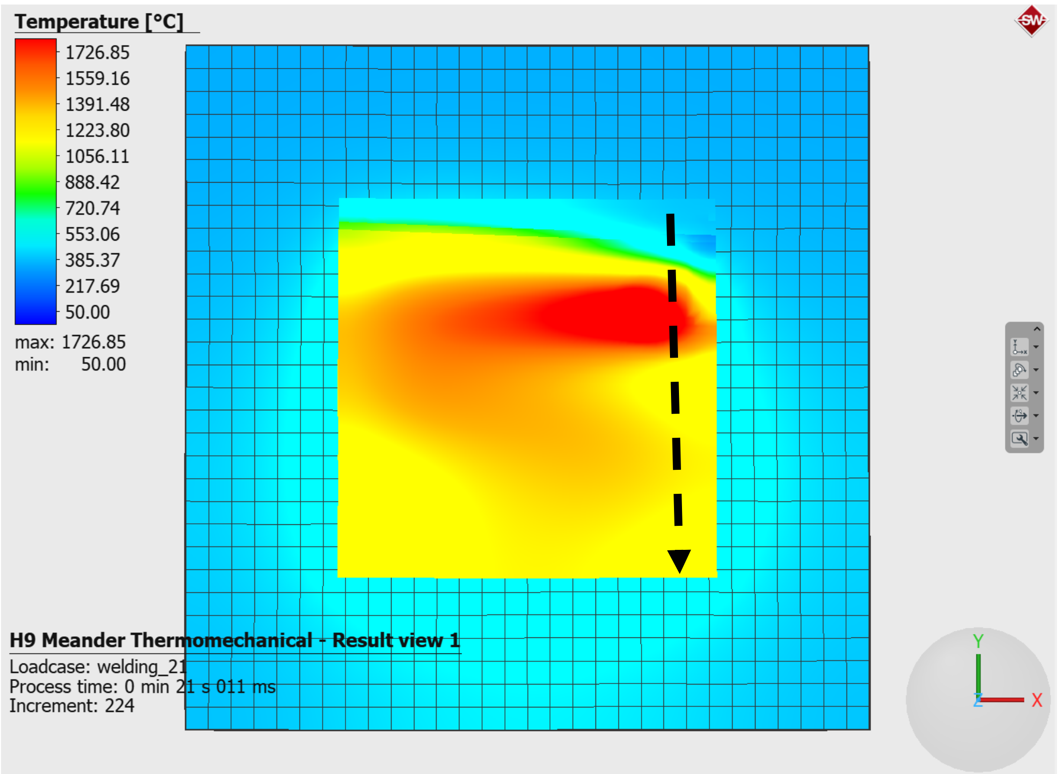

H9 Meander Thermomechanical - Result view 1

Loadcase: welding_21
Process time: 0 min 21 s 011 ms
Increment: 224

Figure 59: Examination along Y direction

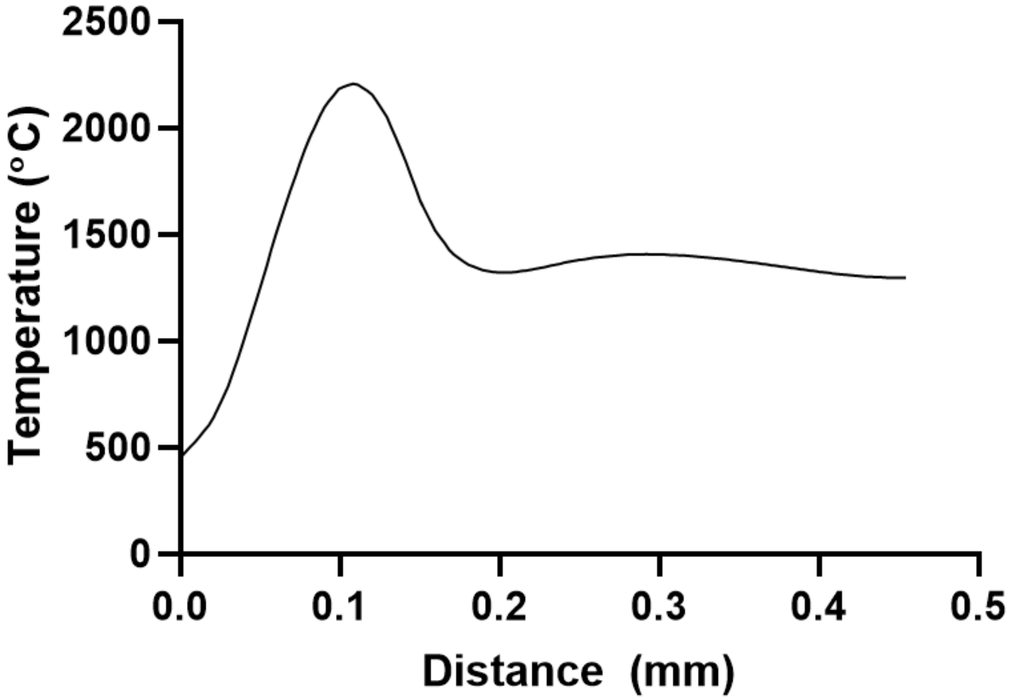

Figure 60: Temperature profile along Y direction

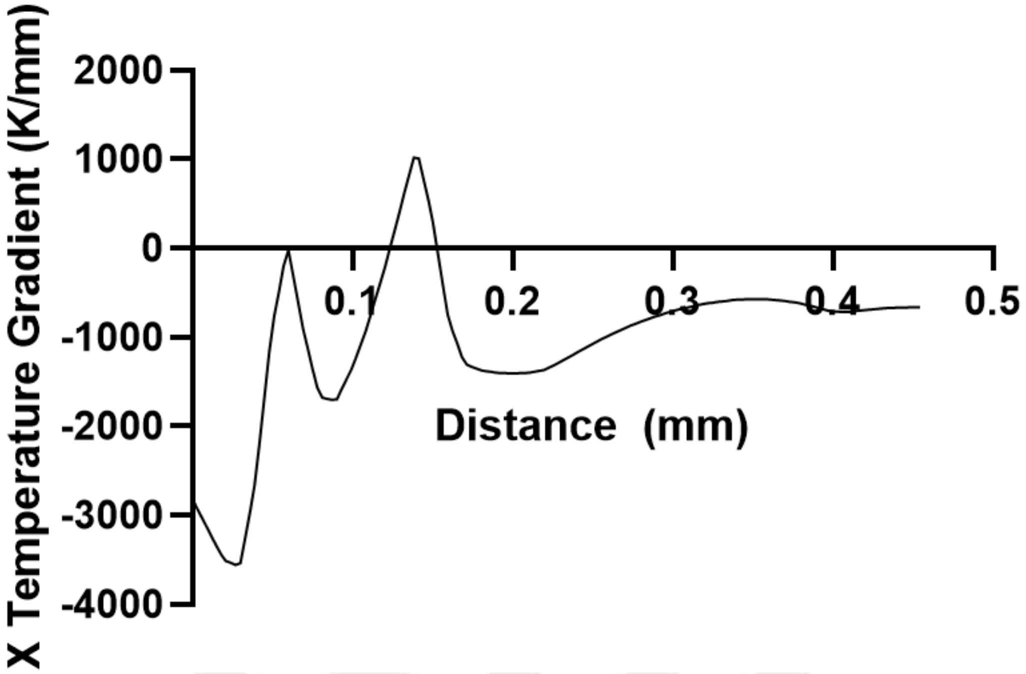

Figure 61: X Temperature gradient along Y direction

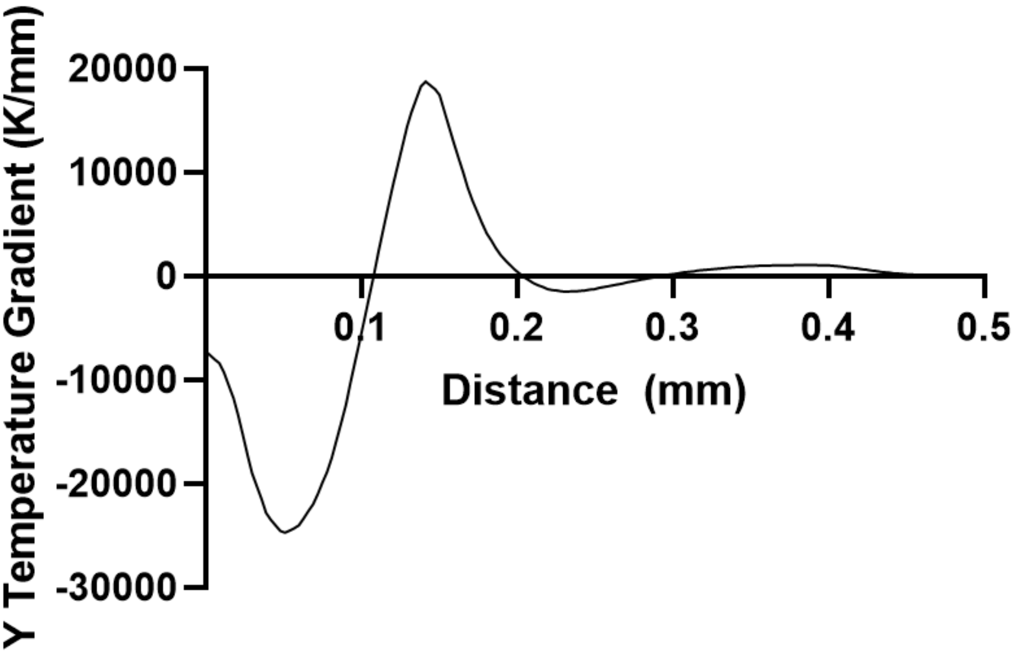

Figure 62: Y Temperature gradient along Y direction

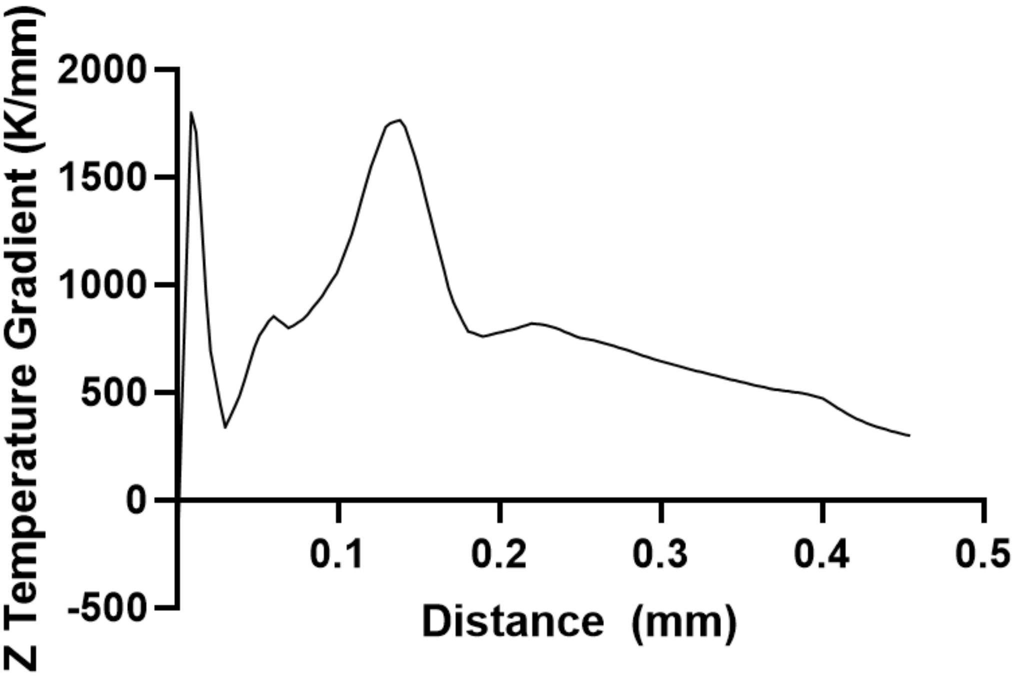

Figure 63: Z Temperature gradient along Y direction

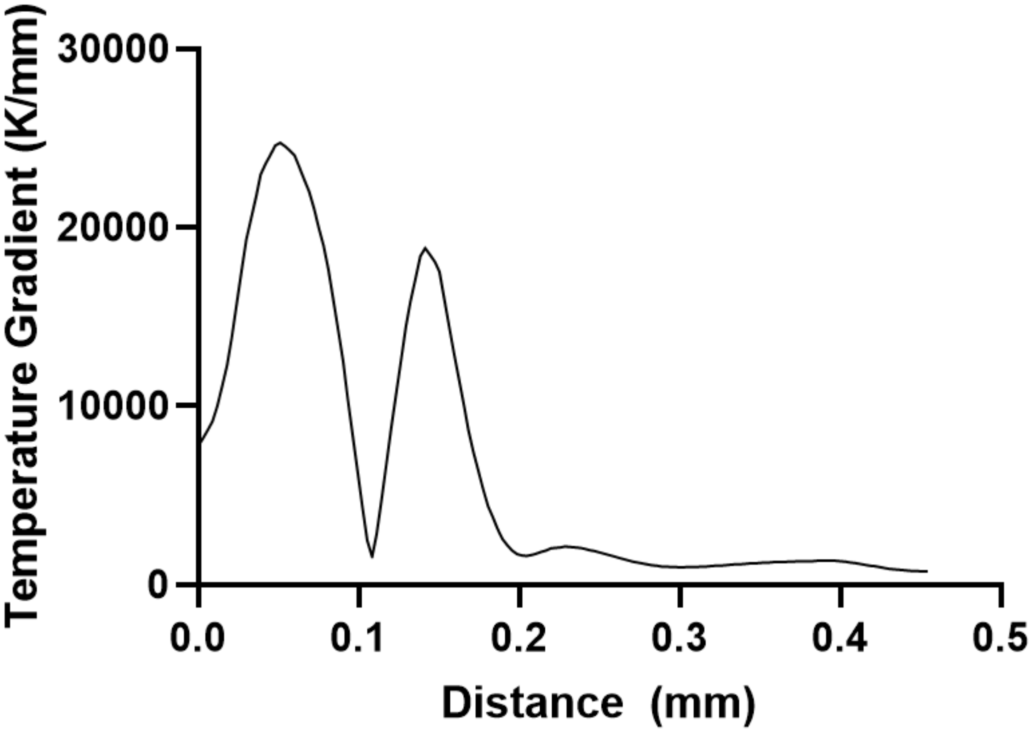

Figure 64: Temperature gradient along Y direction

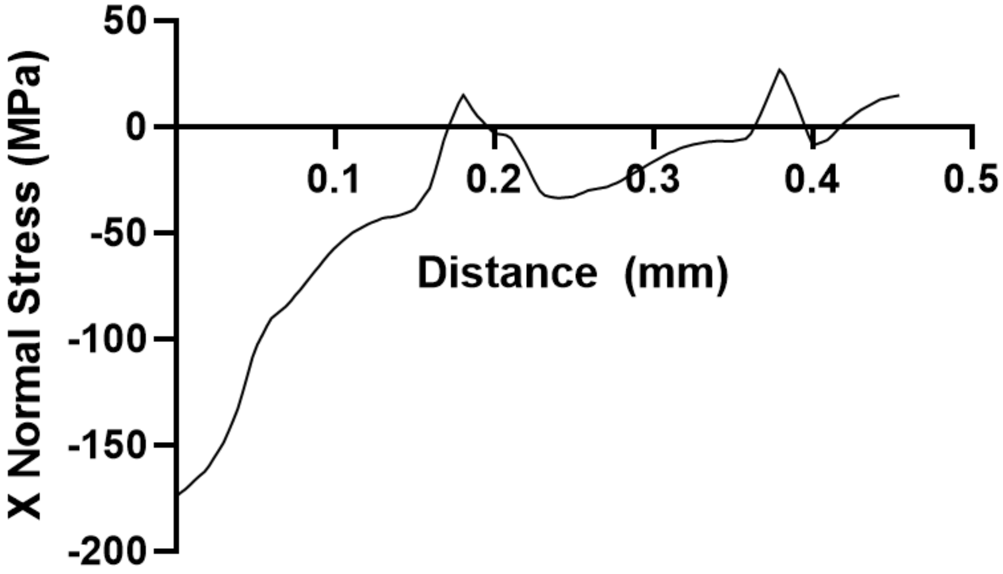

Figure 65: X Normal Stress along Y direction

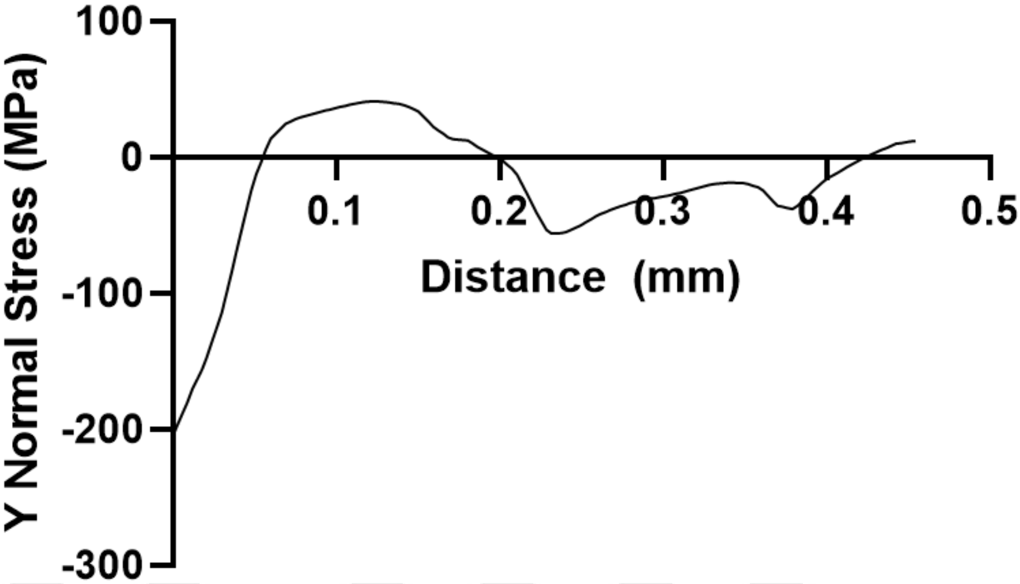

Figure 66: Y Normal Stress along Y direction

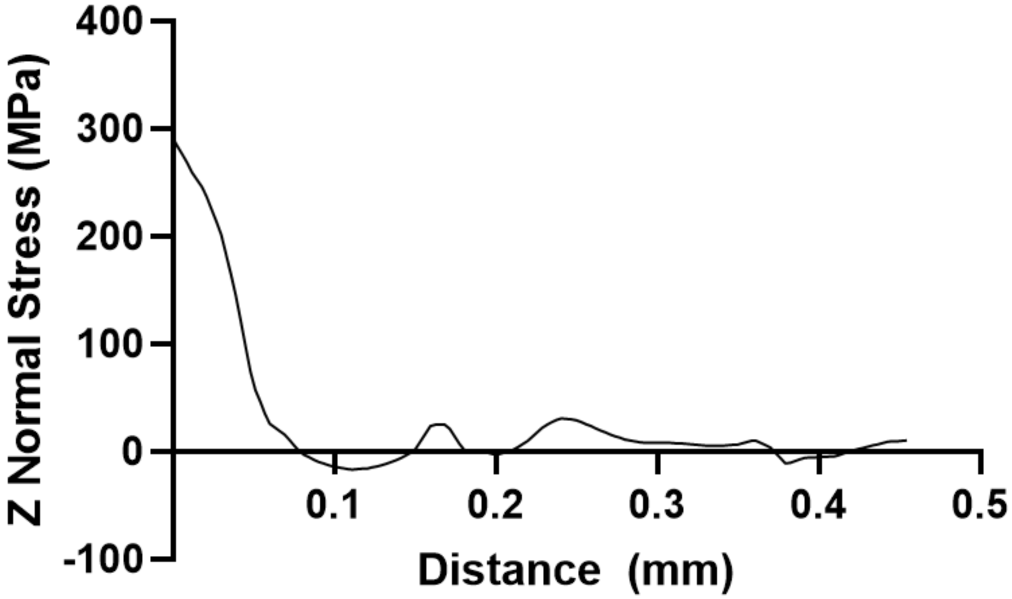

Figure 67: Z Normal Stress along Y direction

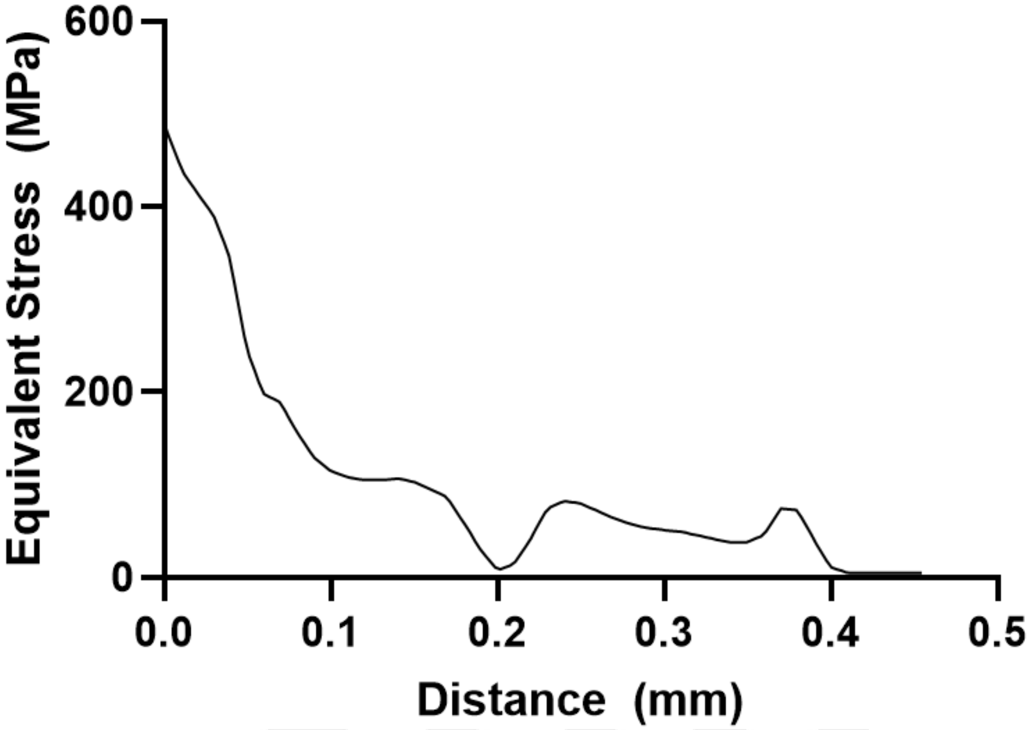

Figure 68: Equivalent Stress along Y direction

Since the baseplate as well as previously consolidated layers act as heat sink, extremely large and directional thermal gradients arise around the melt pool which result in residual stresses. The formed stress component in the direction of laser path is greater than the component perpendicular to laser path. At the top surfaces, shrinkage of newly solidified melt pool is restrained by neighbouring solid metal which in turn results in tensile residual stresses in the horizontal direction. On the other hand at the middle location of the part, compressive residual stresses exist for all stress components.

4.3 Mechanical Analysis vs Thermomechanical Analysis

Mechanical analysis requires less solve time than thermomechanical analysis due to the fact that mechanical analysis leaves out thermal calculation. For models containing small number of elements, the solve time difference between M and TM analysis may be insignificant but as the number of elements increase, the solve time difference is getting more noticable. Below the comparative figure for both analysis types is given.

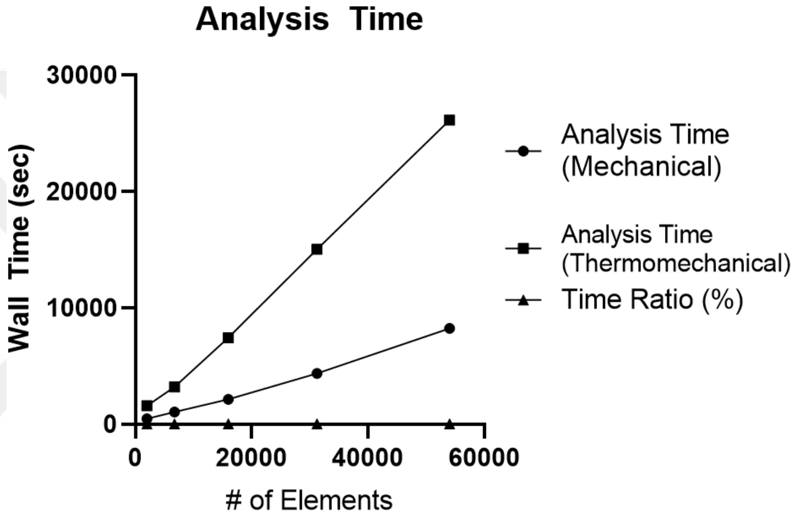

Figure 69: Comparison of analysis times of Mechanical and Thermomechanical analysis

It should also be noted that as the number of elements increase, the ratios of solve time between M and TM analysis remains constant regardless of total number of elements.

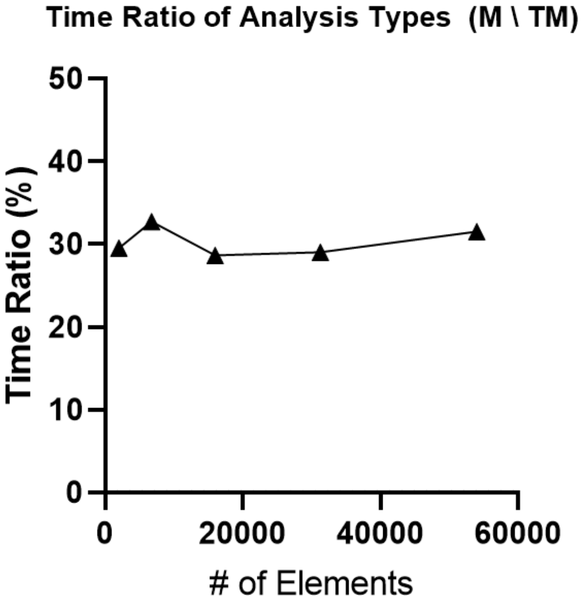

Figure 70: Ratio of analysis times of Mechanical and Thermomechanical analysis

4.4 Thermal Examination

A thermal analysis is run for a 20x20x20 mm3 cube. A single node locating at the mid-portion of the cube is selected as given below figure;

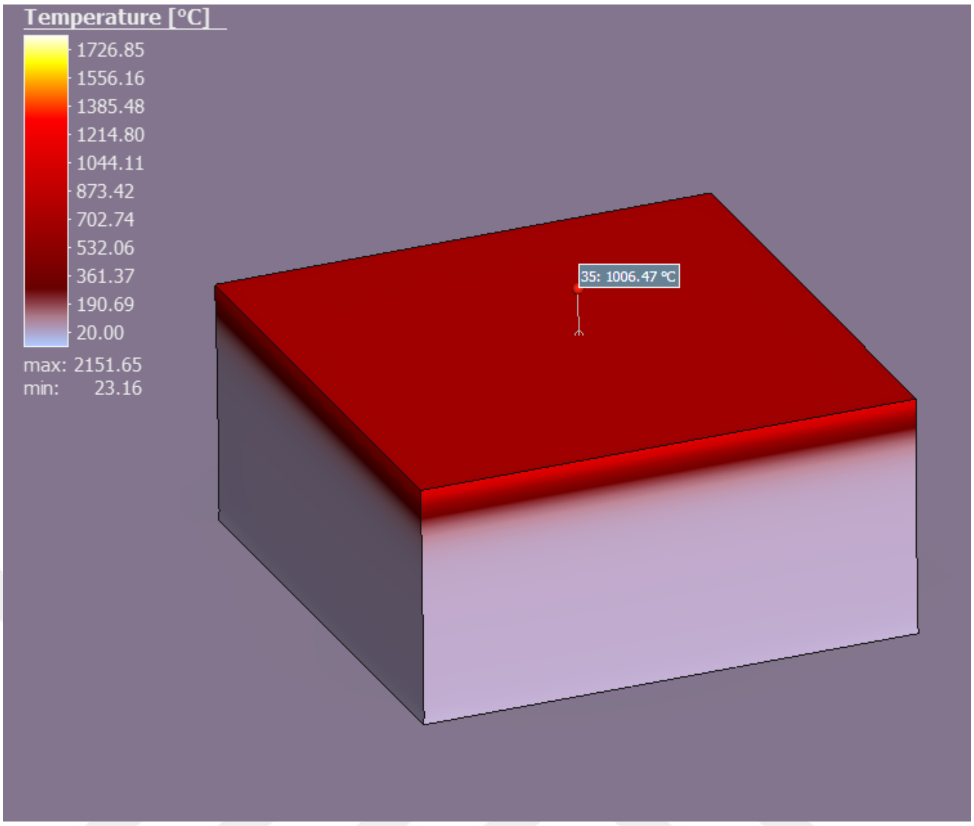

Figure 71: Temperature of top node of cube with edge length of 20 mm

Temperature history of the selected node is given below. Note that at the onset of assigning the node, the peak temperature is 2150 C consistent with the thermal calibration.

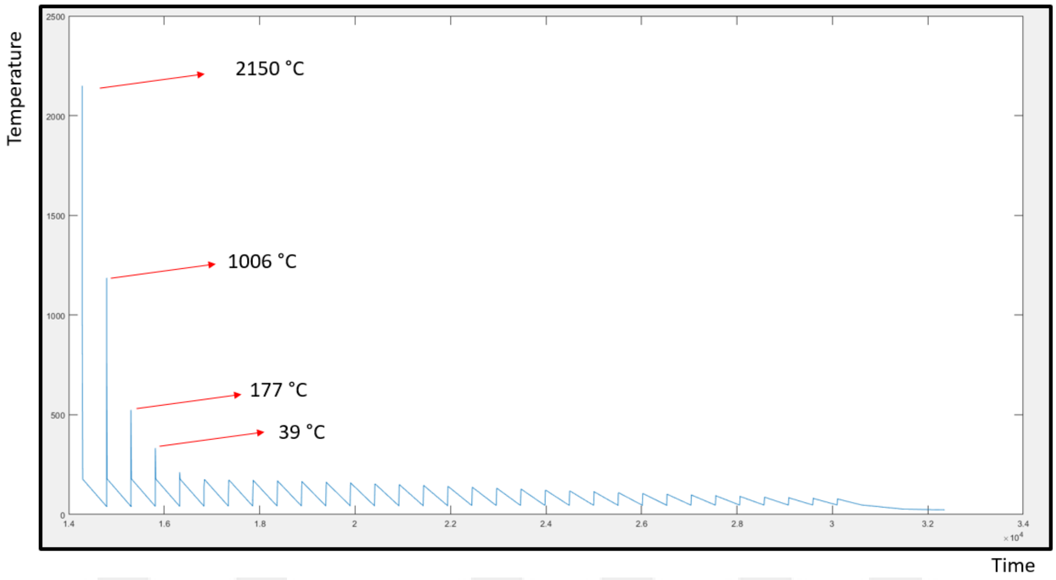

Figure 72: Thermal history of selected node

However, cooling rate of the hot top layer until the addition of another hot layer is calculated as 7666 K/sec. In real case cooling rate is on the order of 10^6 K/sec for SLM process. It is due to the simplified simulation approach in Simufact Additive. Layer thickness of the model is equal to the voxel mesh size which is 0.5 mm. However in real case for SLM processing, layer thickness is much thinner, generally between 20 µm- 50 µm as being one-tenth of the size of voxel mesh. Another simplification is that All elements of the hot top layer is assigned simultaneously where the scan pattern is neglected and thermal histories may not accurately reflect the real case. Nonetheless these simplifications are acceptable because when the layer thickness of model is decreased and scan pattern is considered for part scale problems, simulations get more computationally demanding.

4.5 Distortion

Laser scanned impellers did not yield satisfactory results since surface data obtained at deeper locations of the complex part is corrupted. Therefore true comparison of distortion values cannot be done with laser scanned data.

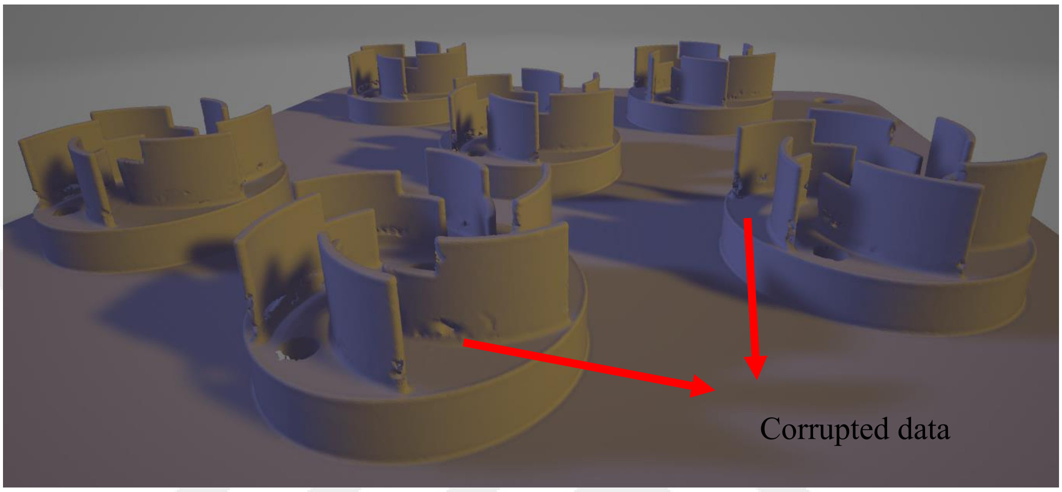

Figure 73: Laser Scanned Surface Data

4.6 Residual Stress

4.6.1 Simulation and Contour Residual Stress Measurement Results

Thermomechanical and Mechanical analysis results as well as Contour residual stress measurement results of distribution of residual stress component perpendicual to the cut plane of cross parts are given below;

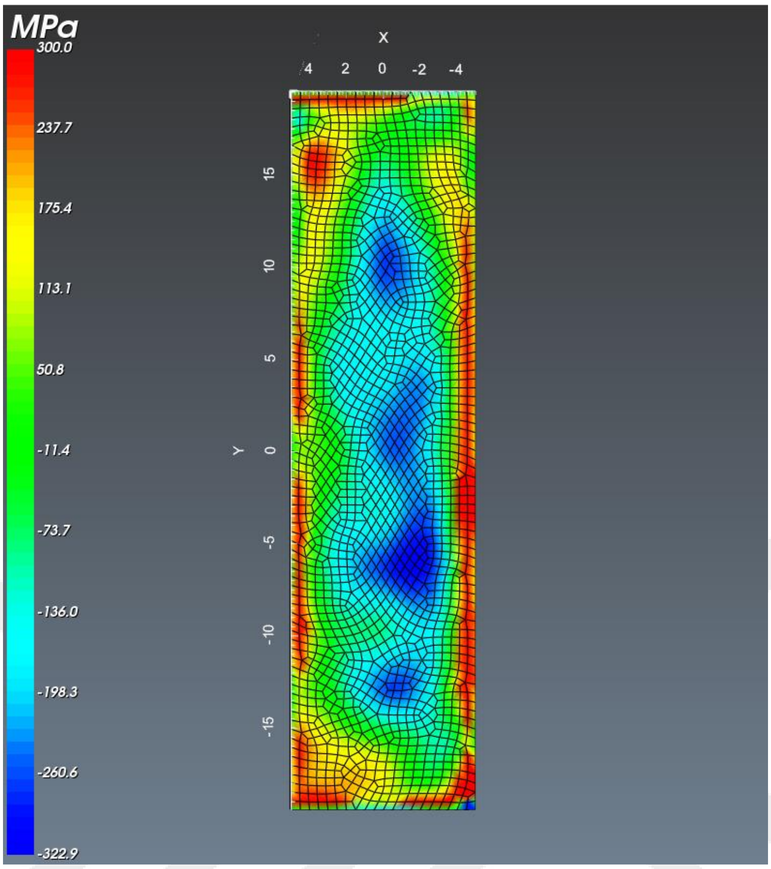

Figure 74: Contour Method: Distribution of σyy component of residual stress at the Y-cut surface of parallelly scanned Cross 1

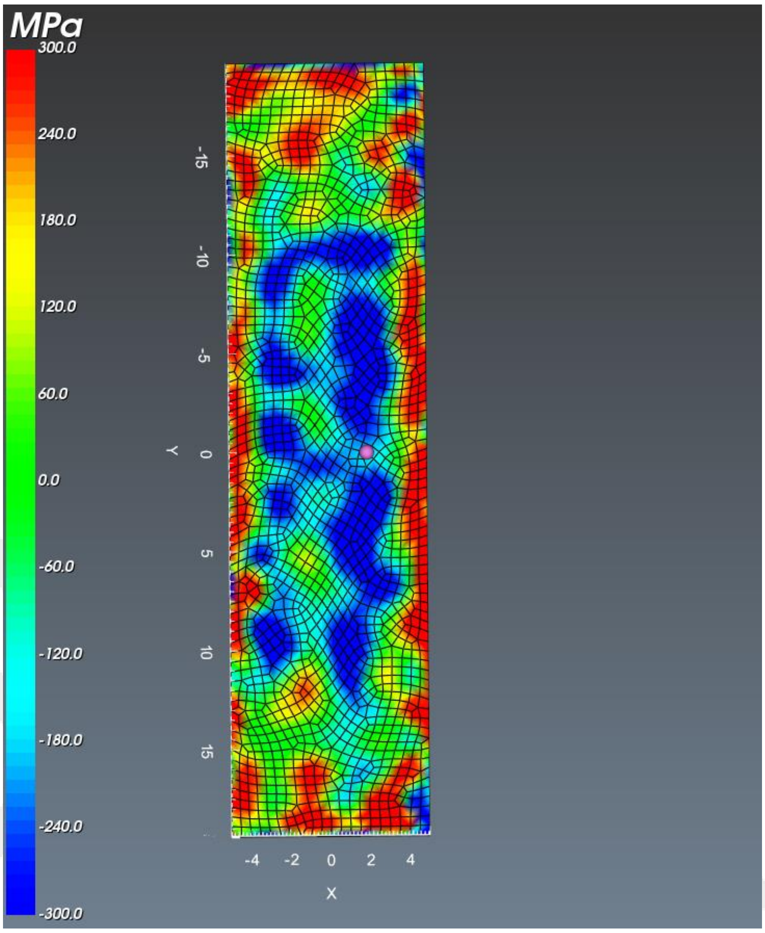

Figure 75: Contour Method: Distribution of σxx component of residual stress at the X-cut surface of parallelly scanned Cross 2

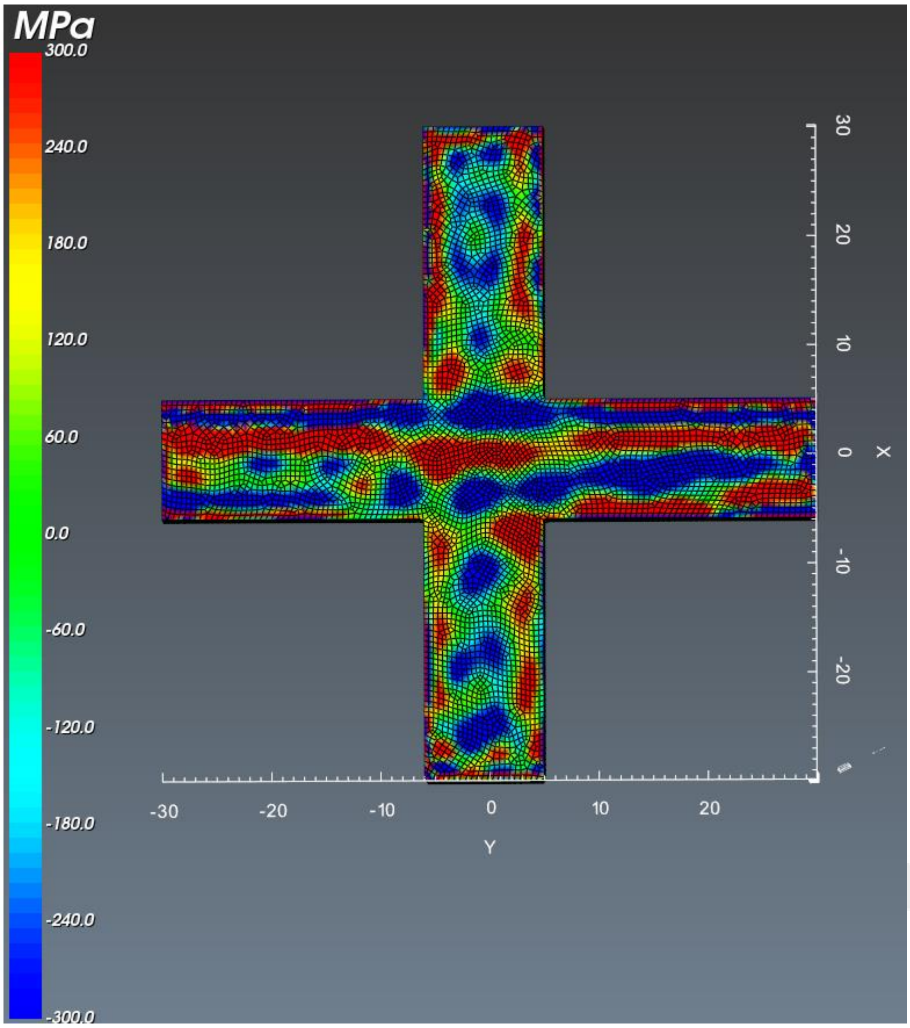

Figure 76: Contour Method: Distribution of σzz component of residual stress at the Z-cut surface of parallelly scanned Cross 3

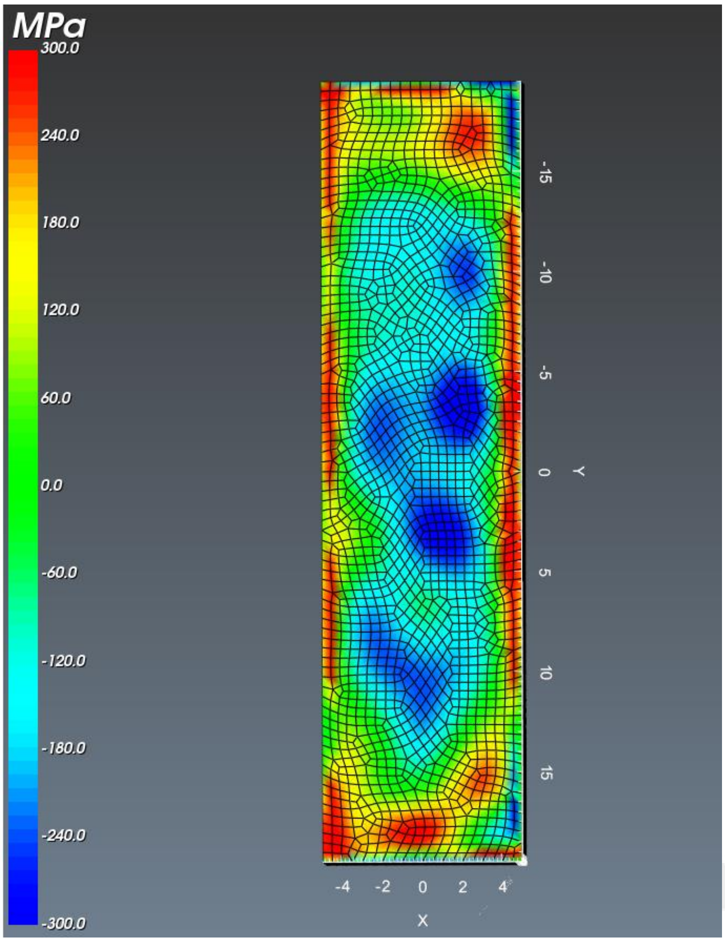

Figure 77: Contour Method: Distribution of σyy component of residual stress at the Y-cut surface of rotationally scanned Cross 4

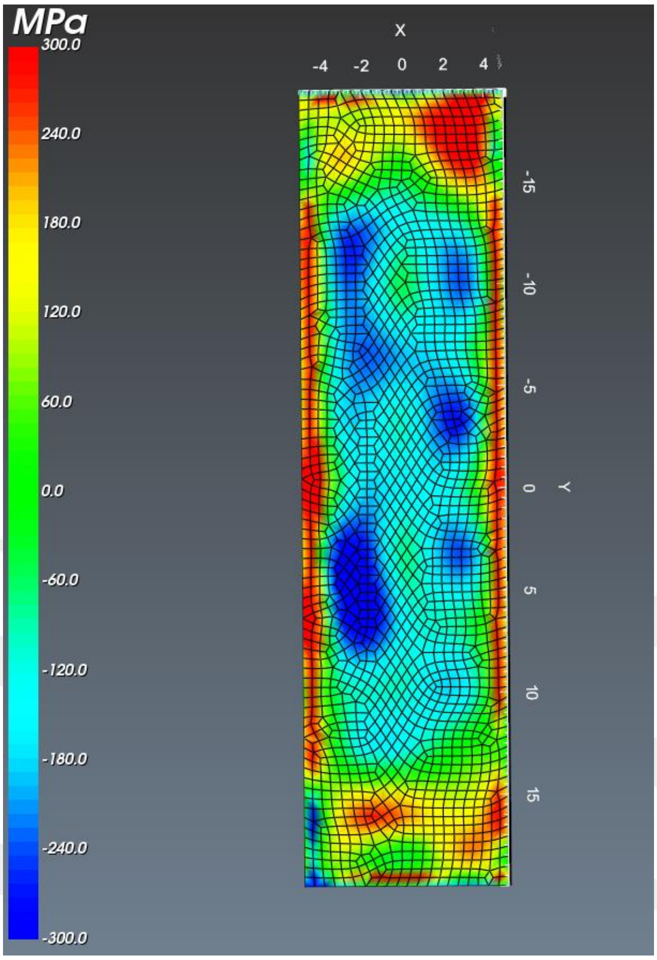

Figure 78: Contour Method: Distribution of σxx component of residual stress at the X-cut surface of rotationally scanned Cross 5

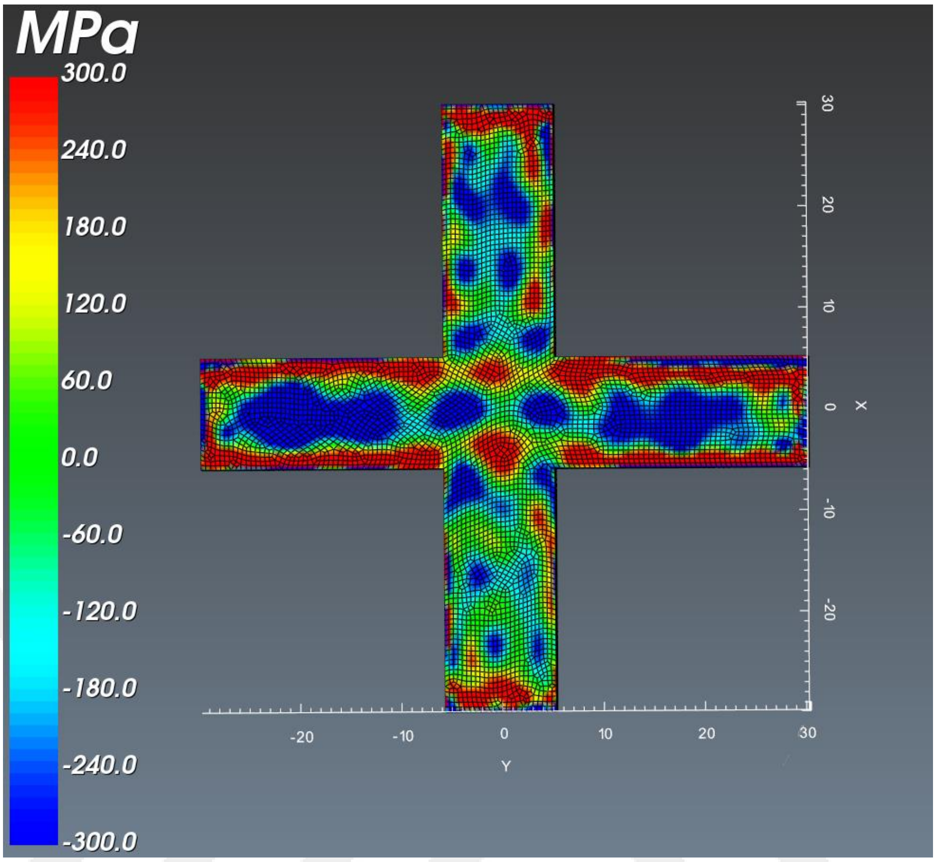

Figure 79: Contour Method: Distribution of σyy component of residual stress at the Z-cut surface of rotationally scanned Cross 6

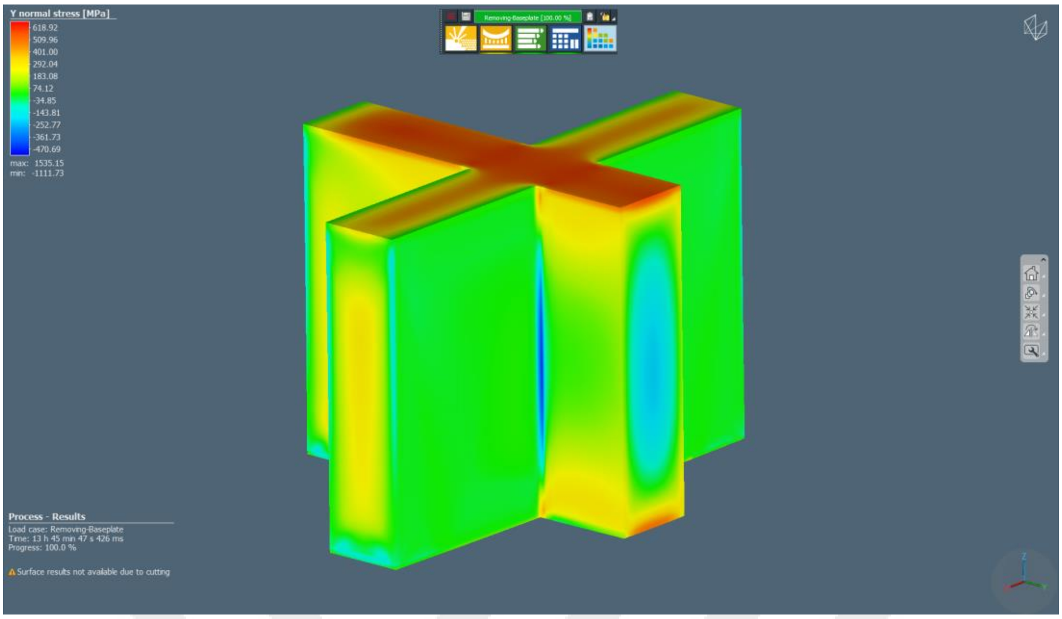

Process - Results
Load case: Removing-Baseplate
Time: 13 h 45 min 47 s 426 ms
Progress: 100.0 %

⚠ Surface results not available due to cutting

Figure 80: Thermomechanical Analysis: Distribution of σyy component of residual stress at the Y-cut surface of rotationally scanned Cross 4

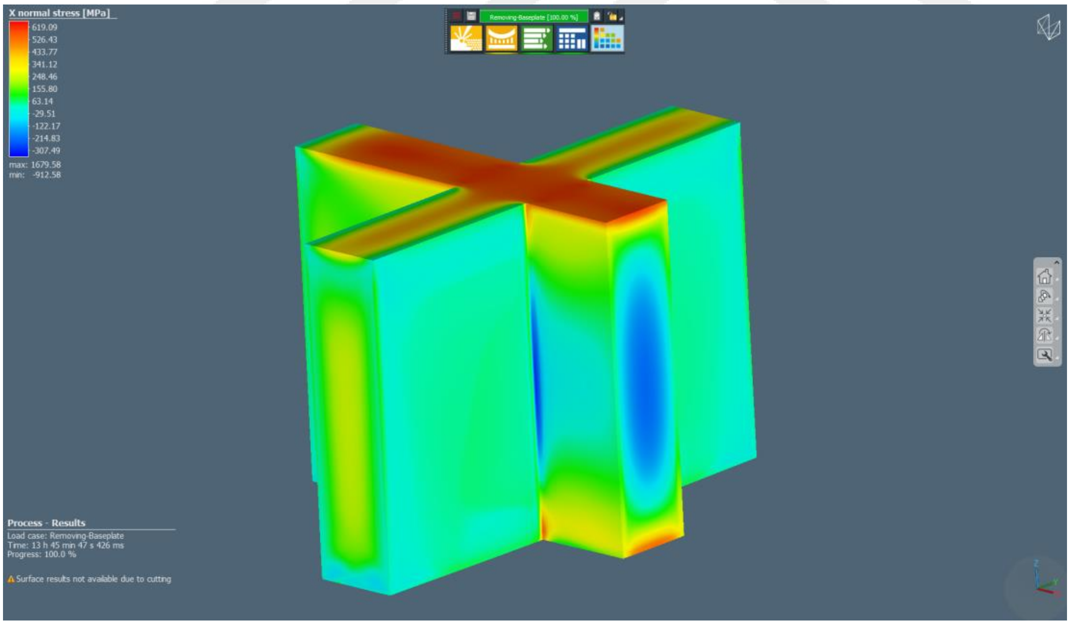

Process - Results
Load case: Removing-Baseplate
Time: 13 h 45 min 47 s 426 ms
Progress: 100.0 %

⚠ Surface results not available due to cutting

Figure 81: Thermomechanical Analysis: Distribution of σxx component of residual stress at the X-cut surface of rotationally scanned Cross 5

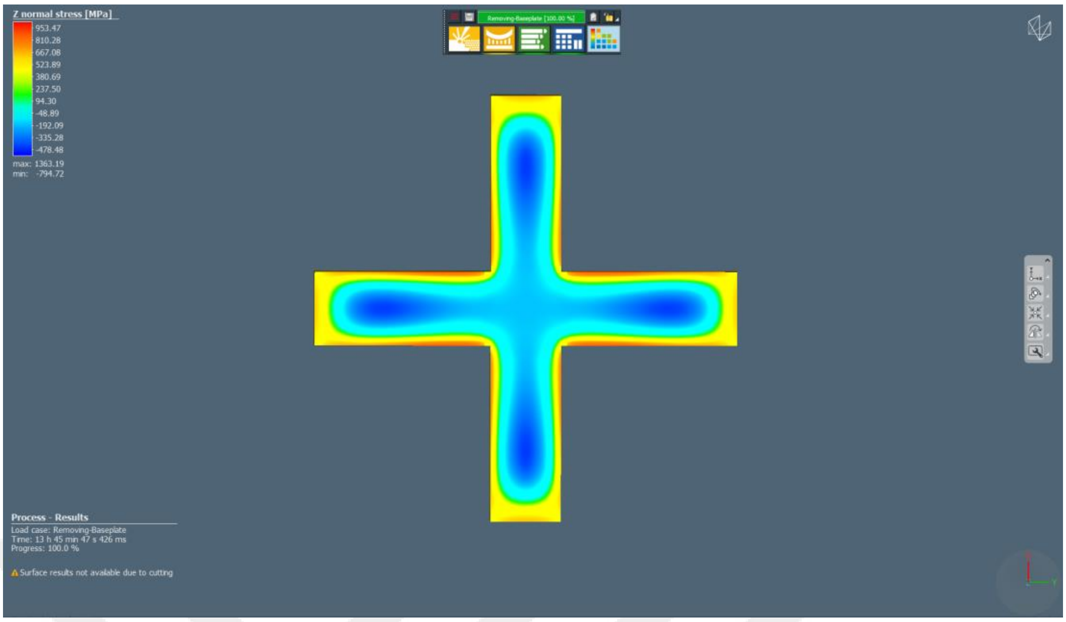

Figure 82: Thermomechanical Analysis: Distribution of σzz component of residual stress at the Z-cut surface of rotationally scanned Cross 6

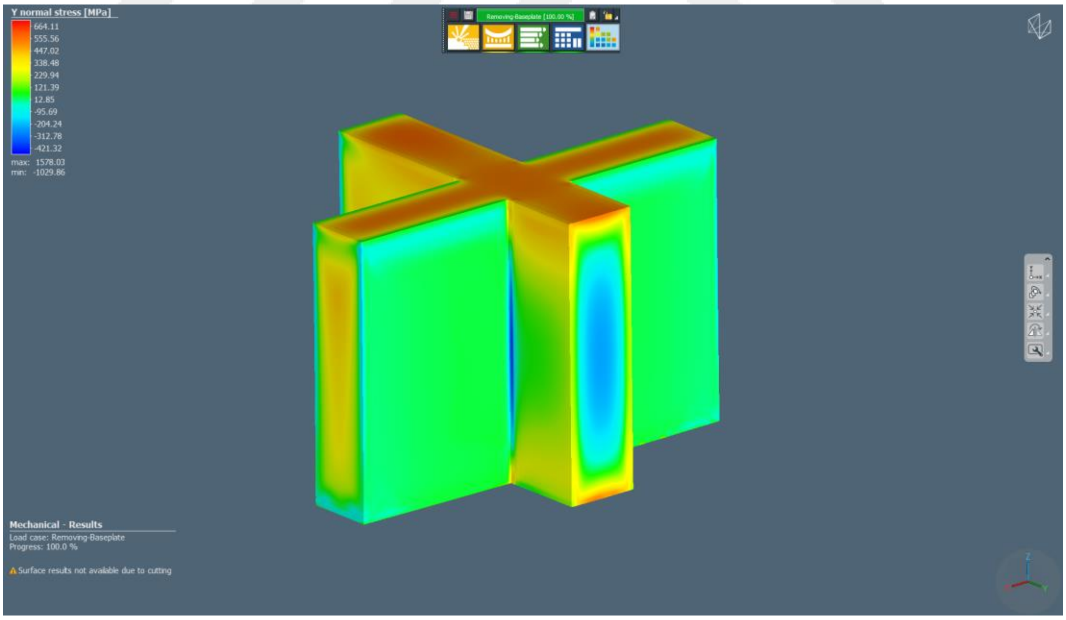

Figure 83: Mechanical Analysis: Distribution of σyy component of residual stress at the Y-cut surface of parallelly scanned Cross 4

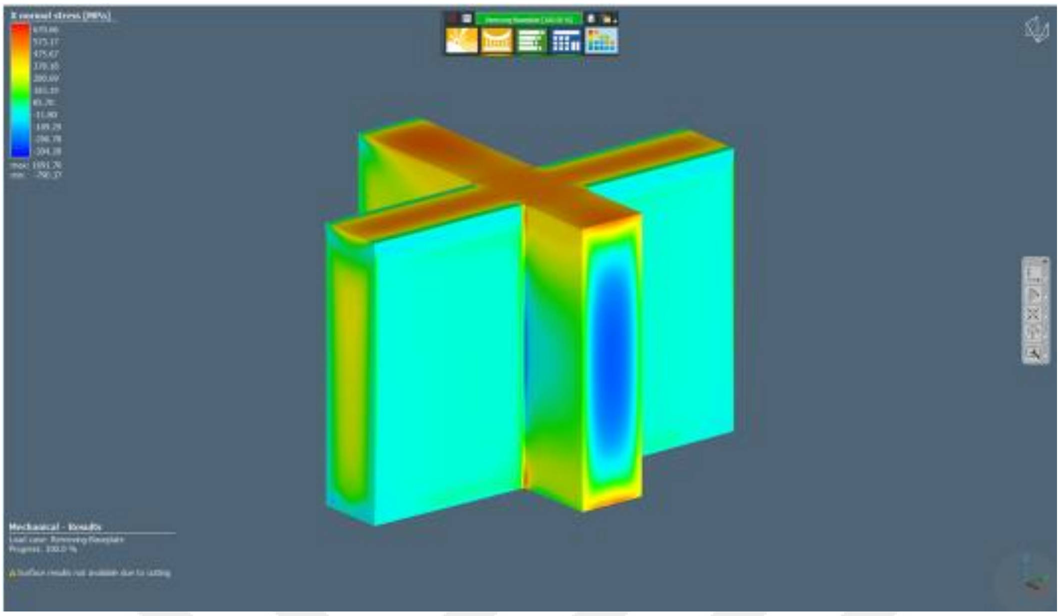

Mechanical - Results
Load case: Removing-Baseplate
Progress: 100.0 %
Surface results not available due to cutting

Figure 84: Mechanical Analysis: Distribution of σxx component of residual stress at the X-cut surface of parallelly scanned Cross 5

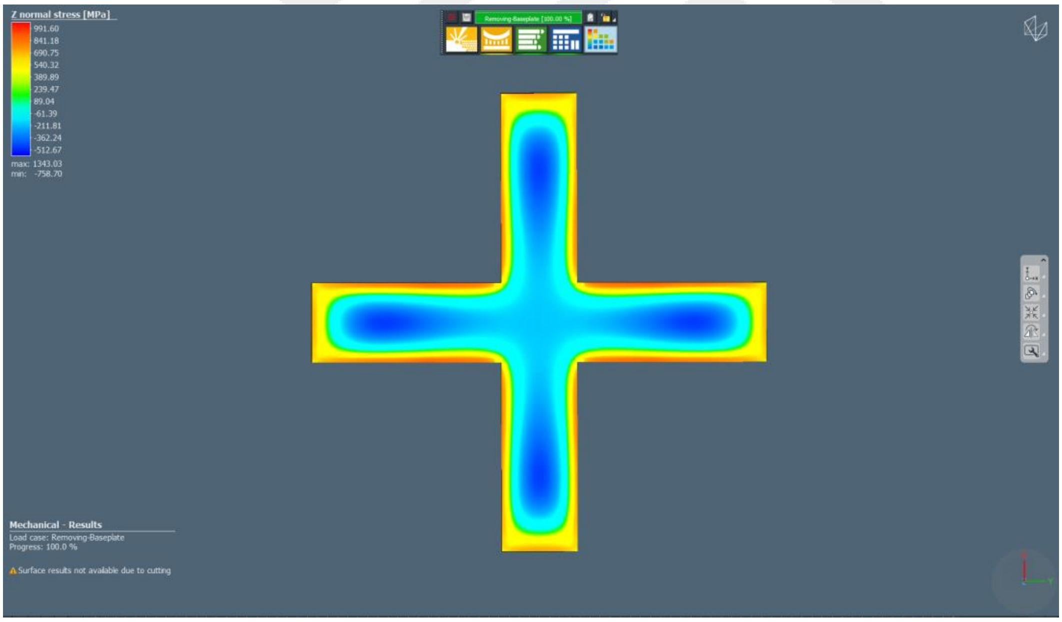

Mechanical - Results
Load case: Removing-Baseplate
Progress: 100.0 %
Surface results not available due to cutting

Figure 85: Mechanical Analysis: Distribution of σxx component of residual stress at the X-cut surface of parallelly scanned Cross 6

4.6.2 Comparison of Simulation Results with Contour Method

Comparison of simulation results with contour residual stress measurements of σxx and σyy components for both Cross 4 and Cross 5 along the A-B and C-D lines on their cut planes are given below.

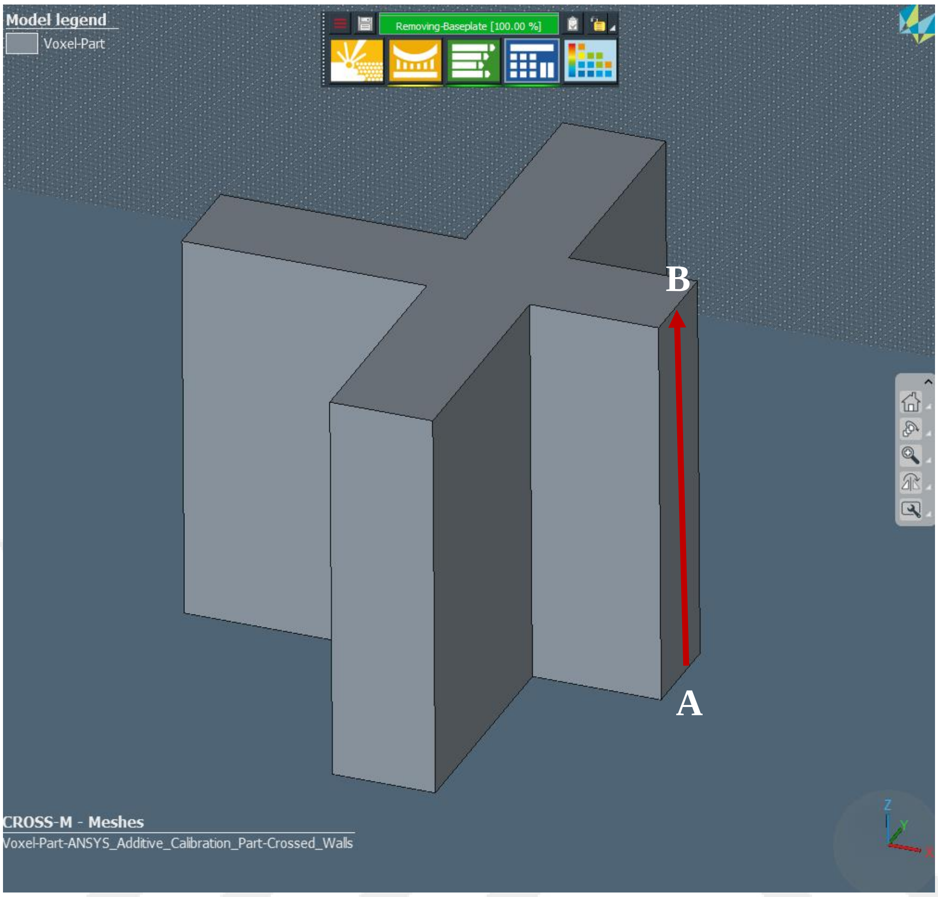

Figure 86: Stress distribution on X-Cut of cross part along A-B line (Cross 5)

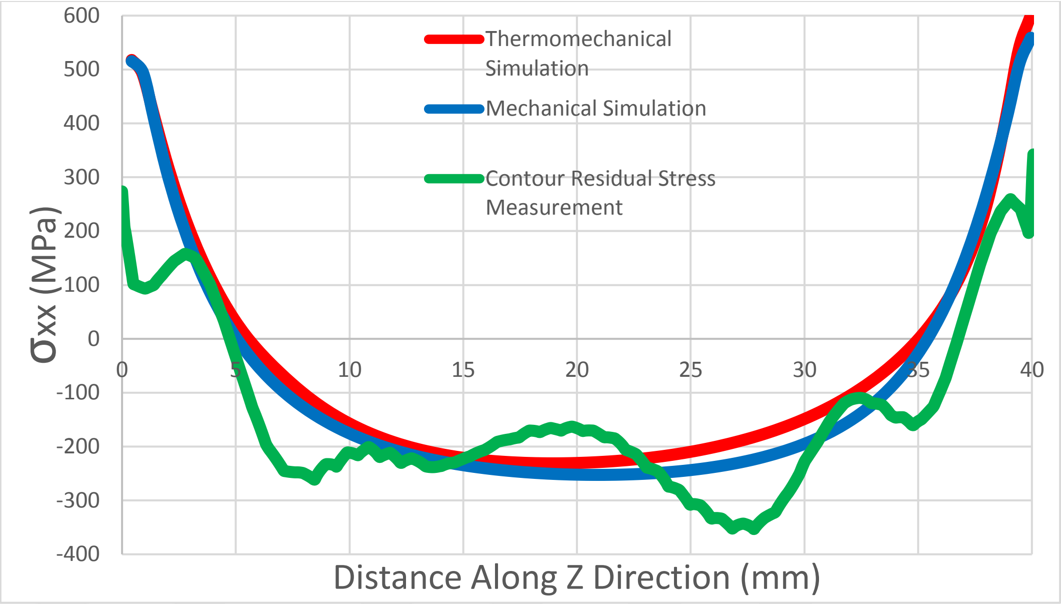

Figure 87: σxx on X-Cut surface of cross part along A-B line

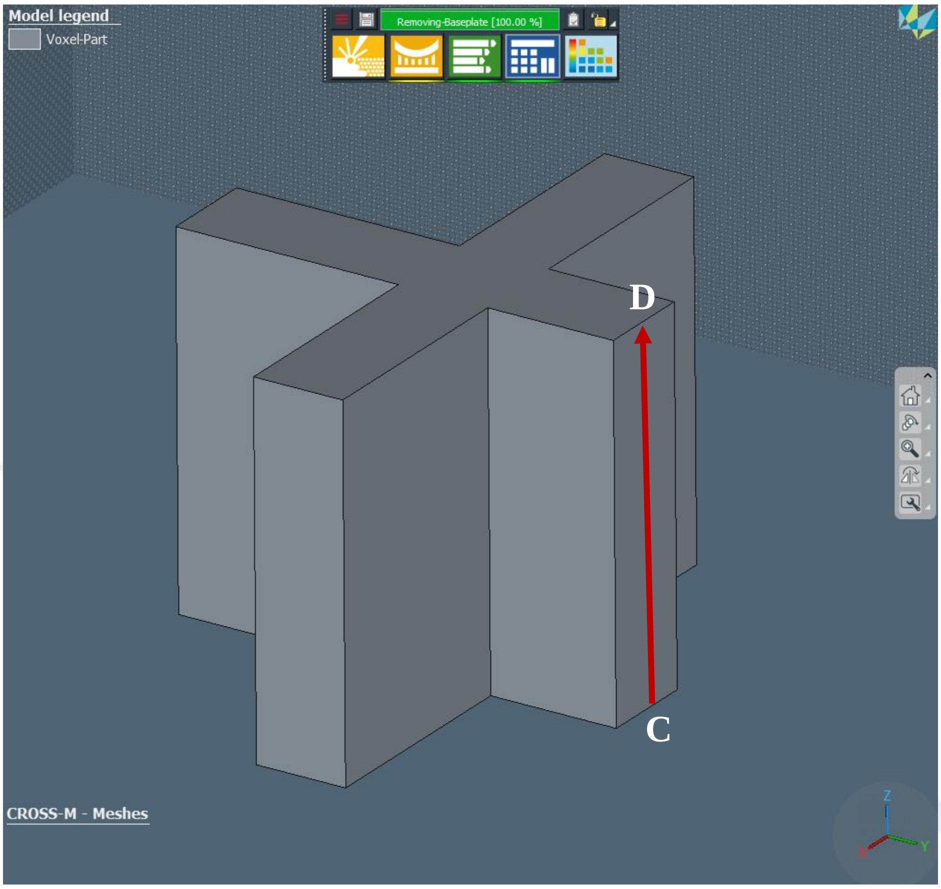

Figure 88: Stress distribution on Y-Cut of cross part along C-D line

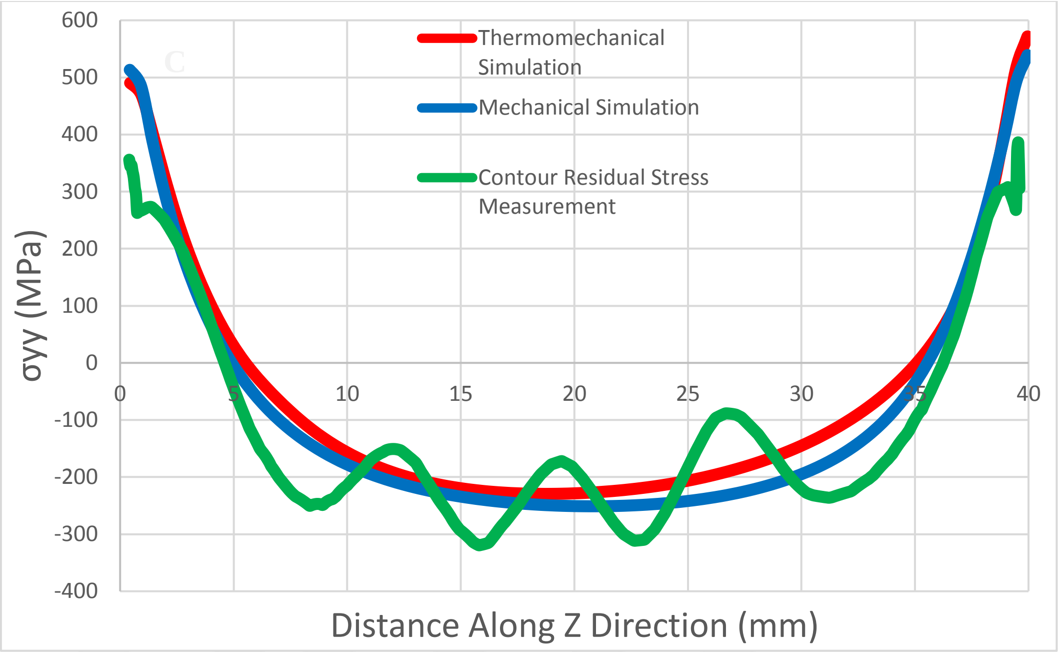

Figure 89: σyy on Y-Cut of cross part along C-D line (Cross 4)

Thermomechanical analysis as well as mechanical analysis show same trend with contor residual stress measurements. The tension to compression transition show consistency for both simulation and experimental results. Secondly, Contour analysis in compressive (mid) region, show local fluctuations along the measured direction, however simulation results show smooth trend. Thirdly, even simulation results at mid region show similar trend with contour results, the tensile region at far ends of the yielded large errors. Contour measurements are resulted by far below stress levels than simulations, this may be due to excessive localized plastic deformation at high stress level regions. It is also stated that in previous studies as the residual stress levels reaches to the materials yield strength, error of the cutting procedure increases due to excessive deformation. Simulation results show 500 MPa stress levels at the edges while contour results show approximately 300 MPa. Special attention should be paid for the clamping procedure of specimens before EDM cutting in order to minimize cutting errors.

Comparison of simulation results with contour residual stress measurements of σzz component for Cross 6 along the X and Y directions (E-F and G-H lines) on their cut plane are given below.

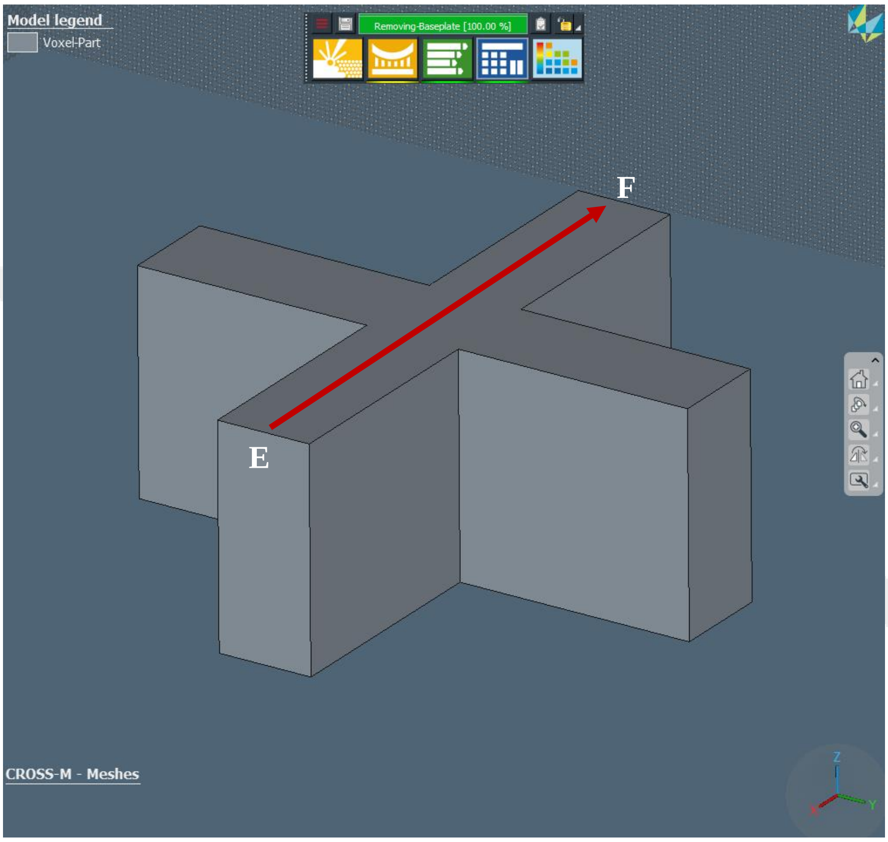

Figure 90: Stress distribution on Z-Cut of Cross 6 along X-Direction (E-F line)

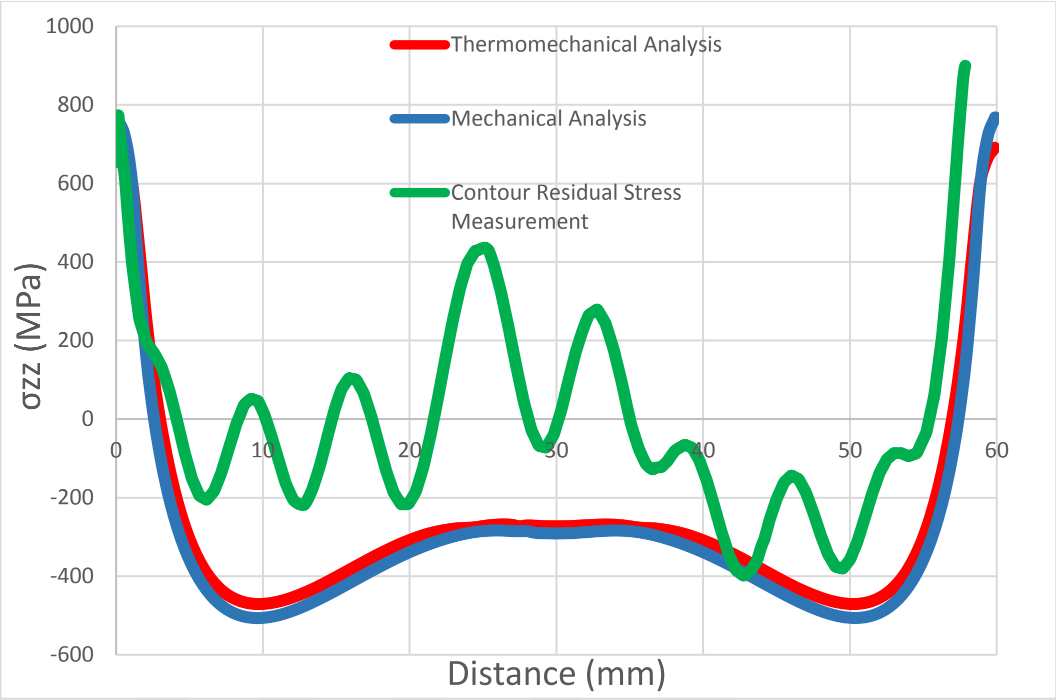

Figure 91: Z Normal Stress on Z-Cut of Cross 6 along X-Direction (E-F line)

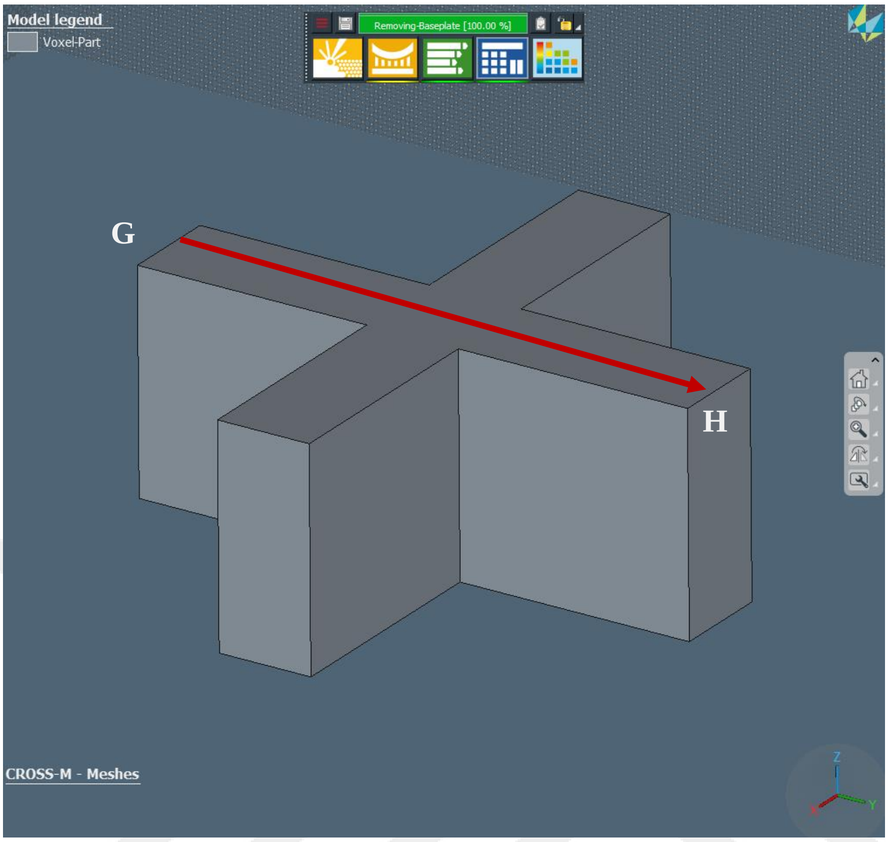

Figure 92: Stress distribution on Z-Cut of Cross 6 along Y-Direction (G-H line)

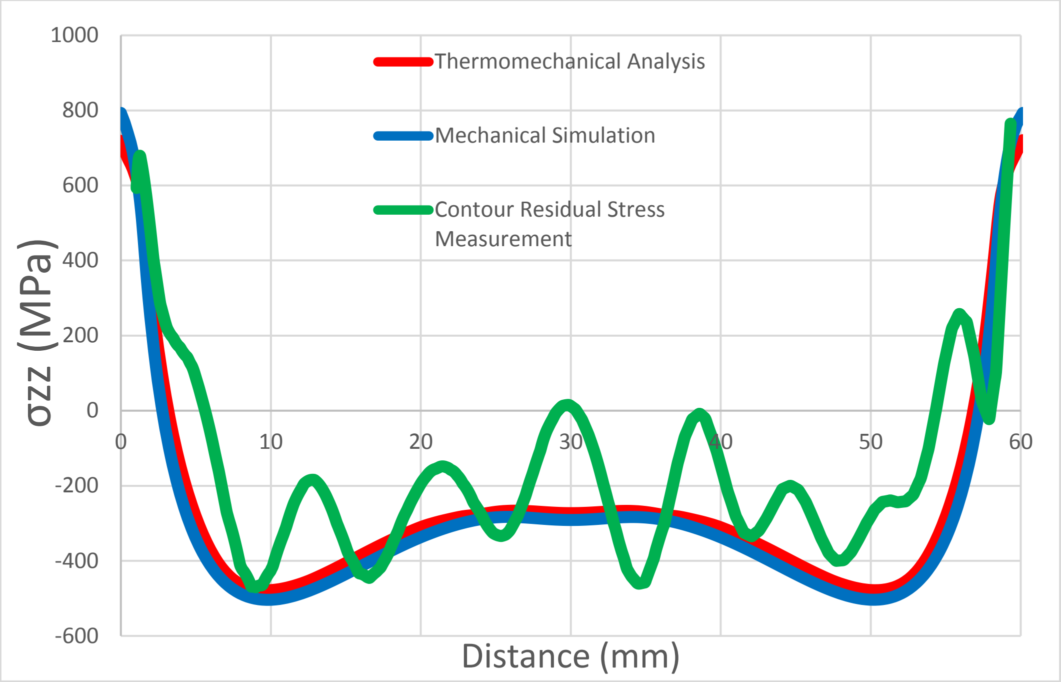

Figure 93: Z Normal Stress on Z-Cut of Cross 6 along Y-Direction (G-H line)

Considering residual stress distribution for X, Y and Z cut surfaces, higher levels of stresses develop for σzz which build corresponds to the build direction for the SLM'ed parts. σzz reaches up to 800 Mpa tensile stresses at 2 ends of the part specified in Figures 89-91. Furthermore simulation results and contour residual stress measurements for σzz show similar trends for both X and Y directions but fluctuations are observed at mid-location of the part and furthermore deviation of experimental results with simulation is higher for data obtained at X direction than Y direction. This is due to cutting procedure of EDM is done through the Y direction therefore in the perpendicular X direction, error increases. Further validation is required with XRD residual stress measurement at mid locations. Special attention also should be paid for the direction of EDM cutting procedure in order to minimize deformations and resulting errors.

4.6.3 Evaluation of Crosses Regarding Contour Method

Comparison of Contour results for Cross 3 (parallel scan) and Cross 6 (rotational scan) are given below;

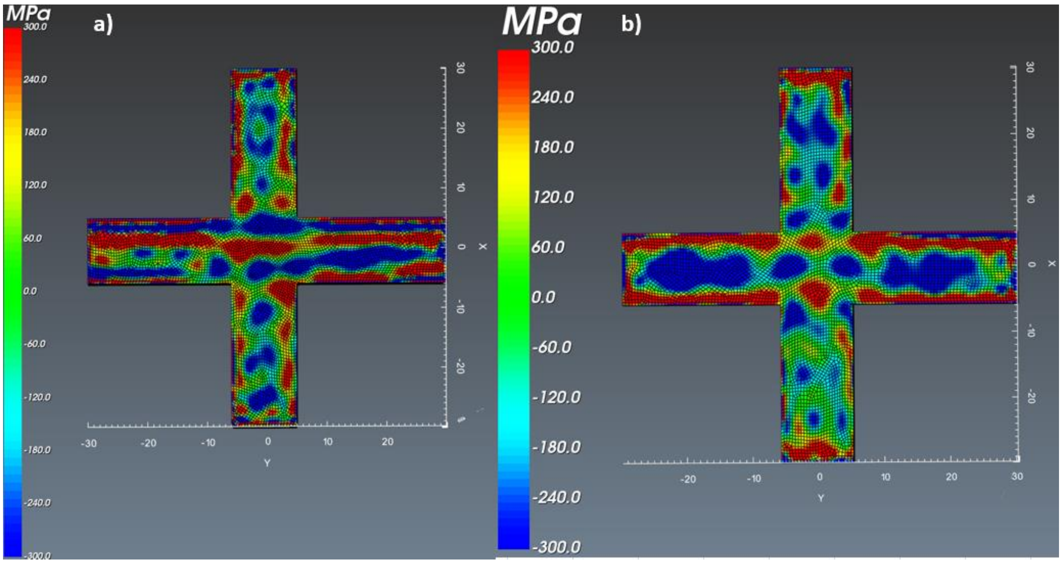

Figure 94: Comparison of Contour results: a) Cross 3 (parallel scan) b) Cross 6 (rotational scan)

For cross 3, which is parallel scanned at X direction, a banded formation of σ_{zz} stress component is observed. However this banded structure is not observed in rotationally scanned cross 6. Furthermore in cross number 6, a red shell surrounding the blue core indicating that tensile stresses formed at edges while compressive stresses at middle regions. SLM'ed parts likely to have compressive residual stress at the mid-section of the part and tensile at the edges. Besides, residual stress is highly concentrated at the part-baseplate interface for parts which are not cut from baseplate. At the top surface or edges, peak tensile residual stress is calculated.

Comparison of contour residual stress measurement of crosses 1-4 and 2-5 are given below.

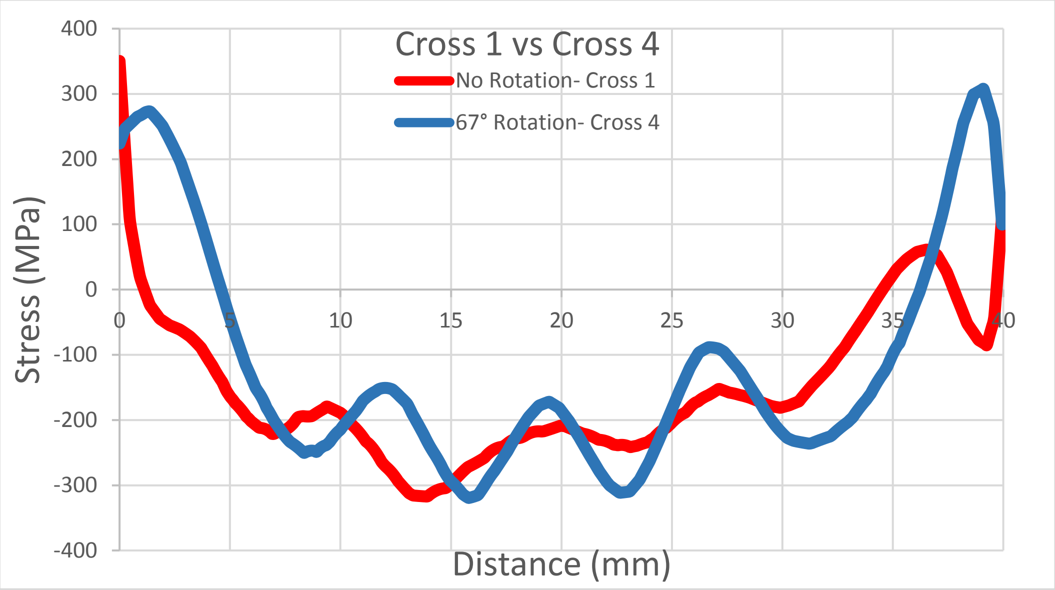

Figure 95: Residual Stress profile of Crosses 1 and 4 along their height

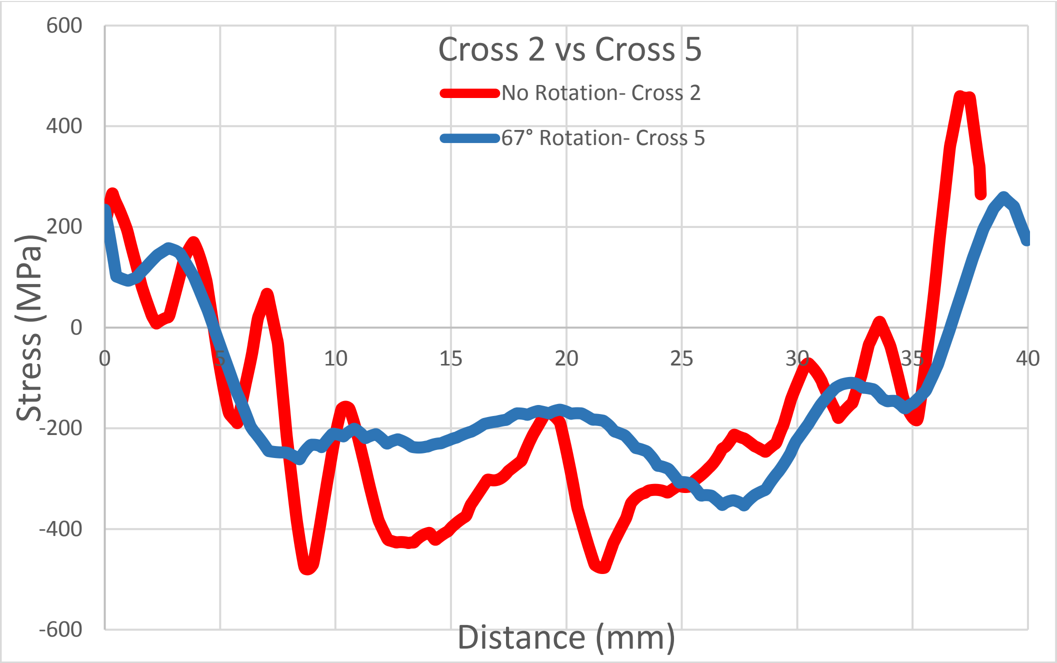

Figure 96: Residual Stress profile of Crosses 2 and 5 along their height

For crosses 1 and 4 which are scanned by 0 and 67 degree rotation angles respectively, exhibited similar residual stress trends along their Y-cut planes. On the other hand comparing crosses 2 and 5, cross 2 resulted in slightly higher residual stress levels along their X-Cut planes due to the higher thermal gradients formed by parallel scanning along X direction.

Contour residual stress measurements results of crosses 1-2 and 4-5 are shown below.

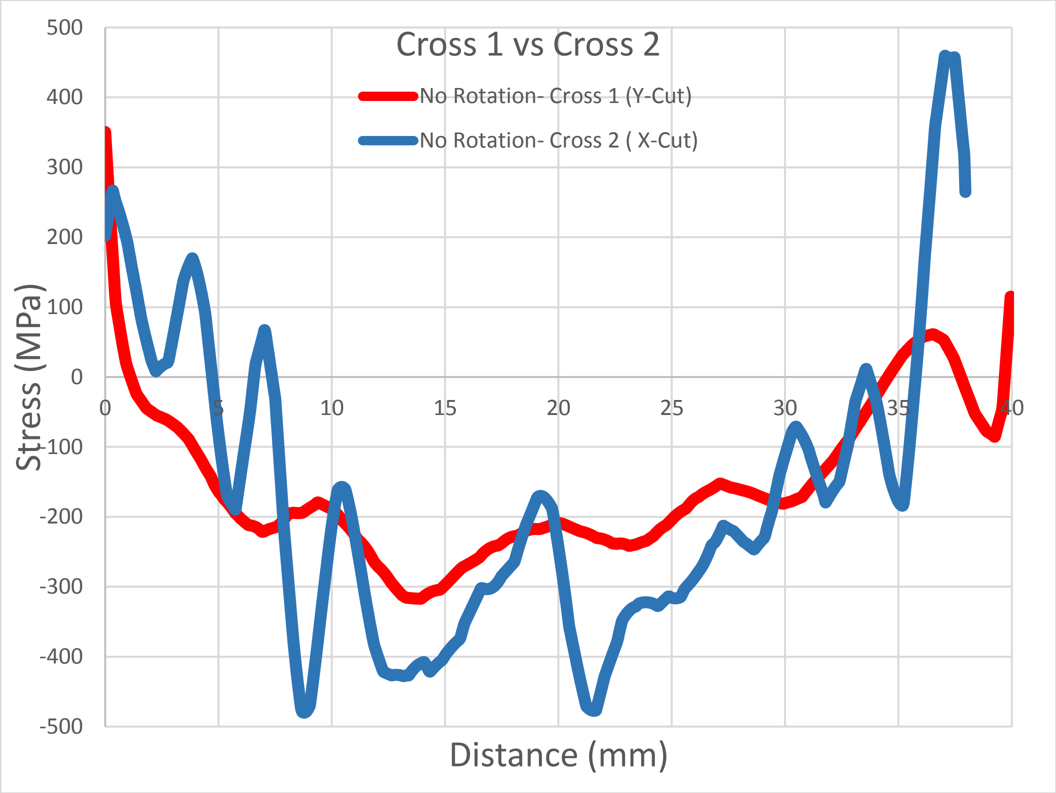

Figure 97: Residual Stress profile of Crosses 1 and 2 along their height

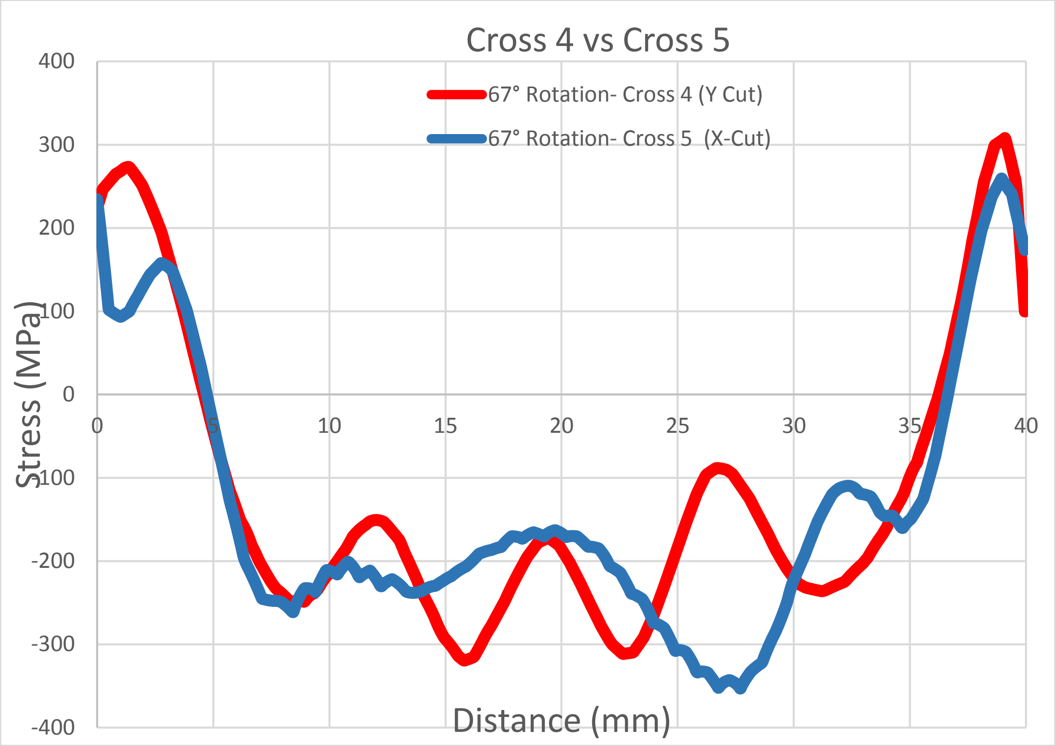

Figure 98: Residual Stress profile of Crosses 4 and 5 along their height

Note that contour residual stress method measures the residual stress component perpendicular to the cut plane. For cross number 2, which is cut perpendicular to the scan vectors, resulted in up to %50 higher levels of compressive stresses in the mid region and tenile stresses at the edges than cross 1 which is cut parallell to the scan vectors. It is explained by residual stress component along the scan direction is developing at higher levels than residual stress component perpendicular to the scan direction. Therefore cross number 2 resulted in higher residual stress levels. On the other hand, crosses number 4 and 5, which are scanned by vectors rotating 67 degree for each consecutive layers, resulting in same magnitude of stress distribution for both X and Y planes of crosses 4 and 5. Rotation of scan vectors homogenize the stress distribution. Overall conclusion from this comparison is that the weight of the stress component shifts towards the scanning direction. This is also consistent with simulation results of mesoscale analysis given in previous sections.

4.7 Critical Temperatures

Critical temperatures obtained from dilatometry tests are given below for wrought and SLM'ed as built 17-4 PH are given below;

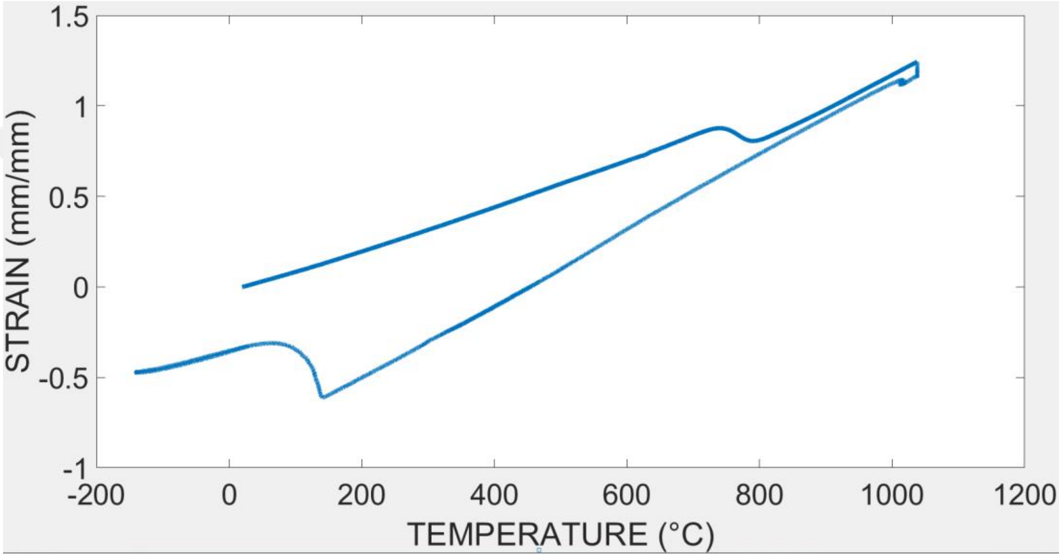

Figure 99: Dilatometry test result

Table 7: Critical Temperatures of Wrought & SLM'ed 17-4 PH Stainless Steel

Specimen Type	**Direction of Cut**	**Critical Temperatures**			
		AC1	AC3	MS	MF
Wrought	X	723	840	210	23
	Y	720	845	205	25
	Z	721	838	207	33
	Average	**721**	**841**	**207**	**27**
SLM	X	745	885	235	47
	Y	750	900	230	37
	Z	752	890	233	52
	Average	**749**	**892**	**233**	**45**

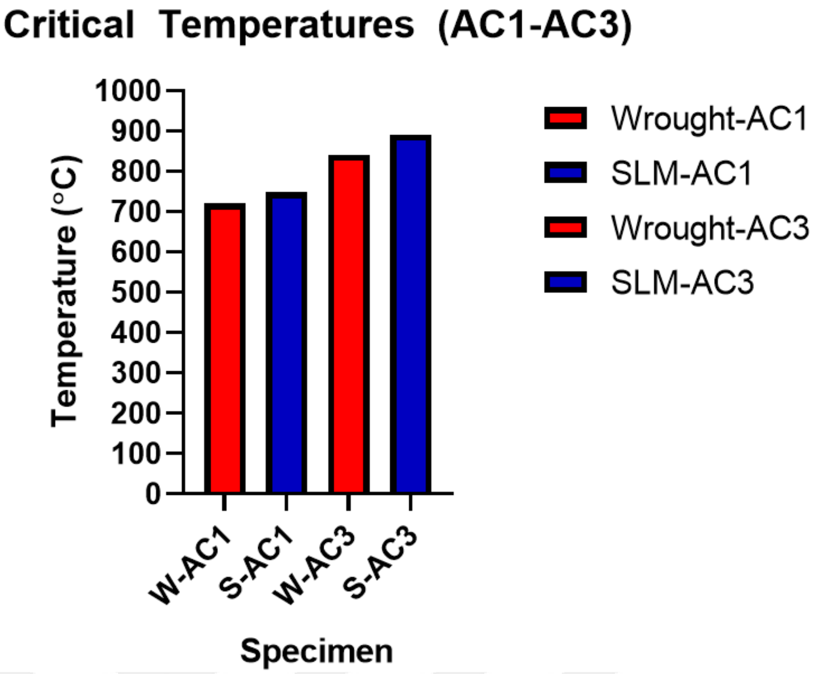

Figure 100: Critical Temperatures (AC1-AC3)

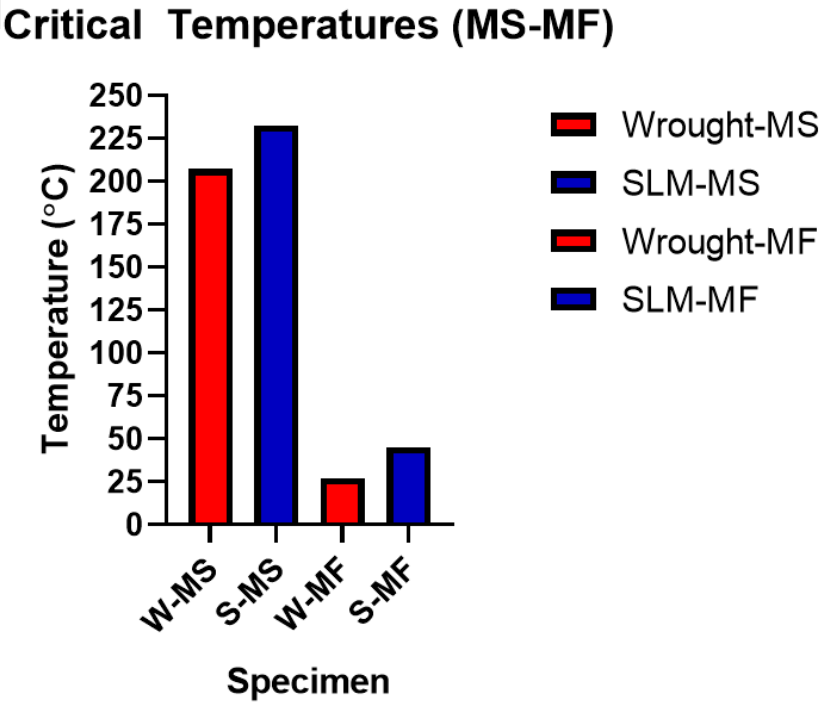

Figure 101: Critical Temperatures (MS-MF)

CHAPTER 5

CONCLUSION

In order to increase the accuracy of the critical material data needed for the simulations of the SLM process and heat treatments, critical parameters such as thermal expansion coefficient is obtained by the experimental dilatometry test and non-critical parameters were obtained computationally from JmatPro databases therefore a hybrid approach was studied. In JmatPro software, the phase change sequence of 17-4 PH Stainless Steel was taken into account during SLM processing, high temperature ferrite phase properties were extrapolated down to room temperature and the SLM processing is intended to be simulated accurately in terms of material behavior.

The application of the Contour method is an industrially practical and easy method which is used for 2D mapping of the stress component perpendicular to the cut surface of the part on the cut surface. Thermomechanical and Mechanical approaches in Simufact Additive software are compared and verified with the contour method. Stress profile trends and tension-compression transitions are largely consistent, small to moderate differences in numerical magnitude between simulation and test results. Although the amount of deformation after cutting is low in relatively small parts, the trend in the simulations with the contour method has resulted in a consistent manner. In addition, thermomechanical and mechanical simulations yields very similar results, since the thermal effect caused by thermal accumulation in small parts is low. Since mechanical analysis requires 1/3 less solution time compared to thermomechanical analysis with the same solving parameters, mechanical analysis is advantageous in small parts and especially in crowded baseplate where time is a criterion for the user. However, as the part size increases, the difference in the results of the two simulation approaches will also increase due to the change in the thermal history. Literature studies show that the deviation from experimental results increases as the particle size increases for mechanical analysis. The simulation type should be determined according to the user's expectation of time and accuracy. To better understand the difference between the results of simulation approaches for bulk parts, it is necessary to run the same simulations for bulk parts and experimental validation.

Another output of the contour method within the scope of the thesis is to reveal the effect of directional scanning in SLM. The effect of rotational and non-rotational scanning vectors for each successive layers on residual stress distribution is evaluated by taking advantage of the contour method. It is found that the contour method is effective in revealing this difference and understanding the evolution of stress components in different directions in the SLM process. In this context, the experimental results are supported by the mesoscale simulations run in Simufact Welding software where detailed laser movement were taken into account.

However, a disadvantage of the contour method is during practicing of the relatively small parts, small deformations occur after cutting which becomes harder to capture accurately considering the measurement capability of the CMM. This yields small fluctuations in the results. It is predicted that these fluctuations will disappear as the practiced cross section of the part is increased. With the right clamping system, similar comparisons should be made on large parts and the results should be evaluated. In overall, simulation studies were verified with the help of another simulation (contour method) within the scope of this thesis. For more comprehensive validation, a well accepted method is needed such as neutron diffraction which is high in accuracy and penetration depth.

Final conclusion is that as built parts come out with some shrinkage. Since the part geometry is relatively small and complex for the impeller geometry, the deformations are very small and uninterpretable. Therefore, it is practically not possible to capture the deformations that occur after built or heat treatment with the

CMM and compare these deformations. In this sense the built and heat treatment deformations should be measured and interpreted by creating appropriate datums either on more primitive and large geometries or on parts with more pronounced thickness-thinness transitions.

REFERENCES

[1] T. D. Ngo, A. Kashani, G. Imbalzano, K. T. Q. Nguyen, and D. Hui, "Additive manufacturing (3D printing): A review of materials, methods, applications and challenges," *Compos. Part B Eng.*, vol. 143, no. February, pp. 172–196, 2018, doi: 10.1016/j.compositesb.2018.02.012.

[2] M. Schneck *et al.*, "Evaluating the use of additive manufacturing in industry applications," *Procedia CIRP*, vol. 81, pp. 19–23, 2019, doi: 10.1016/j.procir.2019.03.004.

[3] G. Gong *et al.*, "Research status of laser additive manufacturing for metal: a review," *J. Mater. Res. Technol.*, vol. 15, pp. 855–884, 2021, doi: 10.1016/j.jmrt.2021.08.050.

[4] C. Meier, R. W. Penny, Y. Zou, J. S. Gibbs, and A. J. Hart, "Thermophysical Phenomena in Metal Additive Manufacturing By Selective Laser Melting: Fundamentals, Modeling, Simulation, and Experimentation," *Annu. Rev. Heat Transf.*, vol. 20, no. 1, pp. 241–316, 2018, doi: 10.1615/annualrevheattransfer.2018019042.

[5] M. Seifi, A. Salem, J. Beuth, O. Harrysson, and J. J. Lewandowski, "Overview of Materials Qualification Needs for Metal Additive Manufacturing," *Jom*, vol. 68, no. 3, pp. 747–764, 2016, doi: 10.1007/s11837-015-1810-0.

[6] C. W. Hull, "Apparatus for production of three-dimensional objects by stereolithography," US Patent 4,575,330, 1986.

[7] E. M. Igor Yadroitsev, Ina Yadroitsava, Anton Du Plessis, *Fundamentals of Laser Powder Bed Fusion of Metals*. .

[8] M. Technologies, "StandardTerminology for," pp. 5–7, 2016, doi:

10.1520/F2792-12A.2.

[9] E. Bogdan and P. Michorczyk, “3D Printing in Heterogeneous Catalysis—the State of the Art,” *Materials (Basel).*, vol. 13, no. 20, pp. 1–23, 2020, doi: 10.3390/ma13204534.

[10] I. Gibson, D. W. Rosen, and B. Stucker, *Chapter 6 Extrusion-Based Systems*. 2010.

[11] L. Yang *et al.*, *Electron Beam Technology*. 2017.

[12] M. Bhuvanesh Kumar and P. Sathiya, “Methods and materials for additive manufacturing: A critical review on advancements and challenges,” *Thin-Walled Struct.*, vol. 159, no. July, p. 107228, 2021, doi: 10.1016/j.tws.2020.107228.

[13] C. Y. Yap *et al.*, “Review of selective laser melting: Materials and applications,” *Appl. Phys. Rev.*, vol. 2, no. 4, 2015, doi: 10.1063/1.4935926.

[14] X. Shi *et al.*, “Performance of high layer thickness in selective laser melting of Ti6Al4V,” *Materials (Basel).*, vol. 9, no. 12, pp. 1–15, 2016, doi: 10.3390/ma9120975.

[15] C. Tan, K. Zhou, W. Ma, P. Zhang, M. Liu, and T. Kuang, “Microstructural evolution, nanoprecipitation behavior and mechanical properties of selective laser melted high-performance grade 300 maraging steel,” *Mater. Des.*, vol. 134, pp. 23–34, 2017, doi: 10.1016/j.matdes.2017.08.026.

[16] M. Seifi *et al.*, “Progress Towards Metal Additive Manufacturing Standardization to Support Qualification and Certification,” *Jom*, vol. 69, no. 3, pp. 439–455, 2017, doi: 10.1007/s11837-017-2265-2.

[17] J. J. Lewandowski and M. Seifi, “Metal Additive Manufacturing: A Review of Mechanical Properties,” *Annu. Rev. Mater. Res.*, vol. 46, no. April, pp. 151–186, 2016, doi: 10.1146/annurev-matsci-070115-032024.

[18] P. Auguste, A. Mauduit, L. Fouquet, and S. Pillot, “Study on 17-4 PH stainless steel produced by selective laser melting,” *UPB Sci. Bull. Ser. B Chem. Mater. Sci.*, vol. 80, no. 4, pp. 197–210, 2018.

[19] S. Vunnam, A. Saboo, C. Sudbrack, and T. L. Starr, “Effect of powder chemical composition on the as-built microstructure of 17-4 PH stainless steel processed by selective laser melting,” *Addit. Manuf.*, vol. 30, no. April, p. 100876, 2019, doi: 10.1016/j.addma.2019.100876.

[20] R. Division, B. Atomic, P. M. Division, B. Atomic, and N. Chemical, “Effects of Aging on the Microstructure of 17-4 PH Stainless Steel,” vol. 104, pp. 181–189, 1988.

[21] M. Murayama, Y. Katayama, and K. Hono, “Microstructural Evolution in a 17-4 PH Stainless Steel after Aging at 400 □C,” vol. 30, no. February, pp. 345–353, 1999.

[22] D. Deng, R. Chen, Q. Sun, and X. Li, “Microstructural Study of 17-4PH Stainless Steel after Plasma-Transferred Arc Welding,” pp. 424–434, 2015, doi: 10.3390/ma8020424.

[23] M. B. Balajaddeh and H. Na, “Pulsed Nd : YAG laser welding of 17-4 PH stainless steel : Microstructure , mechanical properties , and weldability investigation,” vol. 119, no. April, 2019, doi: 10.1016/j.optlastec.2019.105651.

[24] S. Steel, “Armco 17-4 ph ® ®.”

[25] L. Zai *et al.*, “Laser powder bed fusion of precipitation-hardened martensitic stainless steels: A review,” *Metals (Basel).*, vol. 10, no. 2, pp. 1–25, 2020, doi: 10.3390/met10020255.

[26] M. Alnajjar, F. Christien, K. Wolski, and C. Bosch, “Evidence of austenite by-passing in a stainless steel obtained from laser melting additive manufacturing,” *Addit. Manuf.*, vol. 25, pp. 187–195, 2019, doi:

10.1016/j.addma.2018.11.004.

[27] H. K. Rafi, D. Pal, N. Patil, T. L. Starr, and B. E. Stucker, “Microstructure and Mechanical Behavior of 17-4 Precipitation Hardenable Steel Processed by Selective Laser Melting,” *J. Mater. Eng. Perform.*, vol. 23, no. 12, pp. 4421–4428, 2014, doi: 10.1007/s11665-014-1226-y.

[28] M. Alnajjar, F. Christien, C. Bosch, and K. Wolski, “A comparative study of microstructure and hydrogen embrittlement of selective laser melted and wrought 17–4 PH stainless steel,” *Mater. Sci. Eng. A*, vol. 785, no. April, 2020, doi: 10.1016/j.msea.2020.139363.

[29] P. J. Withers and H. K. D. H. Bhadeshia, “Residual stress part 2 - Nature and origins,” *Mater. Sci. Technol.*, vol. 17, no. 4, pp. 366–375, 2001, doi: 10.1179/026708301101510087.

[30] J. L. Bartlett and X. Li, “An overview of residual stresses in metal powder bed fusion,” *Addit. Manuf.*, vol. 27, no. March, pp. 131–149, 2019, doi: 10.1016/j.addma.2019.02.020.

[31] P. J. Withers and H. K. D. H. Bhadeshia, “Residual stress part 1 - Measurement techniques,” *Mater. Sci. Technol.*, vol. 17, no. 4, pp. 355–365, 2001, doi: 10.1179/026708301101509980.

[32] P. Mercelis and J. Kruth, “Residual stresses in selective laser sintering and selective laser melting,” vol. 5, no. March, pp. 254–265, 2006, doi: 10.1108/13552540610707013.

[33] and J.-P. K. K. Kempen, L. Thijs, B. Vrancken, S. Buls, J. Van Humbeeck, “LOWERING THERMAL GRADIENTS IN SELECTIVE LASER MELTING BY PRE-HEATING THE BASEPLATE,” *Solid Free. Fabr. Symp. Proc.*, vol. 7, no. 1, pp. 37–72, 2015, [Online]. Available: https://www.researchgate.net/publication/269107473_What_is_governance/link/548173090cf22525dcb61443/download%0Ahttp://www.econ.upf.edu/~r

eynal/Civil wars_12December2010.pdf%0Ahttps://think-asia.org/handle/11540/8282%0Ahttps://www.jstor.org/stable/41857625.

[34] L. Parry, I. A. Ashcroft, and R. D. Wildman, “Understanding the effect of laser scan strategy on residual stress in selective laser melting through thermo-mechanical simulation,” *Addit. Manuf.*, vol. 12, pp. 1–15, 2016, doi: 10.1016/j.addma.2016.05.014.

[35] N. J. Harrison, I. Todd, and K. Mumtaz, “Reduction of micro-cracking in nickel superalloys processed by Selective Laser Melting: A fundamental alloy design approach,” *Acta Mater.*, vol. 94, pp. 59–68, 2015, doi: 10.1016/j.actamat.2015.04.035.

[36] S. Catchpole-Smith, N. Aboulkhair, L. Parry, C. Tuck, I. A. Ashcroft, and A. Clare, “Fractal scan strategies for selective laser melting of ‘unweldable’ nickel superalloys,” *Addit. Manuf.*, vol. 15, pp. 113–122, 2017, doi: 10.1016/j.addma.2017.02.002.

[37] P. Michaleris, *Minimization of welding distortion and buckling: Modelling and implementation*. 2011.

[38] X. Lu, M. Cervera, M. Chiumenti, and X. Lin, “Residual stresses control in additive manufacturing,” *J. Manuf. Mater. Process.*, vol. 5, no. 4, 2021, doi: 10.3390/jmmp5040138.

[39] H. J. Stone *et al.*, “in Ferritic Steels,” pp. 1–8, 2007.

[40] J. A. Francis, H. K. D. H. Bhadeshia, and P. J. Withers, “Welding residual stresses in ferritic power plant steels,” *Mater. Sci. Technol.*, vol. 23, no. 9, pp. 1009–1020, 2007, doi: 10.1179/174328407X213116.

[41] H. K. D. H. Bhadeshia and R. W. K. Honeycombe, *Steels and Properties*. 2017.

[42] D. P. Koistinen and R. E. Marburger, “A general equation prescribing the

extent of the austenite-martensite transformation in pure iron-carbon alloys and plain carbon steels," *Acta Metall.*, vol. 7, no. 1, pp. 59–60, 1959, doi: 10.1016/0001-6160(59)90170-1.

[43] D. W. Suh, C. S. Oh, H. N. Han, and S. J. Kim, "Dilatometric analysis of austenite decomposition considering the effect of non-isotropic volume change," *Acta Mater.*, vol. 55, no. 8, pp. 2659–2669, 2007, doi: 10.1016/j.actamat.2006.12.007.

[44] H. Jia, H. Sun, H. Wang, Y. Wu, and H. Wang, "Scanning strategy in selective laser melting (SLM): a review," *Int. J. Adv. Manuf. Technol.*, vol. 113, no. 9–10, pp. 2413–2435, 2021, doi: 10.1007/s00170-021-06810-3.

[45] S. Zou *et al.*, "Numerical analysis of the effect of the scan strategy on the residual stress in the multi-laser selective laser melting," *Results Phys.*, vol. 16, no. January, p. 103005, 2020, doi: 10.1016/j.rinp.2020.103005.

[46] C. Chen, J. Yin, H. Zhu, Z. Xiao, L. Zhang, and X. Zeng, "Effect of overlap rate and pattern on residual stress in selective laser melting," *Int. J. Mach. Tools Manuf.*, vol. 145, no. December 2018, p. 103433, 2019, doi: 10.1016/j.ijmachtools.2019.103433.

[47] D. Wang *et al.*, "The effect of a scanning strategy on the residual stress of 316L steel parts fabricated by selective laser melting (SLM)," *Materials (Basel).*, vol. 11, no. 10, 2018, doi: 10.3390/ma11101821.

[48] L. Zhang, S. Zhang, and H. Zhu, "Effect of scanning strategy on geometric accuracy of the circle structure fabricated by selective laser melting," *J. Manuf. Process.*, vol. 64, no. February, pp. 907–915, 2021, doi: 10.1016/j.jmapro.2021.02.015.

[49] X. K. Zhu and Y. J. Chao, "Effects of temperature-dependent material properties on welding simulation," *Comput. Struct.*, vol. 80, no. 11, pp. 967–976, 2002, doi: 10.1016/S0045-7949(02)00040-8.

[50] B. Vrancken, R. Wauthle, J. P. Kruth, and J. Van Humbeeck, “Study of the influence of material properties on residual stress in selective laser melting,” *24th Int. SFF Symp. - An Addit. Manuf. Conf. SFF 2013*, pp. 393–407, 2013.

[51] M. Yakout, M. A. Elbestawi, S. C. Veldhuis, and S. Nangle-Smith, “Influence of thermal properties on residual stresses in SLM of aerospace alloys,” *Rapid Prototyp. J.*, vol. 26, no. 1, pp. 213–222, 2020, doi: 10.1108/RPJ-03-2019-0065.

[52] M. Howes, T. Inoue, and M. Park, *Handbook of Residual Stress and Deformation of Steel Edited by*. 2002.

[53] *STRESS MEASUREMENT METHODS PRACTICAL RESIDUAL STRESS MEASUREMENT*. .

[54] B. Vrancken, “Study of Residual Stresses in Selective Laser Melting,” *PhD Thesis; KU Leuven Arenb. Dr. Sch. Fac. Eng. Sci.*, no. June, pp. 1–253, 2016, [Online]. Available: https://lirias.kuleuven.be/bitstream/123456789/542751/1/thesis+Bey+Vrancken+v01-06-2016+FINAL_compressed.pdf.

[55] M. B. Prime, “Cross-sectional mapping of residual stresses by measuring the surface contour after a cut,” *J. Eng. Mater. Technol. Trans. ASME*, vol. 123, no. 2, pp. 162–168, 2001, doi: 10.1115/1.1345526.

[56] H. Bisaria and P. Shandilya, “Machining of Metal Matrix Composites by EDM and its Variants: A Review,” no. January 2015, pp. 267–282, 2015, doi: 10.2507/daaam.scibook.2015.23.

[57] L. Bass, J. Milner, T. Gnäupel-Herold, and S. Moylan, “Residual Stress in Additive Manufactured Nickel Alloy 625 Parts,” *J. Manuf. Sci. Eng. Trans. ASME*, vol. 140, no. 6, pp. 39–45, 2018, doi: 10.1115/1.4039063.

[58] B. Schoinochoritis, D. Chantzis, and K. Salonitis, “Simulation of metallic powder bed additive manufacturing processes with the finite element

method: A critical review," *Proc. Inst. Mech. Eng. Part B J. Eng. Manuf.*, vol. 231, no. 1, pp. 96–117, 2017, doi: 10.1177/0954405414567522.

[59] B. Cheng, S. Shrestha, and K. Chou, "Stress and deformation evaluations of scanning strategy effect in selective laser melting," *Addit. Manuf.*, vol. 12, pp. 240–251, 2016, doi: 10.1016/j.addma.2016.05.007.

[60] J. C. Traer, "HIGH FIDELITY ADDITIVE MANUFACTURING PROCESS MODELING By In conformity with the requirements for," no. August, 2018.

[61] J. G. Michopoulos, A. P. Iliopoulos, J. C. Steuben, A. J. Birnbaum, and S. G. Lambrakos, "On the multiphysics modeling challenges for metal additive manufacturing processes," *Addit. Manuf.*, vol. 22, pp. 784–799, 2018, doi: 10.1016/j.addma.2018.06.019.

[62] N. Shen and K. Chou, "SIMULATIONS OF THERMO-MECHANICAL CHARACTERISTICS IN ELECTRON BEAM ADDITIVE MANUFACTURING," *Proc. ASME 2012 Int. Mech. Eng. Congr. Expo. IMECE2012 Novemb. 9-15, 2012, Houston, Texas, USA*, pp. 1–8, 2016.

[63] M. Labudovic, D. Hu, and R. Kovacevic, "A three dimensional model for direct laser metal powder deposition and rapid prototyping," *J. Mater. Sci.*, vol. 38, no. 1, pp. 35–49, 2003, doi: 10.1023/A:1021153513925.

[64] N. Ma *et al.*, "Inherent Strain Method for Residual Stress Measurement and Welding Distortion Prediction," no. January 2017, 2016, doi: 10.1115/omae2016-54184.

[65] Q. Chen *et al.*, "An inherent strain based multiscale modeling framework for simulating part-scale residual deformation for direct metal laser sintering," *Addit. Manuf.*, vol. 28, no. May, pp. 406–418, 2019, doi: 10.1016/j.addma.2019.05.021.

[66] "Advanced inherent strain for distortion prediction in additive

manufacturing," no. 1995, p. 2017, 2017.

[67] X. Liang, Q. Chen, L. Cheng, Q. Yang, and A. To, "A Modified Inherent Strain Method for Fast Prediction of Residual Deformation in Additive Manufacturing of Metal Parts," *Solid Free. Fabr. Symp.*, pp. 2539–2545, 2017, [Online]. Available: https://sffsymposium.engr.utexas.edu/sites/default/files/2017/Manuscripts/AModifiedInherentStrainMethodforFastPredict.pdf.

[68] X. Liang, Q. Chen, L. Cheng, D. Hayduke, and A. C. To, "Modified inherent strain method for efficient prediction of residual deformation in direct metal laser sintered components," *Comput. Mech.*, no. 0123456789, 2019, doi: 10.1007/s00466-019-01748-6.

[69] F. Hajializadeh and A. Ince, "Short review on modeling approaches for metal additive manufacturing process," *Mater. Des. Process. Commun.*, vol. 2, no. 2, pp. 1–7, 2020, doi: 10.1002/mdp2.56.

[70] M. Bugatti and Q. Semeraro, "Limitations of the inherent strain method in simulating powder bed fusion processes," *Addit. Manuf.*, vol. 23, no. June 2017, pp. 329–346, 2018, doi: 10.1016/j.addma.2018.05.041.

[71] H. Murakawa, "Computational welding mechanics and concept of inherent strain for industrial applications," *Mater. Sci. Forum*, vol. 539–543, no. PART 1, pp. 181–186, 2007, doi: 10.4028/www.scientific.net/msf.539-543.181.

[72] C. Li, C. H. Fu, Y. B. Guo, and F. Z. Fang, "Fast Prediction and Validation of Part Distortion in Selective Laser Melting," *Procedia Manuf.*, vol. 1, pp. 355–365, 2015, doi: 10.1016/j.promfg.2015.09.042.

[73] N. Peter, Z. Pitts, S. Thompson, and A. Saharan, "Benchmarking build simulation software for laser powder bed fusion of metals," *Addit. Manuf.*, vol. 36, no. October 2019, p. 101531, 2020, doi:

10.1016/j.addma.2020.101531.

[74] T. Mayer, G. Brändle, A. Schönenberger, and R. Eberlein, “Simulation and validation of residual deformations in additive manufacturing of metal parts,” *Heliyon*, vol. 6, no. 5, 2020, doi: 10.1016/j.heliyon.2020.e03987.

[75] X. Liang, L. Cheng, Q. Chen, Q. Yang, and A. C. To, “A modified method for estimating inherent strains from detailed process simulation for fast residual distortion prediction of single-walled structures fabricated by directed energy deposition,” *Addit. Manuf.*, vol. 23, no. August, pp. 471–486, 2018, doi: 10.1016/j.addma.2018.08.029.

[76] M. Siewert, F. Neugebauer, J. Epp, and V. Ploshikhin, “Validation of Mechanical Layer Equivalent Method for simulation of residual stresses in additive manufactured components,” *Comput. Math. with Appl.*, vol. 78, no. 7, pp. 2407–2416, 2019, doi: 10.1016/j.camwa.2018.08.016.

[77] P. Michaleris, “Modeling metal deposition in heat transfer analyses of additive manufacturing processes,” *Finite Elem. Anal. Des.*, vol. 86, pp. 51–60, 2014, doi: 10.1016/j.finel.2014.04.003.

[78] N. Saunders and A. P. Miodownik, *CALPHAD: Calculation of Phase Diagrams. A Comprehensive Guide*, vol. 1. 1998.

[79] Z. Guo, N. Saunders, and J. P. Schille, “Modelling phase transformations and material properties critical to simulation of heat treatment distortion in steels,” *Proc. 17th IFHTSE Congr.*, vol. 2, no. 2, pp. 753–756, 2008.

[80] F. Christien, M. T. F. Telling, and K. S. Knight, “A comparison of dilatometry and in-situ neutron diffraction in tracking bulk phase transformations in a martensitic stainless steel,” *Mater. Charact.*, vol. 82, pp. 50–57, 2013, doi: 10.1016/j.matchar.2013.05.002.

[81] M. Ghayoor, K. Lee, Y. He, C. hung Chang, B. K. Paul, and S. Pasebani, “Selective laser melting of 304L stainless steel: Role of volumetric energy

density on the microstructure, texture and mechanical properties," *Addit. Manuf.*, vol. 32, p. 101011, 2020, doi: 10.1016/j.addma.2019.101011.

[82] L. Tonelli, A. Fortunato, and L. Ceschini, "CoCr alloy processed by Selective Laser Melting (SLM): effect of Laser Energy Density on microstructure, surface morphology, and hardness," *J. Manuf. Process.*, vol. 52, no. March 2019, pp. 106–119, 2020, doi: 10.1016/j.jmapro.2020.01.052.

[83] J. A. Cherry, H. M. Davies, S. Mehmood, N. P. Lavery, S. G. R. Brown, and J. Sienz, "Investigation into the effect of process parameters on microstructural and physical properties of 316L stainless steel parts by selective laser melting," *Int. J. Adv. Manuf. Technol.*, vol. 76, no. 5–8, pp. 869–879, 2015, doi: 10.1007/s00170-014-6297-2.

[84] A. Ozsoy, E. Yasa, M. Keles, and E. B. Tureyen, "Pulsed-mode Selective Laser Melting of 17-4 PH stainless steel: Effect of laser parameters on density and mechanical properties," *J. Manuf. Process.*, vol. 68, no. PA, pp. 910–922, 2021, doi: 10.1016/j.jmapro.2021.06.017.

[85] T. Varona, "Sensitivity analysis and experimental calibration for the Additive Manufacturing computational framework," 2016.

[86] W. Liu, H. Wei, C. Huang, F. Yuan, and Y. Zhang, "Energy efficiency evaluation of metal laser direct deposition based on process characteristics and empirical modeling," *Int. J. Adv. Manuf. Technol.*, vol. 102, no. 1–4, pp. 901–913, 2019, doi: 10.1007/s00170-018-03220-w.

APPENDICES

A. DILATOMETRY

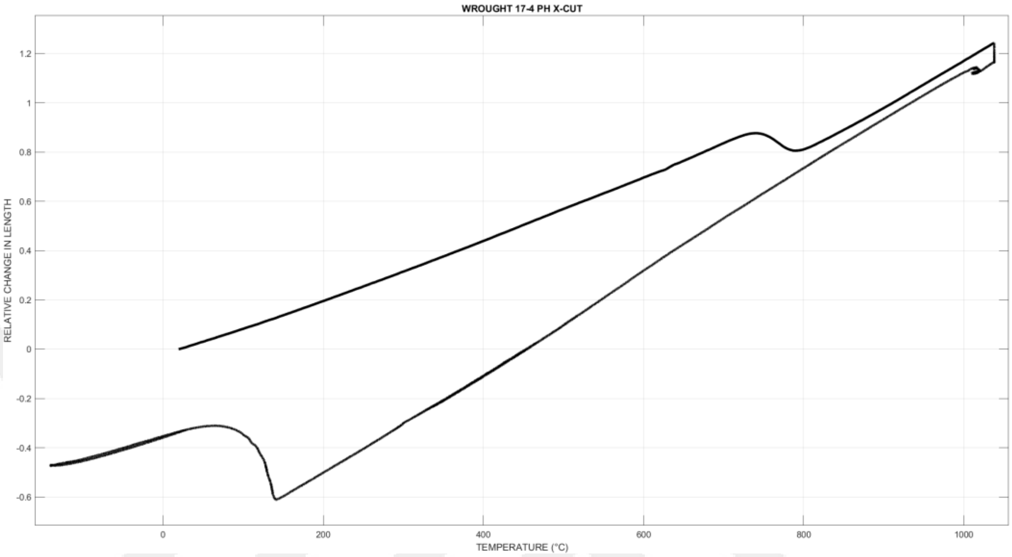

Figure 102: Wrought 17-4 PH X-Cut

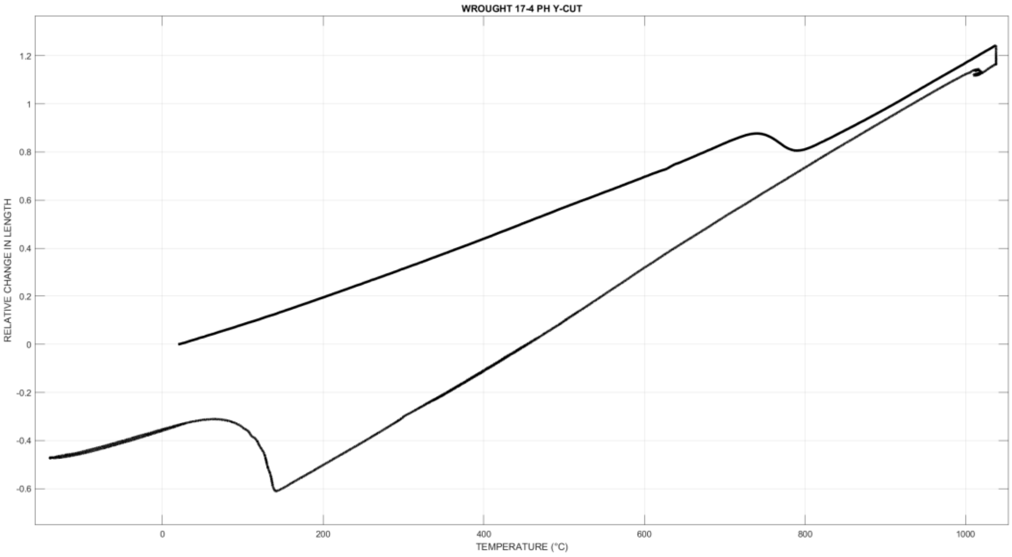

Figure 103: Wrought 17-4 PH Y-Cut

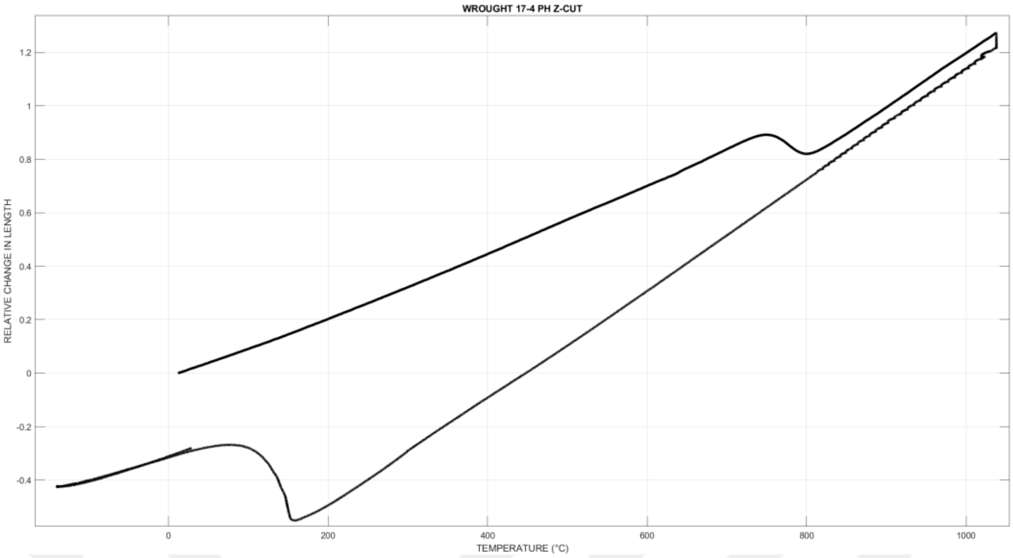

Figure 104: Wrought 17-4 PH Z-Cut

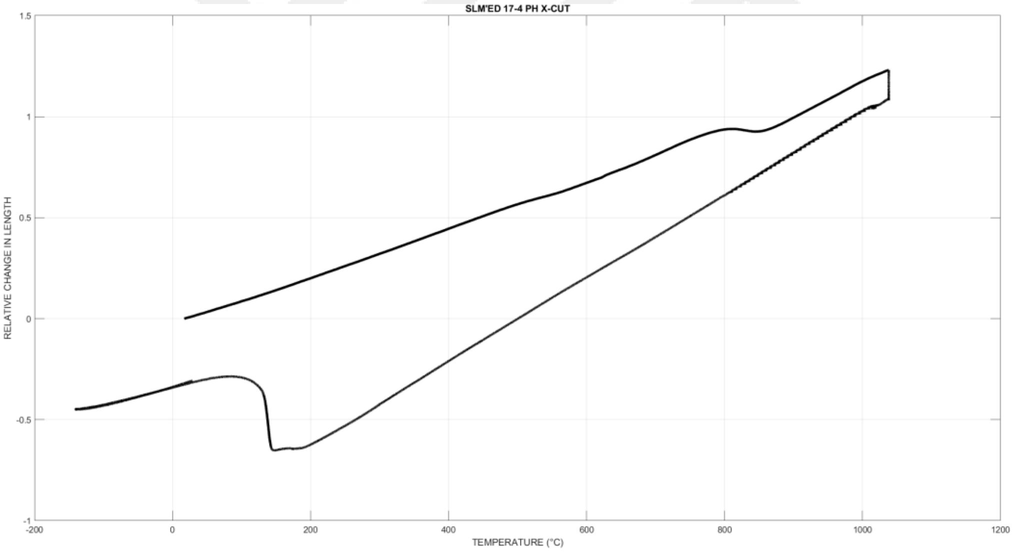

Figure 105: SLM'ed 17-4 PH X-Cut

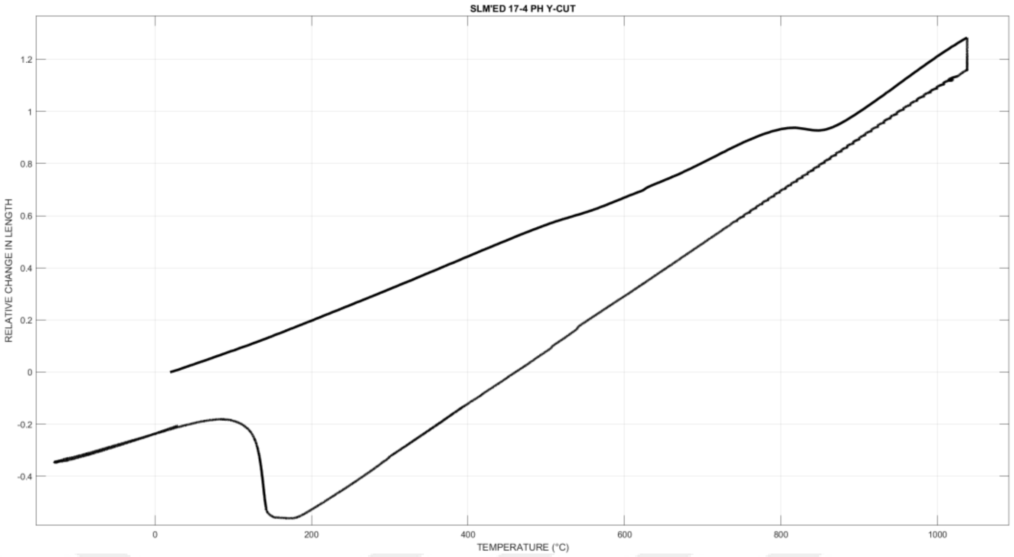

Figure 106: SLM'ed 17-4 PH Y-Cut

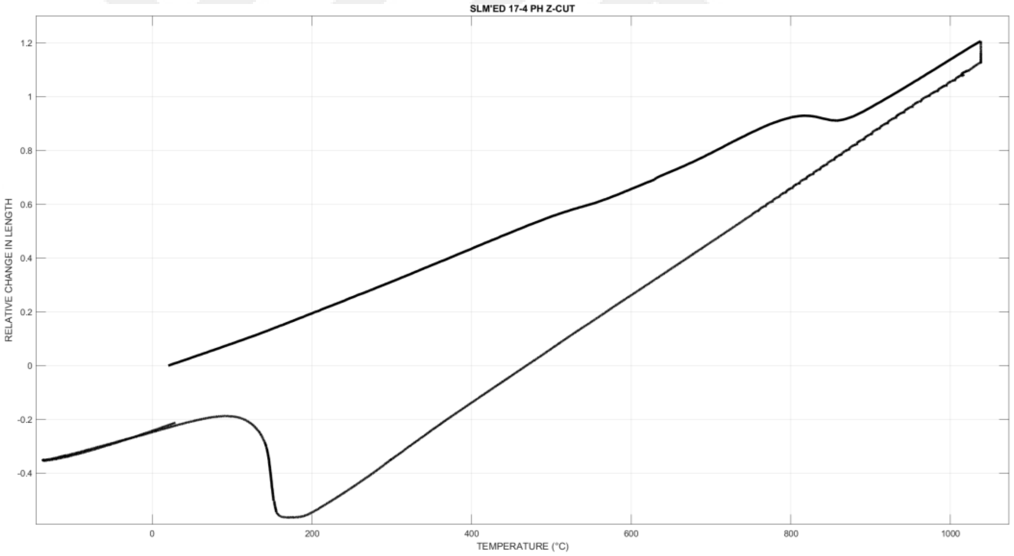

Figure 107: SLM'ed 17-4 PH Z-Cut

B. MATERIAL DATA

Table 8: Hybrid Material Data

T (°C)	**ρ (g/cm³)**	**E (Mpa)**	**v**	**k (W/mK)**	**cp (J/kgK)**	**α (m/mK)**
20	7.84	212	0.29	19.19	496	1.13E-05
50	7.81	210	0.29	19.48	506	1.14E-05
100	7.77	208	0.30	19.95	521	1.14E-05
150	7.74	205	0.30	20.44	534	1.15E-05
200	7.70	202	0.30	20.94	546	1.16E-05
250	7.67	198	0.30	21.45	558	1.17E-05
300	7.64	194	0.30	21.98	568	1.18E-05
350	7.61	190	0.31	22.52	578	1.18E-05
400	7.58	185	0.31	23.07	587	1.19E-05
450	7.55	179	0.31	23.63	596	1.20E-05

Table 8: Hybrid Material Data (continued)

500	7.53	174	0.31	24.21	604	1.21E-05
550	7.51	168	0.31	24.81	611	1.22E-05
600	7.48	162	0.32	25.41	619	1.22E-05
650	7.46	155	0.32	26.04	626	1.23E-05
700	7.44	149	0.32	26.67	633	1.24E-05
750	7.42	142	0.32	27.33	639	1.25E-05
800	7.41	135	0.32	28.00	645	1.25E-05
850	7.39	128	0.33	28.68	651	1.26E-05
900	7.37	121	0.33	29.38	657	1.27E-05
950	7.36	114	0.33	30.10	663	1.28E-05
1000	7.34	107	0.33	30.84	668	1.29E-05
1050	7.33	101	0.34	31.60	673	1.29E-05
1100	7.31	97	0.34	32.37	678	1.30E-05

Table 8: Hybrid Material Data (continued)

1150	7.30	91	0.34	33.16	683	1.31E-05
1200	7.29	84	0.34	33.98	688	1.32E-05
1250	7.27	78	0.34	34.81	693	1.33E-05
1300	7.26	71	0.35	35.66	697	1.33E-05
1350	7.25	65	0.35	36.53	702	1.34E-05
1400	7.18	17	0.41	34.92	773	2.38E-05
1450	7.09	0	0.48	35.69	787	3.46E-05
1500	7.03	0	0.50	36.46	801	3.72E-05
1550	6.99	0	0.50	37.22	814	3.77E-05
1600	6.96	0	0.50	37.99	828	3.82E-05
1650	6.92	0	0.50	38.76	842	3.88E-05
1700	6.88	0	0.50	39.53	856	3.93E-05
1750	6.84	0	0.50	40.30	870	3.98E-05

Table 8: Hybrid Material Data (continued)

1800	6.80	0	0.50	41.07	884	4.03E-05
1850	6.76	0	0.50	41.83	898	4.08E-05
1900	6.72	0	0.50	42.60	912	4.13E-05
1950	6.68	0	0.50	43.37	925	4.18E-05
2000	6.64	0	0.50	44.14	939	4.24E-05
2050	6.61	0	0.50	44.91	953	4.29E-05
2100	6.57	0	0.50	45.68	967	4.34E-05
2150	6.53	0	0.50	46.45	981	4.39E-05

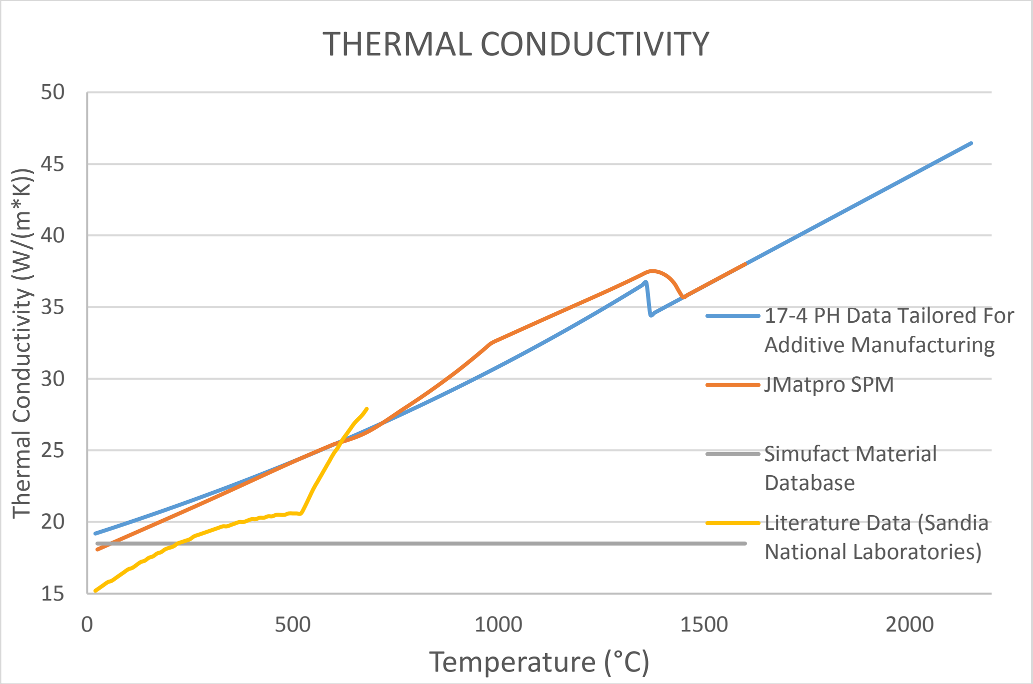

Figure 108: Temperature dependent thermal conductivity data of 17-4 PH SS

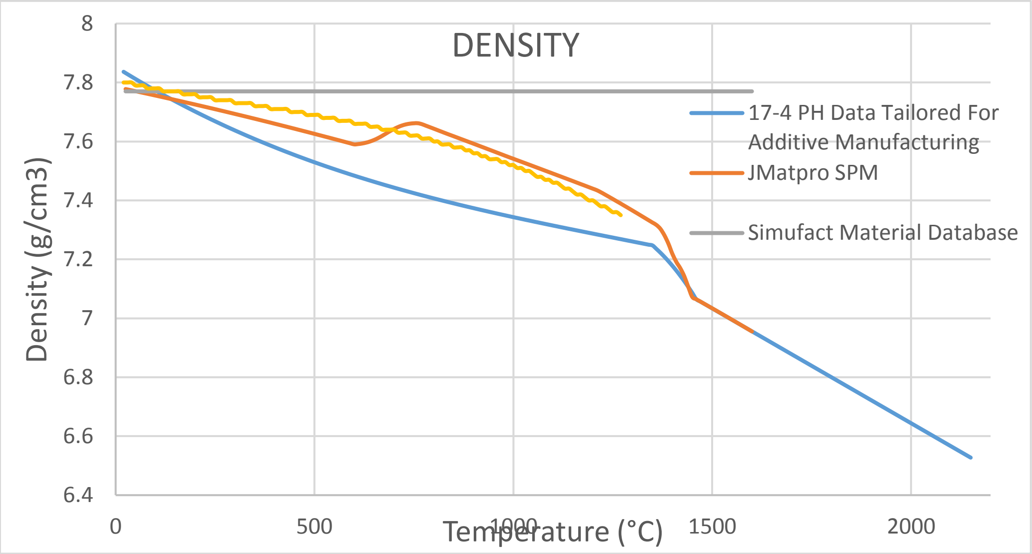

Figure 109: Temperature dependent density data of 17-4 PH SS

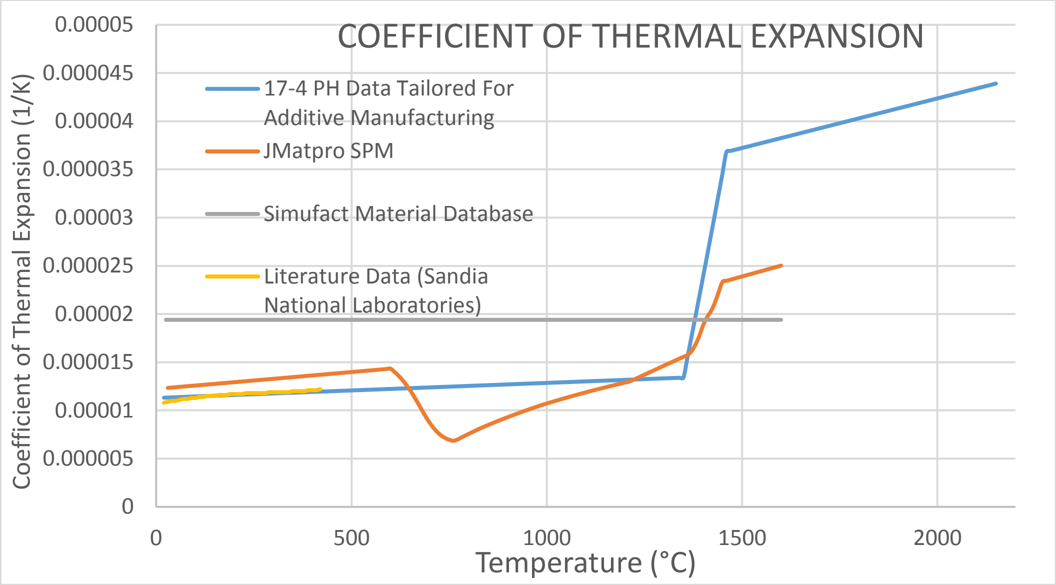

Figure 110: Temperature dependent thermal expansion coefficient data of 17-4 PH SS

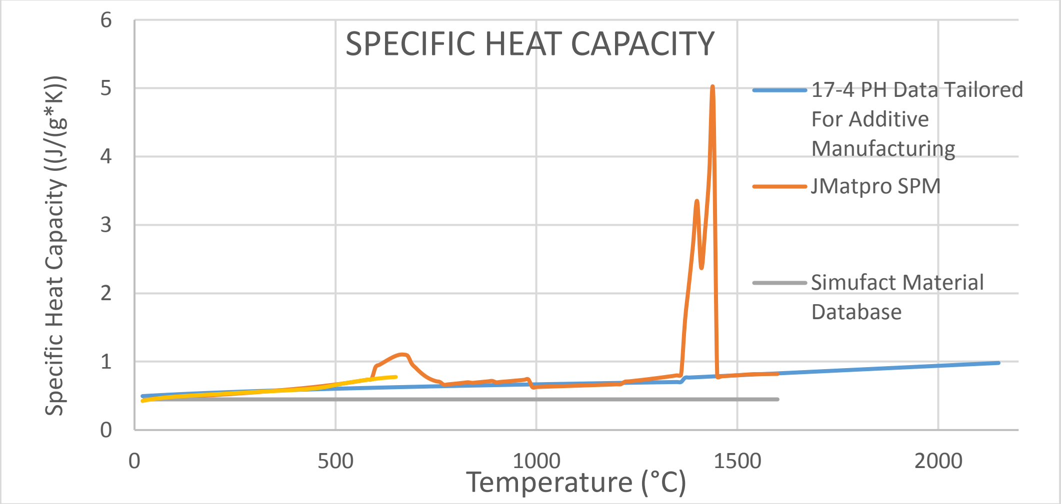

Figure 111: Temperature dependent specific heat capacity data of 17-4 PH SS

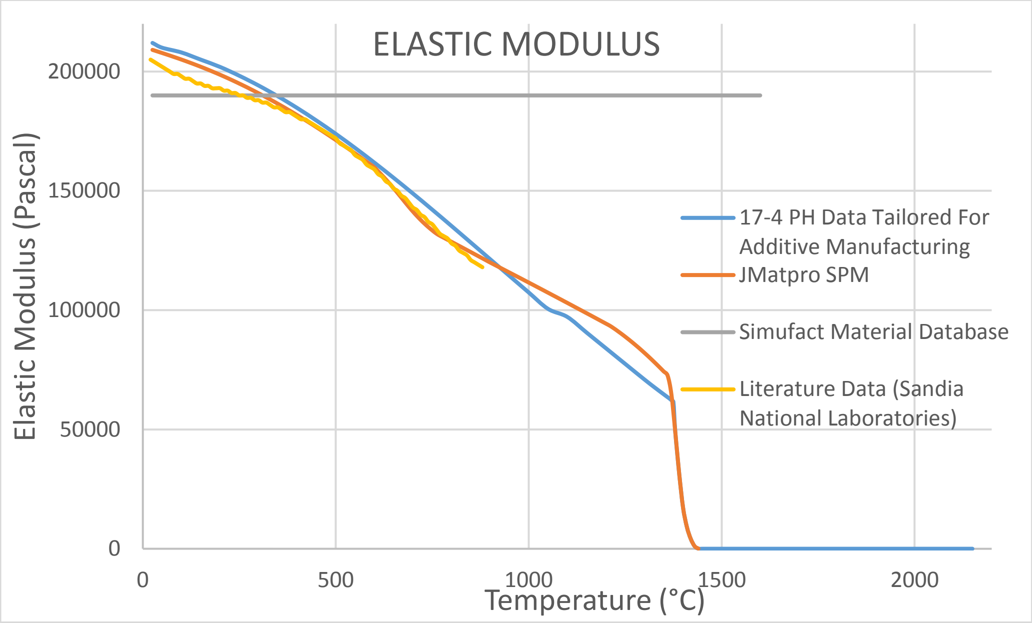

Figure 112: Temperature dependent Elastic Modulus data of 17-4 PH SS

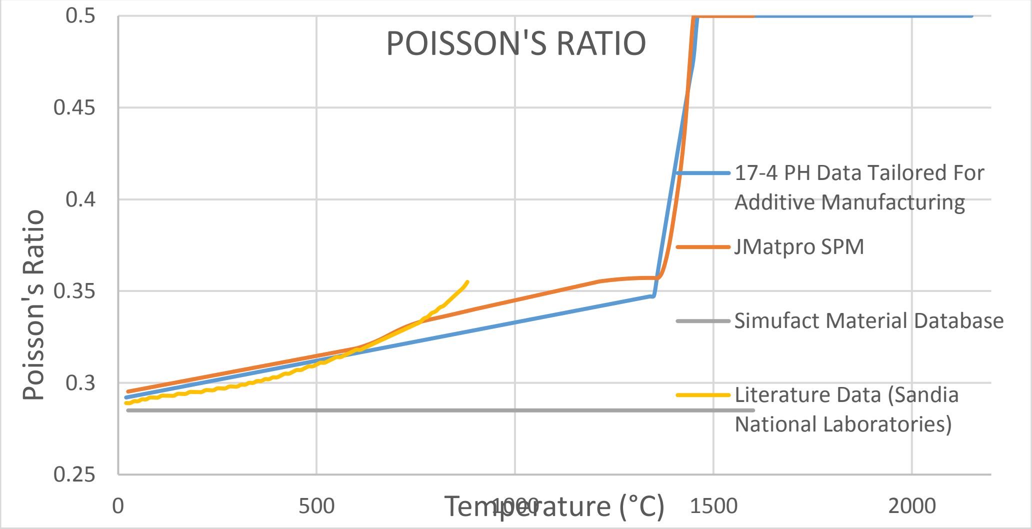

Figure 113: Temperature dependent Poisson’s ratio data of 17-4 PH SS

Creep Data

Creep behaviour of metals have three stages as primary, secondary (steady state) and tertiary stage.

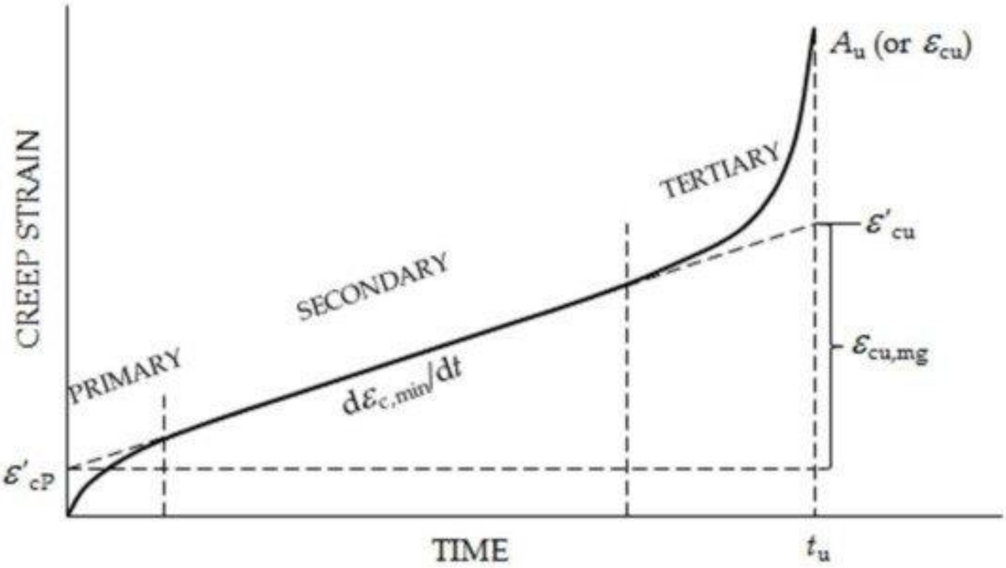

Figure 114: Stages of Creep

Time until failure passes mostly in secondary stage which is defined by following model:

$$\varepsilon = A\sigma^{n}\exp\left(-Q/RT\right)$$

Where A: Constant related to material microstructure

Q: Activation energy

R: Gas constant

σ: Applied stress

n: Stress exponent

Which are to be determined for the simulation of heat treatment. By using JMatPro, 2 different curves at 450°C and 500 °C are calculated for 17-4 PH SS as given below;

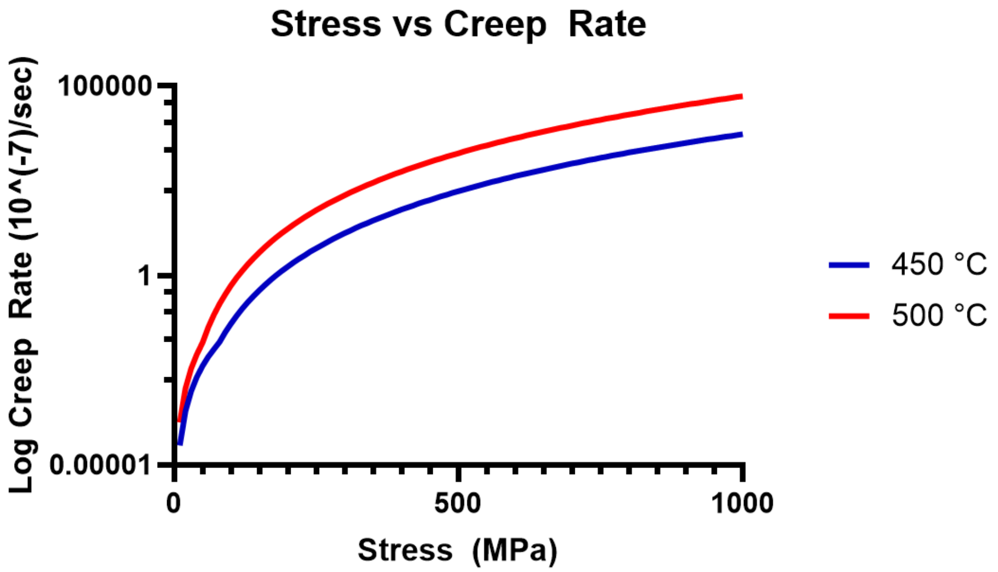

Figure 115: Creep data obtained from JmatPro at 2 different temperatures

$$ln\varepsilon = lnA + nln\sigma - Q/RT$$

For σ= 500 Mpa, T1=450 °C, T2= 500 °C

n=4.96

For T= 450 °C, σ1= 500 MPa, σ2= 750 MPa

A=1.88E-31

Q=261561.58

Determination of Koistinen Marburger Parameter

Lower portion of dilatometry curve at the onset of martensitic phase transformation is given below;

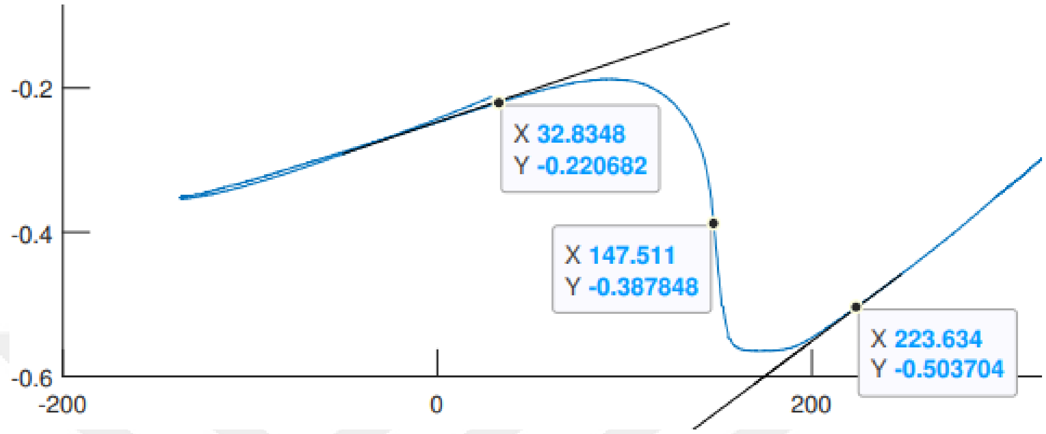

Figure 116: Dilatometry curve between martensite start to martensite finish temperatures

Fraction of Martensite transformed at any specific temperature is determined by lever rule;

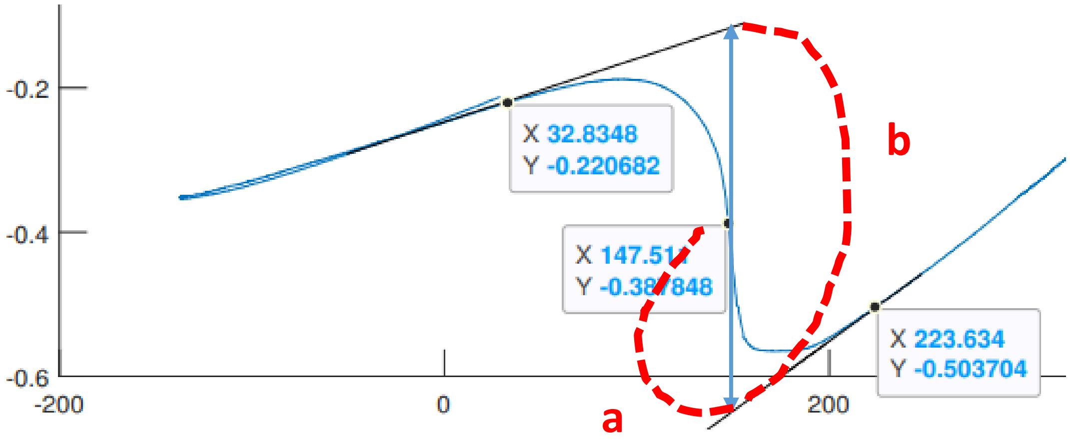

Figure 117: Lever Rule between MS-MF

Repeating the lever rule between the MS to MF transformation range yields;

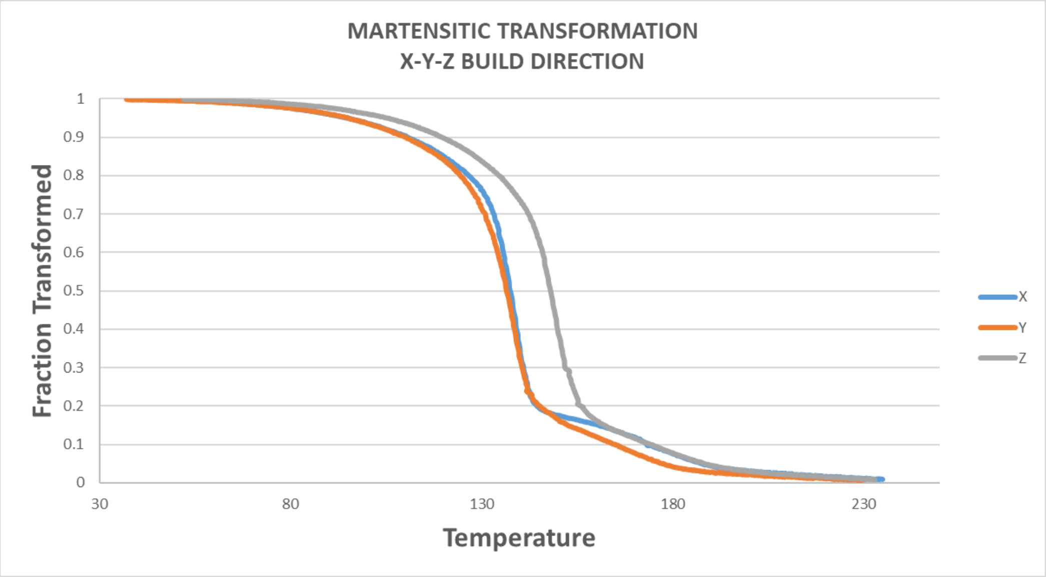

Figure 118: Fraction of martensite transformed between MS-MF

Temperature dependent (time independent) martensitic transformation is defined by Koistinen Marburger equation given by;

$$Xm = Xa0\ (1 - e^{-k(MS-T)})$$

$$k = -\ln\ (0.01)/(Ms - Mf)$$

Where;

Xa0 is Austenite fraction at the beginning of transformation,

XM is fraction of Martensite at any temperature,

k is Koistinen-Marburger parameter

T is Temperature,

Ms is Martensite start temperature

C. PHASE TRANSFORMATION STRAIN

Phase transformation strains are calculated by extrapolating linear regions of lower portion of dilatometry curve.

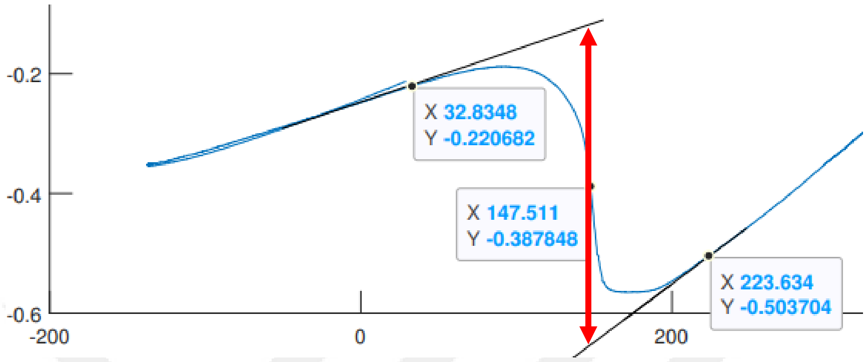

Figure 119: Calculation of phase transformation strain

Strain difference between the linear extrapolated lines yields γ>martensite transformation strains. Calculated transformation strains in X, Y, Z directions of SLM’ed 17-4 PH SS are given below;

Table 9: Phase transformation strain values of SLM'ed 17-4 PH SS in X-Y-Z directions

Transformation Strain	**Value**
ε_{trX}	5.47 E-3
ε_{trY}	5.57 E-3
ε_{trZ}	5.52 E-3
Volume Change	%1.63